

DEVELOPMENT OF 100W PORTABLE FUEL CELL SYSTEM  
WORKING WITH SODIUM BOROHYDRIDE

A THESIS SUBMITTED TO  
THE GRADUATE SCHOOL OF NATURAL AND APPLIED SCIENCES  
OF  
MIDDLE EAST TECHNICAL UNIVERSITY

BY

SERDAR ERKAN

IN PARTIAL FULFILLMENT OF THE REQUIREMENTS  
FOR  
THE DEGREE OF DOCTOR OF PHILOSOPHY  
IN  
CHEMICAL ENGINEERING

SEPTEMBER 2011

Approval of the thesis:

**DEVELOPMENT OF 100W PORTABLE FUEL CELL SYSTEM  
WORKING WITH SODIUM BOROHYDRIDE**

Submitted by **SERDAR ERKAN** in partial fulfillment of the requirements for the degree of **Doctor of Philosophy in Chemical Engineering Department, Middle East Technical University** by,

Prof.Dr. Canan Özgen  
Dean, Graduate School of **Natural and Applied Sciences**

\_\_\_\_\_

Prof. Dr. Deniz Üner  
Head of Department, **Chemical Engineering**

\_\_\_\_\_

Prof. Dr. İnci Eroğlu  
Supervisor, **Chemical Engineering Dept., METU**

\_\_\_\_\_

**Examining Committee Members:**

Prof. Dr. Nurcan Baç  
Chemical Engineering Dept., Yeditepe Univ.

\_\_\_\_\_

Prof. Dr. İnci Eroğlu  
Chemical Engineering Dept., METU

\_\_\_\_\_

Prof. Dr. Işık Önal  
Chemical Engineering Dept., METU

\_\_\_\_\_

Prof. Dr. Zeynep İlsen Önsan  
Chemical Engineering Dept., Boğaziçi Univ.

\_\_\_\_\_

Assist. Prof. Dr. Serkan Kıncal  
Chemical Engineering Dept., METU

\_\_\_\_\_

Date: 12.09.2011

**I hereby declare that all information in this document has been obtained and presented in accordance with academic rules and ethical conduct. I also declare that, as required by these rules and conduct, I have fully cited and referenced all material and results that are not original to this work.**

Name, Last name : Serdar ERKAN

Signature :

## **ABSTRACT**

### **DEVELOPMENT OF 100W PORTABLE FUEL CELL SYSTEM WORKING WITH SODIUM BOROHYDRIDE**

Erkan, Serdar

Ph.D., Department of Chemical Engineering

Supervisor: Prof. Dr. İnci Eroğlu

September 2011, 179 pages

Fuel cells are electricity generators which convert chemical energy of hydrogen directly to electricity by means of electrochemical oxidation and reduction reactions. A single proton exchange membrane (PEM) fuel cell can only generate electricity with a potential between 0.5V and 1V. The useful potential can be achieved by stacking cells in series to form a PEM fuel cell stack. There is a potential to utilize 100W class fuel cells. Fuelling is the major problem of the portable fuel cells.

The aim of this thesis is to design and manufacture a PEM fuel cell stack which can be used for portable applications. The PEM fuel cell stack is planned to be incorporated to a NaBH<sub>4</sub> hydrolysis reactor for H<sub>2</sub> supply. Within the scope of this thesis a new coating technique called “ultrasonic spray coating technique” is developed for membrane electrode assembly (MEA) manufacturing. New metal and graphite bipolar plates are designed and manufactured by CNC technique. A fuel cell controller hardware is developed for fuel supply and system control.

The power densities reached with the new method are 0.53, 0.74, 0.77, and 0.88 W/cm<sup>2</sup> for 20%, 40%, 50%, 70% Pt/C catalyst by keeping 0.4mg Pt/cm<sup>2</sup> platinum loading constant, respectively. The power density increase is 267% compared to “spraying of catalyst ink with air pressure atomizing spray gun”.

All parts of the PEM fuel cell stack designed were produced, assembled, and tested. The current density reached is 12.9A at 12 V stack potential and the corresponding electrical power of the stack is 155W.

Keywords: PEM fuel cell stack, portable PEM fuel cell system, sodium borohydride, membrane electrode assembly, fuel cell controller.

## ÖZ

### SODYUM BOR HİDRÜR İLE ÇALIŞAN 100 W PORTATİF YAKIT PİLİ SİSTEMİ GELİŞTİRİLMESİ

Erkan, Serdar

Doktora, Kimya Mühendisliği Bölümü

Tez Yöneticisi: Prof. Dr. İnci Eroğlu

Eylül 2011, 179 sayfa

Yakıt pilleri hidrojenin kimyasal enerjisini elektrokimyasal oksidasyon ve indirgenme reaksiyonları ile doğrudan elektriğe çeviren jeneratörlerdir. Tekli bir yakıt hücresi potansiyeli 0.5 V ile 1 V arasında bir elektrik üretebilir. Kullanılabilir potansiyel, yakıt pili yığınının oluşturmak için hücrelerin seri bağlanması ile sağlanır. 100 W sınıfı yakıt pillerinin kullanılabilmesi için potansiyel bulunmaktadır. Yakıt sağlama portatif yakıt pillerinin temel sorunudur.

Bu tezin amacı, portatif uygulamalarda kullanılacak bir polimer elektrolit membranlı (PEM) yakıt pili yığınının tasarlanması ve üretilmesidir. PEM yakıt pilinin hidrojen sağlayıcısı olarak  $\text{NaBH}_4$  hidroliz reaktörü ile birleştirilmesi planlanmıştır. Bu tezin kapsamında membran elektrot atacı (MEA) imalatı için “ultrasonik spre y kaplama tekniği” adında yeni bir kaplama tekniği geliştirilmiştir. Yeni metal ve grafit plakalar tasarlanmış ve CNC tekniği ile imal edilmiştir. Yakıt besleme ve sistem kontrolü için yakıt pili kontrol cihazı geliştirilmiştir.

Yeni metot ile ulařılan g yoęunlukları 0.4mg Pt/cm<sup>2</sup> platin yklemesini sabit tutarak %20, %40, %50 ve %70 Pt/C katalizler iin sırasıyla, 0.53, 0.74, 0.77 ve 0.88 W/cm<sup>2</sup> ye ulařmıřtır. G yoęunluęu artıřı, katalizr mrekkebinin “basınlı hava sprey tabancası pskrtme yntemi” ile pskrtlmesine kıyasla %267 artmıřtır.

PEM yakıt piline ait btn paralar tasarlanmıř, imal edilmiř ve test edilmiřtir. Ulařılan akım yoęunluęu 12 V potansiyelde 12.9A’e ulařmıřtır ve buna karřılık gelen yıęın gc 155W tır.

Anahtar Kelimeler: PEM yakıt pili yıęını, portatif PEM yakıt pili sistemi, sodyum bor hidrr, membran elektrot atacı, yakıt pili kontrol cihazı

To My Family and My Love

## ACKNOWLEDGMENTS

I would like to express my deepest gratitude to my thesis supervisor, Prof. Dr. İnci Erođlu for her invaluable guidance, encouragement, humanity and insight throughout the research.

The members of the PhD examining committee, Prof. Dr. Zeynep İlsen Önsan and Prof. Dr. Nurcan Baç are gratefully acknowledged for their critical and constructive comments that help the progress of the thesis.

I would like to thank my great friends and partners Dr. Yılser Devrim and Hüseyin Devrim for their help, and support they gave me.

I am also thankful to the members of METU Fuel Cell Technology Dr. Ayşe Bayrakçeken, Dr. Berker Fıçıcılar, Erce Sengül, Dr. R. Gültekin Akay, Aslı Boran, Burcu Güvenatam, Seda Şayin and all my friends for their encouragement and friendship throughout my study.

I would like to thank to the technicians in the machine shop of METU Chemical Engineering Department.

My love Dilek Ergün deserves the greatest thanks for her endless love and great support throughout my studies. She encouraged me whenever I lost faith to the study.

I also thank my family for their support and encouragements during my long education life.

This study was supported by Turkish Boron Institute (BOREN) with project 2009.Ç0219. I feel myself responsible to thank to all of the projects supported our studies which led me to learn about fuel cells. These projects are supported by TUBITAK with Projects MISAG 230, 104M364, and 109M221. METU BAP2004-07-02-00-128 and the State Planning Organization (DPT) Grant No: BAP-08-11-DPT2002K120510 (ÖYP-FBE-BTEK3).

## TABLE OF CONTENTS

ABSTRACT .....	iv
ÖZ .....	vi
ACKNOWLEDGMENTS .....	ix
TABLE OF CONTENTS .....	xi
LIST OF TABLES .....	xvi
LIST OF FIGURES .....	xvii
LIST OF SYMBOLS .....	xxii
LIST OF ABBREVIATIONS .....	xxiv
CHAPTERS .....	1
1. INTRODUCTION.....	1
2. PEM FUEL CELLS .....	6
2.1 Thermodynamics and Electrochemistry of Fuel Cells .....	7
2.2 PEM Fuel Cell Components .....	13
2.2.1 The proton exchange membrane .....	13
2.2.2 Electrically conductive porous backing layer .....	15
2.2.3 Catalyst layer.....	16
2.2.4 Membrane electrode assembly (MEA) .....	17
2.2.5 Current collector (bipolar) plates .....	23
2.2.6 Gasket.....	24
3. FUEL STORAGE and SUPPLY SYSTEMS FOR PORTABLE PEM FUEL CELLS.....	28

3.1 Hydrogen Storage and Supply Systems.....	28
3.1.1 Recent developments in sodium borohydride hydrogen supply for PEMFC systems .....	32
4. EXPERIMENTAL .....	36
4.1 Membrane Electrode Assembly Preparation Technique .....	36
4.1.1 Spray gun method.....	36
4.1.2 Newly developed MEA preparation procedure.....	38
4.1.3 MEAs used for the stacks.....	40
4.2 Bipolar Plate Manufacture.....	42
4.3 Bipolar Plate Coating.....	44
4.3.1 Electrolytic plating .....	45
4.3.2 Coating with soldering .....	46
4.3.3 Coating with conductive composite paint .....	47
4.4 Electrochemical Impedance (EIS) Tests.....	48
4.5 Test Station and Performance Tests .....	49
4.5.1 Procedure for leakage test .....	50
4.5.2 Procedure for operation.....	50
4.5.3 Homemade single cell test station.....	51
4.5.4 Commercial 2kW PEM fuel cell test station.....	53
5. PEM FUEL CELL STACK DESIGN .....	55
5.1 Conceptual Design.....	57
5.1.1 Design basis.....	58
5.1.2 Design strategy .....	59
5.1.3 The mass balance for fuel cell.....	60

5.1.4	The energy balance.....	62
5.1.5	The results of the mass and energy balance.....	62
5.2	Channel and Manifold Design.....	68
5.2.1	Bipolar plate Design 1.....	69
5.2.2	Bipolar plate Design 2.....	70
5.2.3	Bipolar plate Design 3.....	73
5.2.4	Bipolar plate Design 4.....	75
5.3	Flow Modeling.....	76
5.3.1	Flow modeling results of Design 2.....	77
5.3.2	The modeling results of Design 3 and Design 4.....	80
6.	RESULTS and DISCUSSION.....	83
6.1	Results and Discussion for MEA Development.....	83
6.1.1	Performance of MEAs prepared with hand spray coating.....	83
6.1.2	The effect of gas diffusion media on the performance of PEM fuel cell.....	84
6.1.3	The effect of gasket thickness on the performance of PEM fuel cell.....	86
6.1.4	Performance of newly developed MEAs.....	87
6.2	Effect of Contact Resistance on PEMFC Performance.....	93
6.3	Results of Bipolar Plate Coating.....	100
6.3.1	Performance and durability of Ni coated bipolar plates.....	100
6.3.2	Performance and durability of solder (Sn-Ag-Ti) coated bipolar plates.....	102
6.3.3	Performance of graphite-PVDF composite coated bipolar plates.....	104

6.4 Results of PEMFC Prototype Stack .....	110
6.4.1 Performance of Prototype Stack 1.....	110
6.4.2 Performance of Prototype Stack 2.....	113
7. SYSTEM DESIGN AND AUXILIARIES .....	117
7.1 Controller Selection.....	121
7.2 Control Peripheral Cards .....	125
7.2.1 Power management and peripheral driver card.....	125
7.2.2 Cell voltage monitor multiplexer card .....	133
7.3 Air Supply System.....	136
7.4 NaBH <sub>4</sub> Hydrolysis Reactor and H <sub>2</sub> Supply System.....	137
7.5 Power Flow of System.....	138
8. CONCLUSION AND RECOMMENDATIONS.....	140
REFERENCES.....	145
APPENDICES .....	151
A.SAMPLE CALCULATION FOR STACK DESIGN .....	151
A.1 Design Basis .....	151
A.2 Mass Balance.....	152
A.2.1 Inlet flow rates.....	152
A.2.2 Outlet flow rates .....	154
A.3 Energy Balance.....	157
A.3.1 Input .....	157
A.3.2 Output.....	157
A.4 Summary of Results.....	158
A.5 Pressure Drop Calculations .....	159

A.6 Cooling Calculations .....	163
A.6.1 Natural convection .....	165
A.6.2 Radiation .....	166
B.FLOW SIMULATION OF SOLIDWORKS .....	170
B.1 Computational Domain.....	171
B.2 Initial and Boundary Conditions .....	172
B.3 Meshing .....	172
B.4 Solving.....	173
B.5 Time - Dependent Analysis .....	173
CURRICULUM VITAE .....	175

## LIST OF TABLES

### TABLES

Table 2.1 $\Delta G^f$ for the reaction $\text{H}_2 + 1/2\text{O}_2 \rightarrow \text{H}_2\text{O}$ at various temperatures [9] .....	8
Table 2.2 Properties of commercial cation-exchange membranes [11] .....	14
Table 2.3 Structural parameters for the parts of the membrane electrode assembly [15] .....	19
Table 3.1 Comparison of hydrogen storage systems each with 1 kWh of stored energy (~8h of operation of net 100W generating PEM fuel cell system) .....	31
Table 3.2 Summary of the published $\text{NaBH}_4$ hydrolysis catalysts and $\text{H}_2$ generation rates .....	33
Table 4.1 Ultrasonic machine parameters during electrode coating .....	39
Table 5.1 PEM Fuel Cell Stack Design Basis .....	59
Table 5.2 Mass balance table for 117W PEM fuel cell stack .....	63
Table 5.3 Enthalpies of the streams for 117W PEM fuel cell stack .....	64
Table 5.4 Cooling duty with respect to varying ambient temperature (Top = 60 °C) .....	65
Table 5.5 Duty with respect to operating power at 0°C ambient temperature .....	66
Table 6.1 Common electrical elements .....	107
Table 6.2 Comparison of the published performance results of the hydrogen-air PEMFC short stacks and stacks .....	116
Table 7.1 Instrumentation list for the PEM fuel cell system .....	119
Table 7.2 Technical specifications of Cubloc with Cubase32M .....	123
Table 7.3 Switch pair output relation according to the logic status .....	134
Table 8.1 The specifications of the developed and manufactured stacks .....	143

## LIST OF FIGURES

### FIGURES

Figure 2.1 H <sub>2</sub> /O <sub>2</sub> Fuel Cell Ideal Potential as a Function of Temperature [1] .....	9
Figure 2.2 Ideal and Actual Fuel Cell Voltage/Current Characteristic [1] .....	10
Figure 2.3 The schematic view of current path through bipolar plate and gas diffusion layer (left, actual; right, approximation) [6].....	11
Figure 2.4 Classification of membrane materials [11].....	15
Figure 2.5 The schematic exploded view of a membrane electrode assembly (MEA) .....	18
Figure 2.6 The techniques for membrane electrode assembly preparation [17]. .....	21
Figure 2.7 Scanning electron microscope images of the carbon paper (a) before and (b) after hot-pressing [18].....	22
Figure 2.8 Classification of materials for bipolar plates used in PEM fuel cells [2].	24
Figure 2.9 The effect of gasket thickness on the performance of PEM fuel cells. Gasket A: 50 μm, Gasket B: 190 μm, Gasket C: 350 μm, Gasket D: 390 μm, Gasket E: 480 μm [19].....	26
Figure 2.10. Polarization curves for several compression ratios as indicated [19]. ...	27
Figure 3.1 Fuel supply options for fuel cells .....	30
Figure 4.1 MEA Preparation Techniques.....	37
Figure 4.2 A view of the ultrasonic coating machine .....	40
Figure 4.3 The picture of coating machine in action .....	41
Figure 4.4 The picture of the prepared MEAs of the 100W fuel cell stack .....	42
Figure 4.5 The steps for bipolar plate machining .....	43
Figure 4.6 The photographs of (a) CNC router machine and (b),(c) bipolar plate machining.....	44
Figure 4.7 Process for Ni plating on aluminum bipolar plate .....	45

Figure 4.8 Picture of Ni plated aluminum bipolar plate.....	46
Figure 4.9 Graphite-PVDF composite painted aluminum fuel cell test plate having	47
Figure 4.10 The experimental setup for the electrochemical impedance spectrometry measurements.....	48
Figure 4.11. Schematic view of the homemade test station which is used for single cell testing .....	52
Figure 4.12. Photograph of the homemade test station which is used for single cell testing .....	52
Figure 4.13. Photograph of the homemade test station during stack testing.....	53
Figure 4.14 Photograph of the commercial test station which is used for stack testing .....	54
Figure 5.1 The schematic view and reactions of a single PEM fuel cell at ideal conditions .....	56
Figure 5.2 The schematic view and reactions of a single PEM fuel cell at maximum load operating conditions .....	56
Figure 5.3 The schematic view of a PEM fuel cell stack formation and gas feeds and exhausts.....	57
Figure 5.4 Streams that enter and leave the PEM fuel cell stack.....	63
Figure 5.5 Heat dissipation of 117W net electrical power PEM fuel cell stack .....	67
Figure 5.6 Cooling air requirement for 117W net electrical power PEM fuel cell stack at varying ambient temperature .....	67
Figure 5.7 CAD solid model of graphite bipolar plate Design 1 .....	70
Figure 5.8 3D CAD drawing of graphite bipolar plate Design 2.....	71
Figure 5.9 The exploded view of the single cell CAD model for bipolar plate Design 2 and gasket arrangement.....	71
Figure 5.10 CAD Model view of the full stack assembled .....	72
Figure 5.11 A Closer look to the compression mechanism of the stack .....	72
Figure 5.12. 3-D schematic view of the bipolar plate Design 3.....	74
Figure 5.13. 3-D schematic view of the stack Design 3.....	74
Figure 5.14 3-D schematic view of the bipolar plate Design 4.....	75

Figure 5.15 3-D schematic view of the stack Design 4 without the manifolds .....	76
Figure 5.16 Air density profile in air flow channel of bipolar plate Design 2.....	78
Figure 5.17 Air pressure distribution in air flow channels of bipolar plate Design 2	79
Figure 5.18 Air velocity profile of the bipolar plate channel Design 2 .....	80
Figure 5.19 Air density profile of the bipolar plate channel Design 3 and 4.....	81
Figure 5.20 Air pressure distribution of the bipolar plate channel Design 3 and 4 ..	81
Figure 5.21 Air velocity profile of the bipolar plate channel Design 3 and 4.....	82
Figure 6.1 Polarization curve for the fuel cell assembled with the MEA prepared with 20%Pt/C catalyst by hand spraying method .....	84
Figure 6.2. The effect of GDL on the performance of serpentine channeled cell operated at 70°C in stable conditions .....	85
Figure 6.3. The effect of gasket thickness on the performance of serpentine channeled cell with GDL 30BC carbon paper GDL operated at 70°C in stable conditions. ....	86
Figure 6.4 Comparison of the polarization curves of the MEAs produced by membrane coating or GDL coating.....	88
Figure 6.5 Comparison of the polarization curves of the GDL coated MEAs produced by 88 (0.32mg Pt/cm <sup>2</sup> ) pass or 110 pass (0.4mg Pt/cm <sup>2</sup> ) with the same catalyst ink	89
Figure 6.6 The effect of the catalyst Pt content on the performance of the fuel cells having MEAs prepared with ultrasonic coated electrodes.....	90
Figure 6.7 The comparison of the performances of the MEAs produced with 20% and 40% catalyst and commercial MEA.....	91
Figure 6.8 Comparison of the polarization curves of the MEAs produced 40%, 50% or 70% Pt/C catalysts .....	92
Figure 6.9. Exploded view of the single cell assembly for Design 2.....	94
Figure 6.10. Polarization curve of the assembled single cell with oxygen operation – cell voltage was measured two different points .....	96
Figure 6.11. Polarization curve of the assembled single cell with air operation – cell voltage was measured two different points.....	97

Figure 6.12. Comparison of the polarization curves of the assembled single cell with air operation and oxygen operation – cell voltage was at $V_m2$ .....	99
Figure 6.13 Polarization curves for nickel plated aluminum bipolar plates .....	100
Figure 6.14 The change of current density at 0.6V cell potential and the cell resistance for nickel coated fuel cell plates.....	102
Figure 6.15 Polarization curves for Sn-Ag-Ti alloy coated single cell aluminum plates. ....	103
Figure 6.16 The change of current density at 0.6V cell potential and the cell resistance for Sn-Ag-Ti alloy coated single cell aluminum plates.....	104
Figure 6.17 Polarization curves for graphite-PVDF (0.85:0.15) composite coated single cell aluminum plates.....	105
Figure 6.18 Impedances of the cell assembled with a GDL with graphite, graphite-PVDF composite as coated, graphite-PVDF composite as polished after spraying and graphite-PVDF composite as hot pressed at 160°C after spraying.....	109
Figure 6.19 Cell voltage distribution .....	111
Figure 6.20 Polarization curve for the tested stack .....	112
Figure 6.21 Manufactured and assembled fuel cell stack .....	114
Figure 6.22 Polarization curve obtained from the fourth fuel cell stack design .....	115
Figure 7.1 The flow sheet of the 100W Portable PEM Fuel Cell System .....	118
Figure 7.2 Image of Cubloc Cubase 32M board to be used in system controller ....	122
Figure 7.3 Schematic diagram of Cubloc input outputs (I/Os) .....	124
Figure 7.4 The connectors of the peripheral card that is interfaced with Cubloc ....	126
Figure 7.5 Power handling and current sensor block.....	127
Figure 7.6 Pulse width modulation (PWM) driver block.....	128
Figure 7.7 Valve and battery charging enable driver block.....	129
Figure 7.8 Multiplexer logic signal driver block .....	129
Figure 7.9 The pin-out of the multiplexer card interface. ....	130
Figure 7.10 Temperature sensor reading to voltage converter block (PT100 converter block) .....	131
Figure 7.11 Analog isolator used for isolation of cell voltage monitor readings.....	132

Figure 7.12 The photographs of completed fuel cell system controller a) Cubloc controller side b) power management and peripheral driver card side .....	132
Figure 7.13 The schematics of multiplexer circuit.....	133
Figure 7.14 Schematic view of spring pin connections .....	134
Figure 7.15 Interface connector with the peripheral driver board .....	135
Figure 7.16 Cell voltage monitor multiplexer card a) Front view b) Back view .....	135
Figure 7.17 The photograph of the manufactured cell voltage monitor card.....	136
Figure 7.18 Air supply system .....	137
Figure 7.19 NaBH <sub>4</sub> reactor and H <sub>2</sub> supply system.....	138
Figure 7.20 Power flow block diagram.....	139

## LIST OF SYMBOLS

$d_{BP}$	Bipolar plate thickness
$d_C$	Channel depth
$d_{GDL}$	Gas diffusion layer thickness
$E$	Reversible open circuit voltage
$E_{cell}$	Standard potential of the cell
$E_o$	Cell EMF at standard pressure
$F$	Faraday constant
$I$	Current
$i$	Current density
$i_o$	Exchange current density
$i_o^{ref}$	Reference exchange current density
$n$	Number of electrons involved
$P_i$	Partial pressure of component “i”
$V$	Potential (Voltage)
$W_{elec}$	work done by the electrical cell
$W_{max}$	maximum work that can be obtained
$W_C$	Channel width
$W_L$	Landing width
$\Delta G_f$	Change in Gibbs free energy of the process at constant temperature and pressure
$\Delta V_{act}$	Potential loss due to activation loss
$\Delta V_{CR}$	Voltage drop due to interfacial contacts
$\Delta V_{ohm}$	Potential losses due to electronic and ionic resistances
$\Delta V_{trans}$	Potential loss due to gas transport losses
$\phi$	Phase angle

- $\alpha$     Transfer coefficient
- $\gamma$     Pressure coefficient (0.5 to 1)

## LIST OF ABBREVIATIONS

AC	Alternating current
AI	Analog input
AO	Analog output
BAM3G	Ballard Advanced Materials 3 <sup>rd</sup> generation
CL	Catalyst Layer
CNC	Computer Numeric Control
DC	Direct Current
DI	Digital Input
DO	Digital output
EIS	Electrochemical Impedance Spectroscopy
GDE	Gas Diffusion Electrode
GDL	Gas Diffusion Layer
i	Current density
LiPo	Lithium polymer battery
MBS-PBI	Methylbenzensulfonated polybenzimidazoles
MCU	Microcontroller unit
MFC	Mass Flow Controller
MOSFET	Metal–oxide–semiconductor field-effect transistor
MPL	Microporous layer
MUX	Multiplexer
NPI	Naphthalenic polyimide
OCV	Open Circuit Voltage
P4VP	Poly(4-vinylpyridine)
PBI	Polybenz- imidazole
PEI	Polyetherimide
PFCA	Perfluorinated carboxylic acid

PFSA	Perfluorosulfonic acid
PFSI	PerFluoro Sulfonate Ionomer
PLC	Programmable logic controller
Poly-AMPS	poly(2-acrylamido-2-methyl-1-propanesulfonic acid)
PSU(NH <sub>2</sub> ) <sub>2</sub>	Aminated poly- sulfone Udel
PTFE-g-TFS	Sulfoated trifluorostyrene grafted poly(tetrafluoroethylene)
PVA	Polyvinyl alcohol
PVDF-g-PSSA	Poly(vinylidene fluoride) grafted polystyrene sulfonated acid
PWM	Pulse width modulation
RH	Relative humidity
slpm	Standard liter per minute
SPEEK	Sulfonated-polyether-ether-ketone
SPPBP	Sulfonated poly(4-phenoxybenzoyl-1,4-phenylene)
SPSU	Sulfonated polysulfone
V	Cell Potential

## CHAPTER 1

### INTRODUCTION

Fuel cells are electricity generators which convert chemical energy of hydrogen directly to electricity by means of electrochemical oxidation and reduction reactions. While the operation of them is similar to batteries without any mechanical parts, the electricity generation is continuous as the case in mechanical electricity generators. In a typical fuel cell, gaseous fuels are fed continuously to the anode compartment (negative electrode) and an oxidant (i.e., oxygen in air) is fed continuously to the cathode compartment (positive electrode); the electrochemical reactions take place at the electrodes to produce an electric current [1].

Fuel cells attract interests in the last decades as electrical generators from micro power scales to hundreds of kilowatts power scales. There are many types classified by the operation temperature and the electrolyte used. Among the available types, proton exchange membrane (PEM) fuel cells are the most attracted ones. PEM fuel cells are very suitable for portable power generating systems. There is a potential for 100W portable power generators or storages like batteries. The main disadvantages of the energy storage devices such as batteries are their long charging time and low energy densities (energy stored/weight). Using a fuel cell system eliminates the long charging time and increases energy density for larger amount of energy storages.

A single fuel cell produces electricity at 0.5-0.7V on maximum rated power load conditions. In order to produce electricity useful for many applications, many cells must be connected in series to form a fuel cell stack. Fuel cells are in the research

and development phase and many studies are conducted on various parts of them. Especially the component development has been intensively studied by researchers all around the world. However, the studies for the development of fuel cell stack are relatively limited. There are few prototypes developed by companies. New design and prototypes are necessary for future applications.

In order to achieve a PEM fuel cell system, utmost important part is the development of stack and stack components. The stack components are bipolar plates, seals, gaskets and membrane electrode assembly (MEA) which consists of proton exchange membrane, electro-catalyst and gas diffusion layer, and compression end plates.

Bipolar plates are the physical backbone of a fuel cell stack. They conduct the electrons produced by the reaction, distribute the reactants on the active area of the MEA and exchanges heat generated by the reaction with a suitable cooling medium such as air or water. The material of a bipolar plate must have some important properties such as high electrical and heat conductivity, chemical stability, easy and cheap manufacturability. Non-metal, metal and composite materials are used as bipolar plate material. As non-metal material, graphite is widely used for manufacturing of bipolar plates. It has a perfect chemical resistance. Its electrical and thermal conductivity is acceptable. However, it has high manufacturing cost since graphite bipolar plates can be manufactured by computer numeric control (CNC) machining only. Metals have very high electrical and thermal conductivity in bulk. However, the chemical resistance of the metals is not enough to be used in a fuel cell. The contact interface between the bipolar plate and gas diffusion layer loses its electrical conductivity rapidly. In order to prevent the surface from corrosion, some corrosion resistant conductive coatings are applied to the surface of the bipolar plates. Another method of bipolar plate manufacturing is the molding of composite blends such as chemically stable polymer and conductive fillers. As a binder resin, thermoplastics such as polyvinylidene fluoride, polypropylene, polyethylene and thermosets such as, epoxy, phenolic, furan resins and vinyl esters might be used [2].

Metallic bipolar plates are relatively much cheaper than graphite bipolar plates. Therefore, new materials and coatings need to be searched.

Sealing material used and its application to eliminate gas leakage are the cumbersome part of fuel cell stack assembling. Gasket has many functions in a fuel cell. Its primary role is sealing the reactant intermixing and leaking to the surrounding. It also determines the amount of compression on the GDL and affects the contact resistance between the GDL and bipolar plate. It was found in Middle East Technical University Fuel Cell Technology Laboratory that the thickness of the gasket material is extremely important for a fuel cell performance. Lin et.al. [3] have optimized gasket thickness by comparing the performances of PEMFC working with five different gaskets. Increasing compression on gas diffusion layer causes a reduction on gas permeability and contact resistance. Compression ratio should be optimized to maximize the cell performance.

Composite materials, steel, and aluminum might be used as compression end plate material. The material used, its thickness and design should be convenient. An appropriate mechanical design that leads to the compression on the cells is required.

The membrane electrode assembly is the most important part of a PEM fuel cell stack. Its components (catalyst, membrane, gas diffusion layer) and preparation technique significantly affect the performance of the fuel cell. A previously developed technique has been applied for many years by Middle East Technical University Fuel Cell Research Center (FCRC) group [4, 5]. This technique is spraying of catalyst ink with air pressure atomizing spray brush (air brush) onto the microporous layer coated side of the gas diffusion layer. The nature of the manufacturing technique is strongly dependent on the manual operation of the operator. Therefore, the produced membrane electrode assemblies are not identical with this method. This method is also not applicable for larger active area and large number of membrane electrode assemblies, since considerable amount of material is

lost during manufacturing. In order to improve the performance and enable consistent quality membrane electrode assemblies, a new method should be implemented.

Fuel cells are systems that require many sensors, compressors, pumps, fans etc. Therefore, there is a need for a controller for such a system. An applicable control system is the cell voltage monitoring (CVM) system. Even one of the cells potential reduces below to a certain voltage like below 0.4V or cell voltage reversal occurs due to fuel or oxidant starvation, the stack must be closed in order to prevent the cell from damage. Therefore, all cells of the stack have to be monitored for the safe operation of the fuel cell. Electronic control cards should be designed and manufactured to supply necessary interface between the controller and fuel cell and balance of plant.

A device or machine is defined as portable if it can be easily carried or moved. According to Barbir [6], the term “portable power system” is not sharply defined. These devices might be divided in two categories as battery replacements which are under 100W and portable power generators up to 1kW. There are many applications which can be run with fuel cells having small power (<100W). Some of these applications are military portable power, unmanned vehicles, military radios, battery chargers, emergency lights, nautical devices, wheelchairs, laptops, flash lights etc. The use of a fuel cell instead of a battery brings important advantages such as elimination of charging time and increased energy density. These advantages are especially invaluable for military systems. The operation times are limited by the energy stored. An unmanned air vehicle (UAV) has an operation time of 1-4 hours with the use of batteries. The use of a portable fuel cell system may extend the operation time to 3-4 times longer than batteries.

One of the most important problems of a portable fuel cell system is the storage of the fuel necessary for the system. The storage of hydrogen in gas form requires high

pressure vessels which is not suitable for a portable system. Not only the weight of the pressure vessel is high but also the refilling becomes complicated for a portable low power system. Another option is to store the hydrogen in metal hydride cartridges. This option partially solves the problem of refilling. However, the weight of these cartridges is too high for a portable low power fuel cell system. Direct feed of liquid fuels (methanol, ethanol) are also studied. However, the state of the fuel cell polymer electrolyte technology is not ready for using such fuels directly. On site hydrogen production technologies might be used for supplying the necessary hydrogen to the fuel cell. This option brings high energy density and safe storage of hydrogen. Among the choices of onsite hydrogen production from methanol, alcohol or other hydrocarbon fuels, aqueous solution of sodium borohydride is the most promising alternative for a portable 100W power PEM fuel cell system due to its easily controllable excellent kinetic properties and pure hydrogen release as a result of the reaction.

The aim of this thesis is to design and manufacture a PEM fuel cell stack which can be used for portable applications. The PEM fuel cell stack is planned to be incorporated to a NaBH<sub>4</sub> hydrolysis reactor for H<sub>2</sub> supply. Within the scope of this thesis a new coating technique is developed for MEA manufacturing. New metal bipolar plates are designed and manufactured by CNC technique. A control system is developed for fuel supply and system control.

## CHAPTER 2

### PEM FUEL CELLS

Proton exchange membrane (PEM) or polymer electrolyte (PE) fuel cells are the most common type of fuel cell which can be applied to many types of application. The key technology leading these fuel cells is the development of a solid polymeric ion conducting membranes. These fuel cells are compact and have high energy density.

Although the fuel cells known for more than a century, the first prototype of PEMFC was produced by General Electric (GE) in 1963. A 1 kW system was realized for the Gemini mission of NASA with a sulfonated polystyrene membrane as polymer electrolyte, the cell was operated with pure H<sub>2</sub> and O<sub>2</sub>. In 1969 Nafion® (DuPont) was used as electrolyte in a GE fuel cell for the first time. In the 1980s Ballard Company used a proton exchange membrane produced by DOW Chemical. A five-cell-stack using air as oxidant was presented in 1988 by similar systems of varying power were used by Ballard [7].

As introduced by Kirk Othmer [8], the advantages of PEMFCs are that they do not contain free corrosive liquid in the cell, the fabrication of the cells is simple, they are able to withstand large pressure differentials, their materials corrosion problems are minimal, and they demonstrate long life.

On the other hand, the disadvantages of PEMFCs are that the fluorinated polymer electrolyte is traditionally expensive, water management in the membrane is critical

for efficient operation, and long-term high performance with low catalyst loadings in the electrodes needs to be demonstrated.

The reactions involved in the PEM fuel cells are given in Equations 2.1 and 2.2.



Then, the standard potential of the cell becomes  $E_{\text{cell}} = 1.229 \text{ V}$ .

## 2.1 Thermodynamics and Electrochemistry of Fuel Cells

For an electrochemical cell the maximum work that can be obtained is equal to the change in Gibbs free energy of the process at constant temperature and pressure as given in Equation 2.3. That is,

$$W_{\text{max}} = \Delta G_f \quad (2.3)$$

The maximum work is obtained if the process is sufficiently slow that there is no irreversibility. The electrical potential produced by the cell is referred as zero-current cell potential ( $E$ ). The work done by the electrical cell  $W_{\text{elec}}$ , in moving  $n$  moles of electrons across a potential difference of  $E$  is given in Equations 2.4 and 2.5.

$$W_{\text{elec}} = -nFE \quad (2.4)$$

$$\text{Since } \Delta G_f = W_{\text{elec}} = -nFE \quad (2.5)$$

and  $n=2$  for a hydrogen fuel cell. Then the fundamental equation which gives the reversible zero-current voltage or reversible open circuit voltage  $E$  becomes as given in Equation 2.6,

$$E = \frac{-\Delta G_f}{2F} \quad (2.6)$$

where  $F$  is the Faraday constant and equal to 96485C. The values of the  $\Delta G_f$  for the reaction  $H_2+1/2O_2 \rightarrow H_2O$  at various temperatures are given in Table 2.1.

Table 2.1  $\Delta G_f$  for the reaction  $H_2+1/2O_2 \rightarrow H_2O$  at various temperatures [9]

Form of water product	Temperature (°C)	$\Delta G_f$ (kJ mol <sup>-1</sup> )
Liquid	25	-237.2
Liquid	80	-228.2
Gas	80	-226.1
Gas	100	-225.2
Gas	200	-220.4
Gas	400	-210.3
Gas	600	-199.6
Gas	800	-188.6
Gas	1000	-177.4

From the values of  $\Delta G_f$  listed in Table 2.1, the ideal potential of a  $H_2/O_2$  fuel cell as a function of temperature can be plotted as in Figure 2.1.

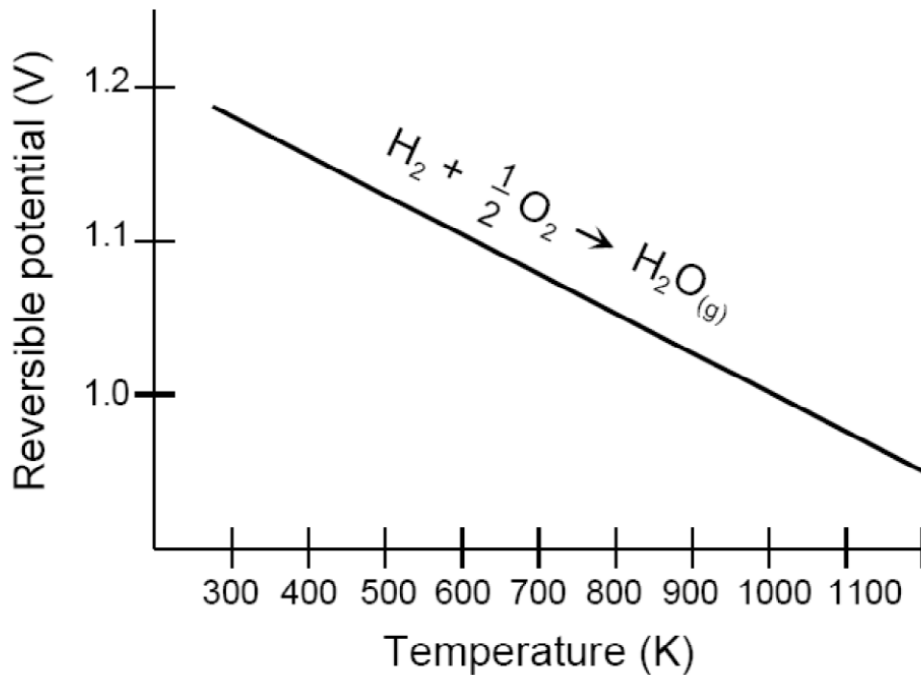


Figure 2.1 H<sub>2</sub>/O<sub>2</sub> Fuel Cell Ideal Potential as a Function of Temperature [1]

The pressure and concentration of the reactants affect the Gibbs free energy, and thus the voltage. This situation can be described by Nernst equation given in Equation 2.7.

$$E = E^0 + \frac{RT}{2F} \ln \left( \frac{P_{H_2} \cdot P_{O_2}^{\frac{1}{2}}}{P_{H_2O}} \right) \quad (2.7)$$

where  $E^0$  is the cell EMF at standard pressure.

Ideal voltage of the cell could not be reached even at the open circuit (zero-current) conditions for the actual operation of a fuel cell. The total loss of the cell voltage is composed of activation polarization loss, ohmic polarization loss, and the concentration polarization loss. A typical polarization curve containing the listed losses is given in Figure 2.2.

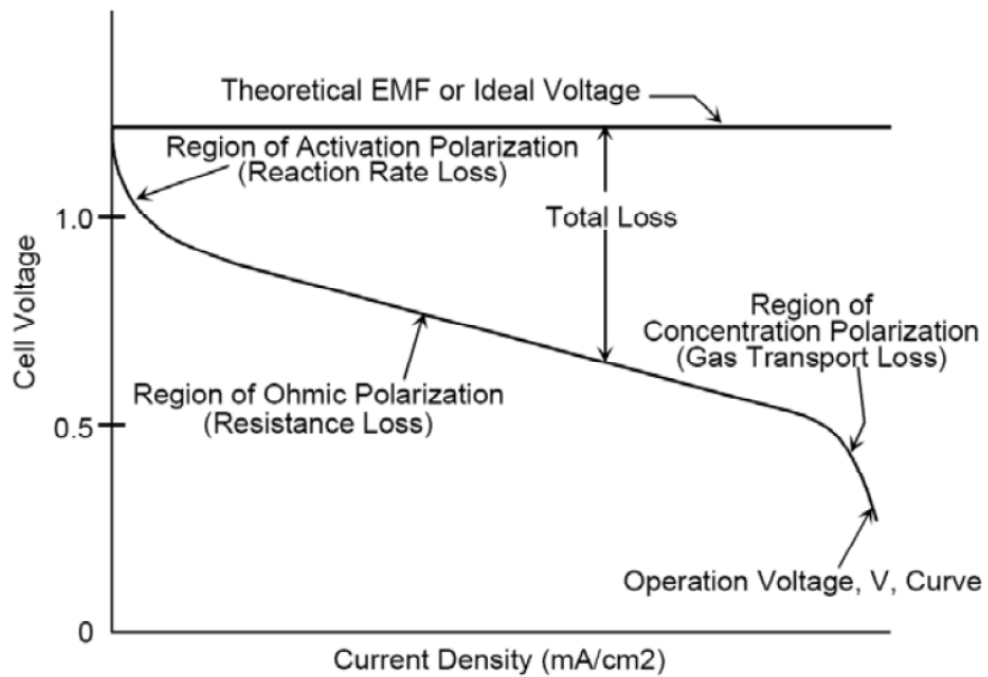


Figure 2.2 Ideal and Actual Fuel Cell Voltage/Current Characteristic [1]

The overall irreversibility and the resulting voltage loss can be described as in Equation 2.8.

$$V = E - \Delta V_{ohm} - \Delta V_{act} - \Delta V_{trans} \quad (2.8)$$

Ohmic polarization losses include electronic resistances occurring in the interfaces, the bulk of GDL and the bipolar plates, and ionic resistances occurring in the ionomer. The electron path in a fuel cell is shown in Figure 2.3. In the cross-sectional view dark grey drawing is the bipolar plate (BP), the white parts are the flow channels, gas diffusion layer (GDL) is the grey layer below bipolar plates and the bottom part is the catalyst layer (CL).

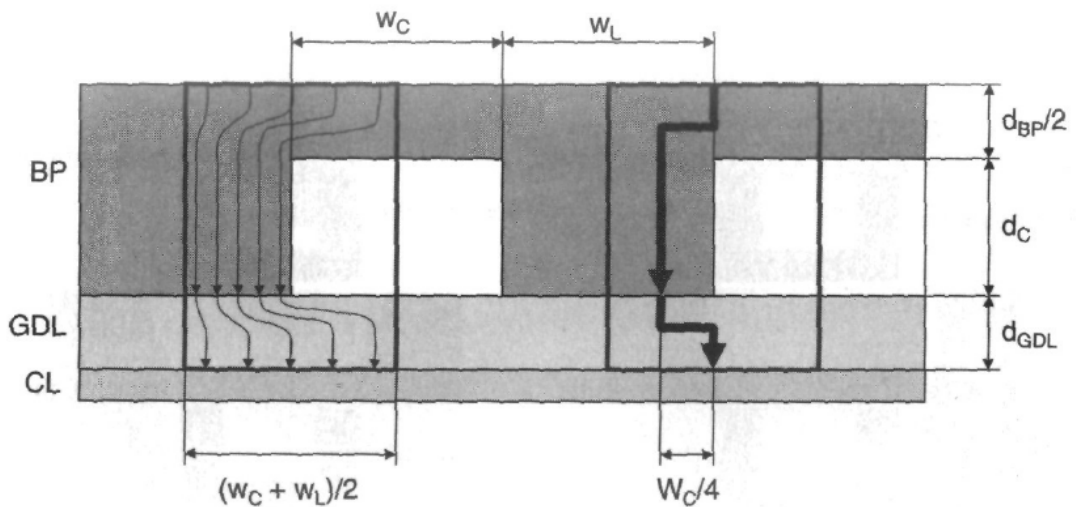


Figure 2.3 The schematic view of current path through bipolar plate and gas diffusion layer (left, actual; right, approximation) [6].

For a geometry shown in Figure 2.3, and with simplification of the current path in the control area {shown in rectangle) the voltage loss through the control area is shown in Equation 2.9.

$$\Delta V = \Delta V_{BP} + \Delta V_{GDL} + \Delta V_{CR} \quad (2.9)$$

Where;  $\Delta V_{BP}$  is the voltage drop through the bipolar plate,  $\Delta V_{GDL}$  is the voltage drop through gas diffusion layer, and  $\Delta V_{CR}$  is the voltage drop due to interfacial contacts which is given by Equation 2.10.

$$\Delta V_{CR} = R_{CR} \frac{W_L + W_C}{W_L} i \quad (2.10)$$

Therefore, the minimum value for the contact resistance is obtained for  $W_C=0$  and for any value of  $W_C>0$ ,  $\Delta V_{CR}>R_{CR}i$ . That is, when there is no channel, the contact resistance is minimized. In addition to this, components may be manufactured more economically since flat plate is more economical to produce. It also reduces the thickness of a cell and consequently reduces the height of a stack of fuel cells. The uniform distribution of the reactants through catalyst layers is also achieved [10].

Substituting ohmic, activation and transport voltage losses into Equation 2.8 one gets Equation 2.11.

$$V = E - ir - A \ln \left( \frac{i + i_n}{i_0} \right) + m \exp(ni) \quad (2.11)$$

where,  $E$  is the reversible open circuit voltage (OCV), for a typical PEM fuel cell operating at room temperature  $E$  is about 1.2 V. Reversible OCV is a function of temperature which is given in Figure 2.1.  $i$  is the current density, that is, the current generated per unit active area of the fuel cell. The value of the current density is dependent on the electrical load applied at that instant. For the commercial fuel cells, the typical value of the current density is 1 A/cm<sup>2</sup> at 0.6 V operational voltages,

currently.  $i_n$  is the internal and fuel crossover equivalent current density,  $i_0$  is the Exchange current density at an electrode/electrolyte interface which has a typical value of  $0.1 \text{ mA/cm}^2$  for a low temperature hydrogen-fed fuel cell running on air at ambient pressure for platinum catalyst.  $A$  is the slope of the Tafel line having a typical value of  $0.06 \text{ V/decay}$ ,  $m$  and  $n$  are the constants in the mass transfer overvoltage. The value of  $m$  is typically about  $3 \times 10^{-5} \text{ V}$  [9]. Finally,  $r$  is the area specific resistance which has a value of less than  $1 \text{ ohm/cm}^2$  typically.

## 2.2 PEM Fuel Cell Components

The main components of a PEM fuel cell stack are proton exchange membranes, electrically conductive porous backing layers, electro-catalyst layers (the electrodes) which are plates at the interface between the backing layer and the membrane – the combination of these layers are called as membrane electrode assembly-, bipolar plates and gaskets [1].

### 2.2.1 The proton exchange membrane

The different companies producing polymer electrolyte membranes have their own special tricks, mostly proprietary. However, a common theme is the use of sulphonated fluoro-polymers, usually fluoroethylene. The most well known and well established of these is Nafion<sup>®</sup> (Dupont), which has been developed through several variants since the 1960s. This material is still the electrolyte against which others are judged, and is in a sense an “industry standard”. Other polymer electrolytes function in a similar way [9]. A comparison of some commercial cation-exchange membranes is provided in Table 2.2.

Table 2.2 Properties of commercial cation-exchange membranes [11]

Membrane	Membrane type	IEC (mequiv./g)	Thickness (mm)	Gel water (%)	Conductivity (S/cm) at 30 °C and 100% RH
<i>Asahi Chemical Industry Company Ltd., Chiyoda-ku, Tokyo, Japan</i>					
K 101	Sulfonated polyarylene	1.4	0.24	24	0.0114
<i>Asahi Glass Company Ltd., Chiyoda-ku, Tokyo, Japan</i>					
CMV	Sulfonated polyarylene	2.4	0.15	25	0.0051
DMV	Sulfonated polyarylene	–	0.15	–	0.0071
Flemion	Perfluorinated	–	0.15	–	–
<i>Ionac Chemical Company, Sybron Corporation, USA</i>					
MC 3470	–	1.5	0.6	35	0.0075
MC 3142	–	1.1	0.8	–	0.0114
<i>Ionics Inc., Watertown, MA 02172, USA</i>					
61AZL386	–	2.3	0.5	46	0.0081
61AZL389	–	2.6	1.2	48	–
61CZL386	–	2.7	0.6	40	0.0067
<i>Du Pont Company, Wilmington, DE 19898, USA</i>					
N 117	Perfluorinated	0.9	0.2	16	0.0133
N 901	Perfluorinated	1.1	0.4	5	0.01053
<i>Pall RAI Inc., Hauppauge, NY 11788, USA</i>					
R-1010	Perfluorinated	1.2	0.1	20	0.0333

The classification of the membrane materials used for fuel cells is given in Figure 2.4. Membrane materials researched for PEM fuel cells fall into different membrane systems, which can be classified as perfluorinated ionomers, partially fluorinated polymers, non-fluorinated membranes with aromatic backbone, non-fluorinated hydrocarbons, acid–base blends and composite membranes.

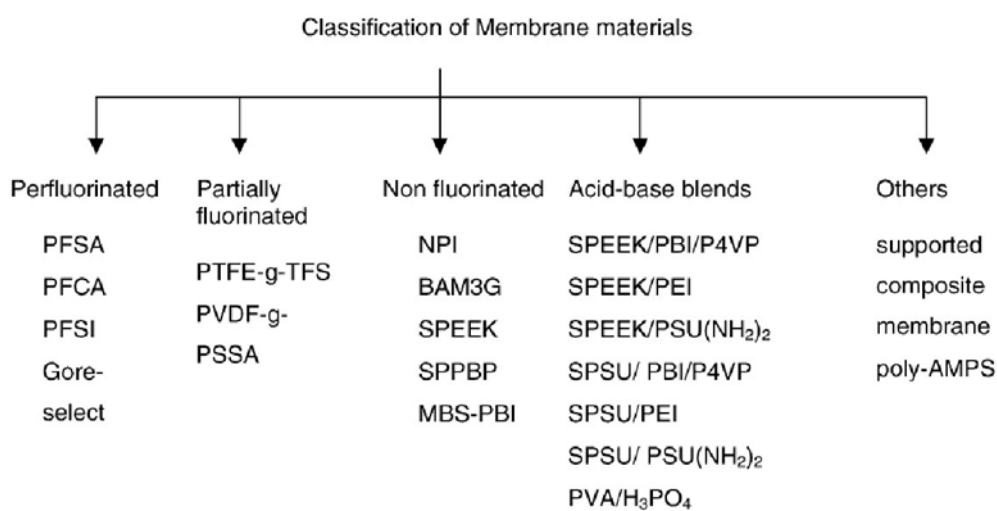


Figure 2.4 Classification of membrane materials [11].

### 2.2.2 Electrically conductive porous backing layer

This backing layer is also widely referred to as gas diffusion layers or current collectors. The polymer membrane and electrodes are sandwiched between two sheets of porous backing media. The functions of the backing layer are such as; acting as a gas diffuser, providing mechanical support, providing an electrical pathway for electrons and channeling for product water away from the electrodes. The importance of this layer is to provide a balance between the electron transfer and reactant and product transfers.

The backing layer is typically carbon-based, and may be in cloth form, or carbon paper which is a non-woven pressed carbon fiber configuration, or simply a felt-like material. The layer incorporates a hydrophobic material, such as poly tetra fluoro ethylene. The function of poly tetra fluoro ethylene is to prevent water from “pooling” within the pore volume of the backing layer so that gases freely contact the catalyst sites. Furthermore, it facilitates product water removal on the cathode as it creates a non-wetting surface within the passages of the backing material [1].

### 2.2.3 Catalyst layer

The heart of the proton exchange membrane fuel cell (PEMFC) is the membrane electrode assembly (MEA) which consists of two catalyst layers at the two sides of the proton conducting membrane. These two catalyst layers play a critical role on the performance of the MEA [12].

As with any heterogeneous catalyst material, a number of fundamental requirements are necessary for good performance. These include high intrinsic activity of sites for the reaction and a maximum number of these sites. Additional requirements for fuel cells are high electrical conductivity, good interaction with the ionomer, reactant gas access to active sites and stability in contact with reactants, products and electrolytes [12].

Both of the anode and cathode is composed of platinum-based catalysts. To promote hydrogen oxidation, the anode uses either pure platinum metal catalyst or, as is common in most modern PEMFC catalysts, a supported platinum catalyst, typically on carbon or graphite for pure hydrogen feed streams. For other fuels, such as reformat (containing H<sub>2</sub>, CO<sub>2</sub>, CO, and N<sub>2</sub>), the desired catalyst is an alloy of platinum containing ruthenium. Oxygen reduction at the cathode may use either the platinum metal or the supported catalyst [1, 13].

Although pure hydrogen can be fed to the anode, the stream may include CO and CO<sub>2</sub> also because of the economical reasons production method conducted. Also on site generation of hydrogen, namely, reformation of hydrocarbons would contain a significant amount of CO and CO<sub>2</sub>. It is well known that CO binds to platinum irreversibly which results to deactivation of the catalyst due to the loss of the active sites. Although the effect of CO<sub>2</sub> is not significant as CO, the reverse water-gas shift reaction produces CO from CO<sub>2</sub>. The most elegant way to overcome anode poisoning is through the development of CO and CO<sub>2</sub>-tolerant electro catalysts, which are capable of operating in the presence of at least 100 ppm CO and 20-25% CO<sub>2</sub>, [14].

#### 2.2.4 Membrane electrode assembly (MEA)

Membrane electrode assembly (MEA) is the core of a PEM fuel cell. The reactions take place in the electrodes of the MEA. It is composed of a proton conducting membrane, electrode layers, micro porous layers and gas diffusion layers as illustrated in Figure 2.5. Beside the components of MEA, the fabrication technique of MEA also affects the performance and efficiency. MEA can be built in 3 layers consisting of electrode-membrane-electrode or in 5 layers consisting of gas diffusion layer-electrode-membrane-electrode-gas diffusion layer or in 7 layers containing gasket layers over the highest level in addition to 5 layers MEA.

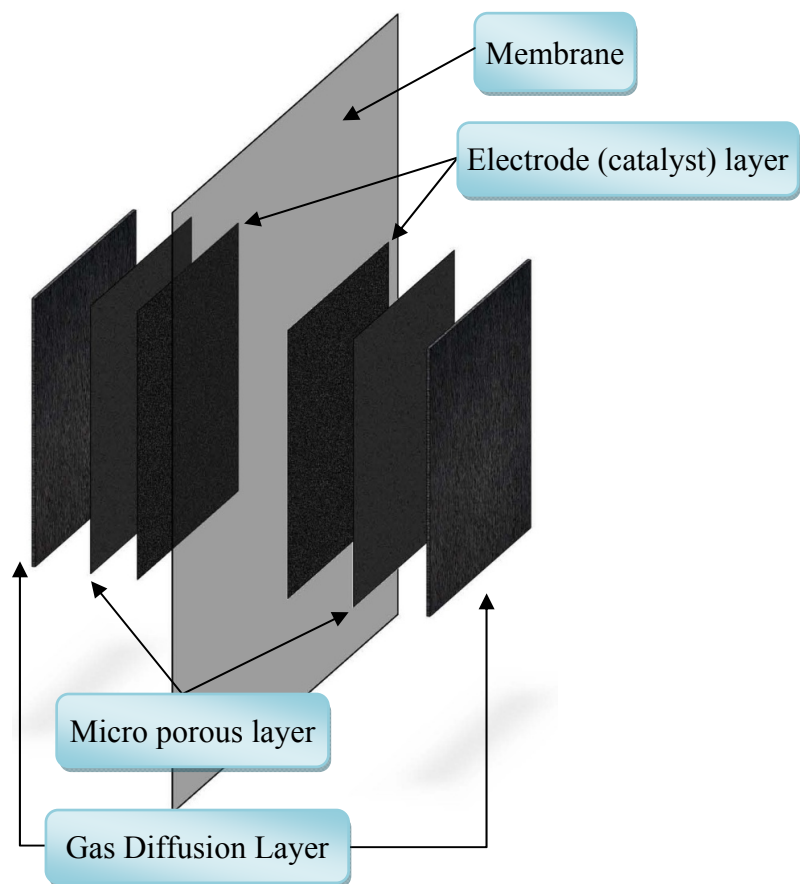


Figure 2.5 The schematic exploded view of a membrane electrode assembly (MEA)

The micro porous layer is generally formed on the gas diffusion layer. Its functions are accepted as it provides high electrical conductivity between catalyst layer and gas diffusion layer, and keeps the membrane from fast dry-out at low current density conditions [15]. The micro porous layer and gas diffusion layer is preferred to be treated with PTFE in order to facilitate the transport produced water to the gas channels [16]. The optimum PTFE loading for micro porous layer is suggested as 20 wt.% for using air at the cathode [16]. There are two approaches for the preparation of the catalyst layer which are coating either onto the membrane or micro porous

layer on the gas diffusion layer. The structural parameters of these three layers are shown in Table 2.3.

Table 2.3 Structural parameters for the parts of the membrane electrode assembly [15]

	Catalyst Layer (CL)	Micro porous Layer (MPL)	Gas diffusion Layer (GDL)
Porosity, $\epsilon$	20–30% <sup>a</sup>	50%	70–80% <sup>b</sup>
Mean pore radius	0.05 $\mu\text{m}$	0.5 $\mu\text{m}$	10 $\mu\text{m}$
Thickness, $L$	10–50 $\mu\text{m}$	10–100 $\mu\text{m}$	200–400 $\mu\text{m}$

<sup>a</sup> Dry base

<sup>b</sup> Uncompressed

The fabrication technique of an MEA may significantly affect the performance of a PEM fuel cell. There are many techniques either published in the literature or used by the companies as proprietary techniques. The formulation, the application, the route followed results difference in performance and durability of the MEAs. Figure 2.6 illustrates MEA manufacturing techniques. Some of the techniques require advanced equipment and special skills.

Catalyst layer is applied either on membrane or gas diffusion layer. Wet thin film methods are widely and easily used for the manufacturing of membrane electrode assemblies. In the spraying method, a pneumatic spray gun is used for coating the catalyst to the hydrophobic treated layer of the gas diffusion media. Once a single ultra thin layer was coated, the surface is dried by a hot air gun set at 80 °C or infrared heating lamp. This coating-drying cycle is repeated many times. The catalyst coated gas diffusion layer (GDL) is weighted in order to determine if the desired

catalyst load is reached or not. When the desired load is reached for anode and cathode, the catalyst coated GDLs are hot pressed onto the both sides of the Nafion<sup>®</sup> membrane. Another technique involves the use of Teflon sheet as an electrode transfer medium. First, catalyst ink is sprayed described in Method 1, and the electrode is transferred to Nafion<sup>®</sup> membrane by hot pressing the electrode coated Teflon sheet to the membrane. The third method is the application of spray method directly to the Nafion<sup>®</sup> membrane placed on a heated vacuum table kept at 80 °C.

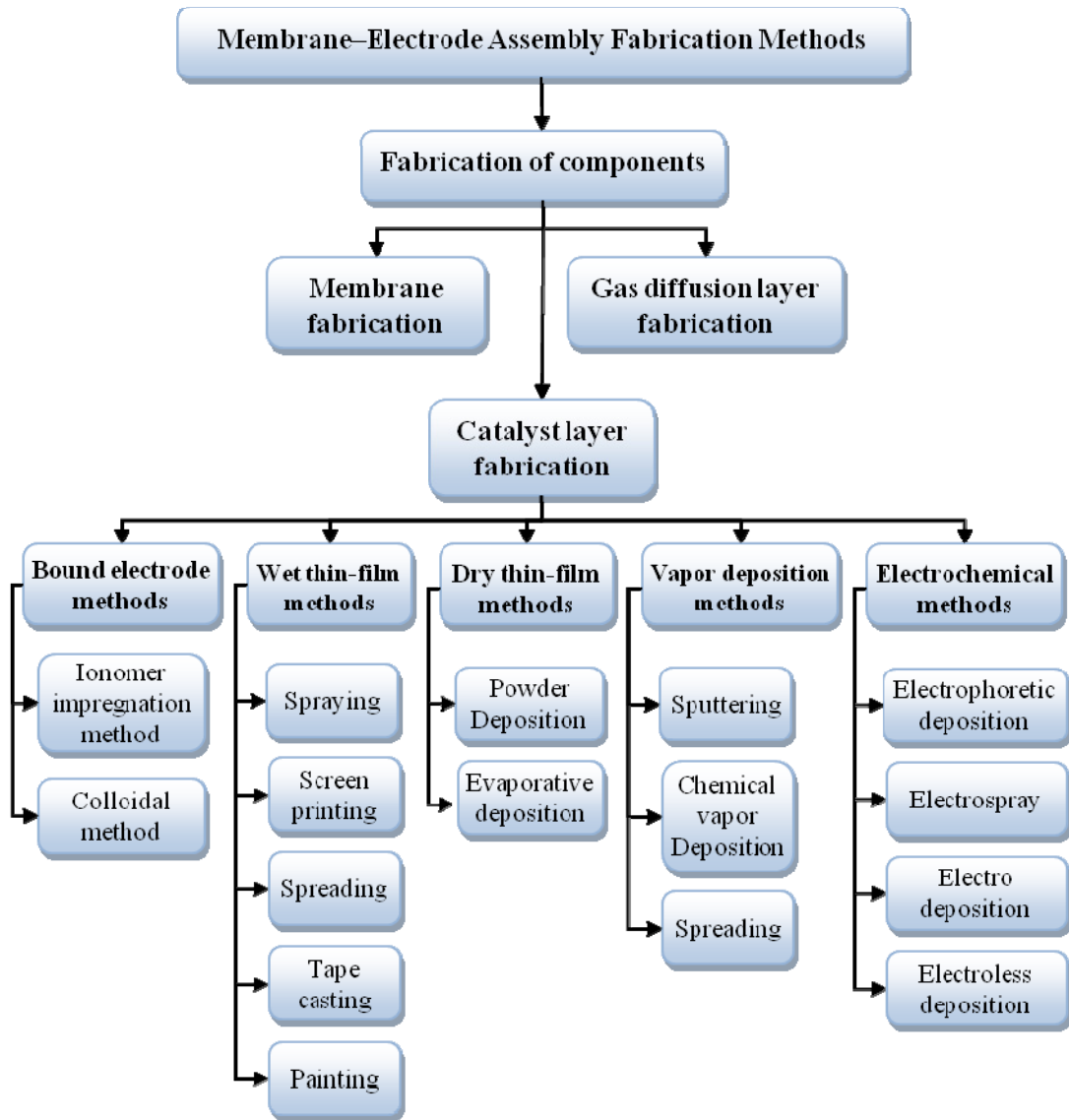


Figure 2.6 The techniques for membrane electrode assembly preparation [17].

Zhang et.al [18] investigated the effects of membrane electrode assemblies (MEAs) fabrication methods (spraying and scraping methods) and the hot-pressing pretreatment of anode electrodes on the performance of direct methanol fuel cells (DMFCs). The scraping method proved to be a little more profitable for improving

the cell performance than the spraying method. It was also found that the hot-pressing pretreatment of the anode electrode decreased the performance of the MEA due to the difficulty for electrons and mass transport in the anode electrode, namely the increase of internal cell resistance. The SEM images of the carbon paper before (Figure 2.7a) and after (Figure 2.7b) the hot pressing pretreatment at 80 kgf/cm<sup>2</sup> is given. It can be seen that the long carbon fibers are crushed into pieces after the hot-pressing pretreatment. So the resistance of MEA is increased due to the breaking of the carbon fibers which are used as the electron transport supports in the carbon paper.

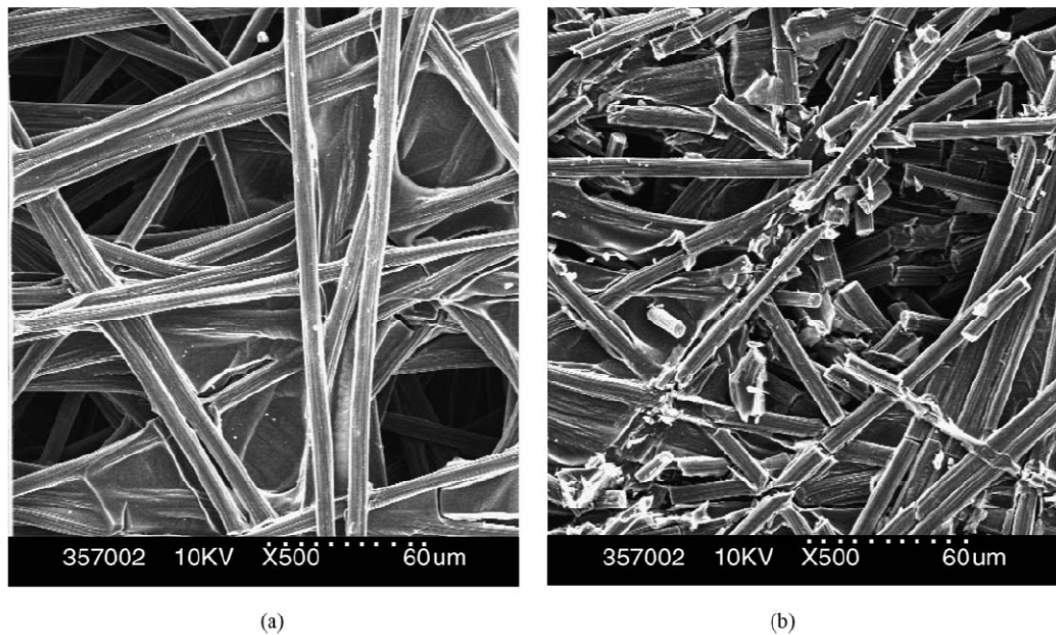


Figure 2.7 Scanning electron microscope images of the carbon paper (a) before and (b) after hot-pressing [18].

Bayrakçeken et.al [4] investigated the effect of hot pressing pressure for the MEA preparation on the performance of PEM fuel cell. The pressure of the hot press was

changed from 0 kgf/cm<sup>2</sup> to 52.7 kgf/cm<sup>2</sup>. The optimum pressure on the MEA during hot pressing was found to be 17.5 kgf/cm<sup>2</sup>.

#### 2.2.5 Current collector (bipolar) plates

Many cells have to be connected and stacked in series in order to reach the desired power and voltage. For this purpose bipolar plates are manufactured. They are used for transporting the electrons produced in a cell to cell connected in series, being a carcass of the fuel cell, supplying reactants to electrodes and remove the products from the electrodes, and being a heat exchanging medium to cool the fuel cell stack.

The necessary properties of these plates are high electrical and heat conductivity, good mechanical strength, high chemical stability, easy machining, lightness, and low cost.

The detailed classification of bipolar plate materials is shown in Figure 2.8. It is possible to make bipolar plates from metals, graphite and composite materials. Metal bipolar plates are usually heavier than the graphite and composite plates. They have low chemical stability although they have very high electrical and heat conductivity. Coatings can be applied over the surface of the metals to improve chemical stability. However, it is not possible to prevent the corrosion of metal completely. Graphite is a chemically stable material that can be used as a bipolar plate. It is light and has sufficient thermal and electrical conductivities. However, it is not suitable for mass production since it is quite abrasive. Another possible material to prepare bipolar plates is graphite polymer composite. It is preferred because of its relatively low cost, suitability for injection molding and its acceptable thermal and electrical conductivities.

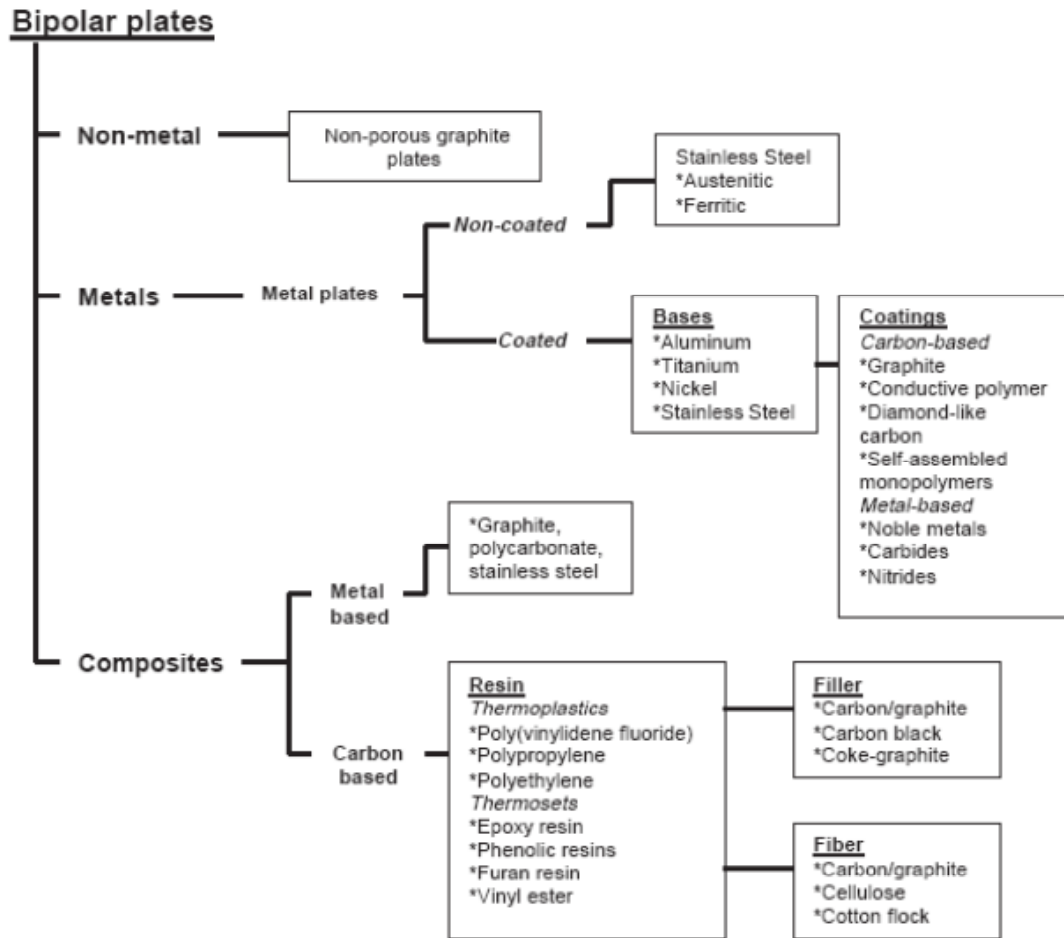


Figure 2.8 Classification of materials for bipolar plates used in PEM fuel cells [2].

### 2.2.6 Gasket

One of the fuel cell components that have to be developed is the gasket. Gasket has many roles in a fuel cell. First and primary role is that they seal the reactants and prevents them from intermixing and leaking to the surrounding. Second it determines the amount of compression of the GDL and the contact resistance between the GDL

and bipolar plate. Third, it prevents the bipolar plates from short-circuiting electrically.

The fuel cell researchers generally underestimate gasket in a fuel cell research. There are a few published material related to gaskets especially for low temperature PEM fuel cells. However, it was found that the thickness of the gasket material is extremely important for a fuel cell performance. Lin et.al [3] also indicates and optimizes the effect of gasket thickness with five different gaskets. The compression of a gas diffusion layer reduces gas permeability and contact resistance. The results provide an optimum value of compression ratio that maximizes the cell performance. The results concerning the balance between compression and performance provide vital information for the fabrication of stacks and support for industrial applications.

Zhou [19] showed the polarization curves at different compression ratios for the contact resistance of 1648mΩ-cm (see Figure 2.10). They found that the voltage increases with increasing compression due to the decrease in the ohmic over-potential. It is shown that there exists an optimal compression displacement (0.0555 mm). The limiting current decreases with an increase in the GDL compression deformation.

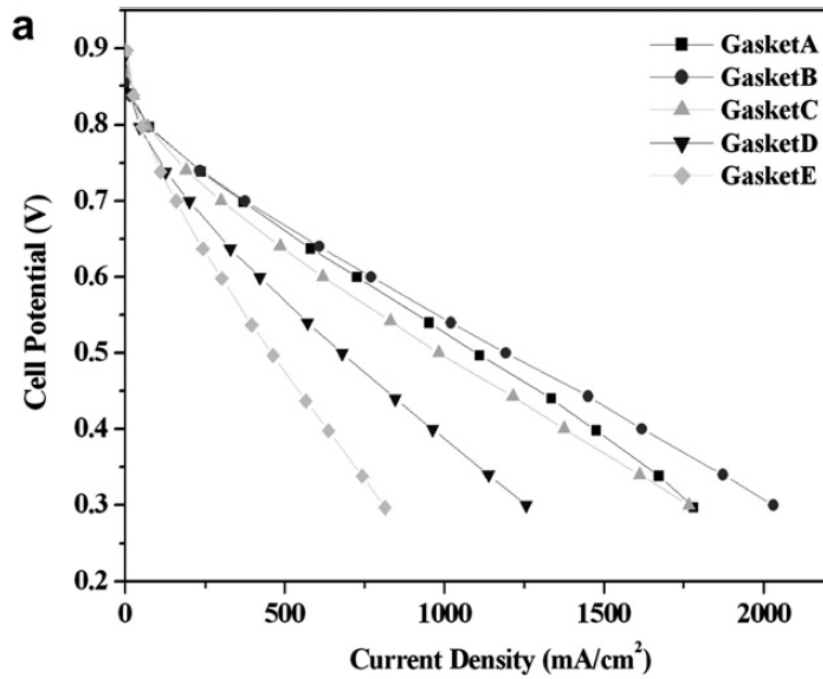


Figure 2.9 The effect of gasket thickness on the performance of PEM fuel cells. Gasket A: 50  $\mu\text{m}$ , Gasket B: 190  $\mu\text{m}$ , Gasket C: 350  $\mu\text{m}$ , Gasket D: 390  $\mu\text{m}$ , Gasket E: 480  $\mu\text{m}$  [19]

Tan [20] has investigated the in-situ degradation of four commercially available gasket materials in a PEM fuel cell environment. Silicone S and Silicone G degradation was judged by mass loss and cracking, in either ADT or regular FC solutions at 80 and 60°C EPDM and fluoro-elastomer have shown insignificant degradation up to 45 weeks exposure to the ADT solution at bend angle of 120°.

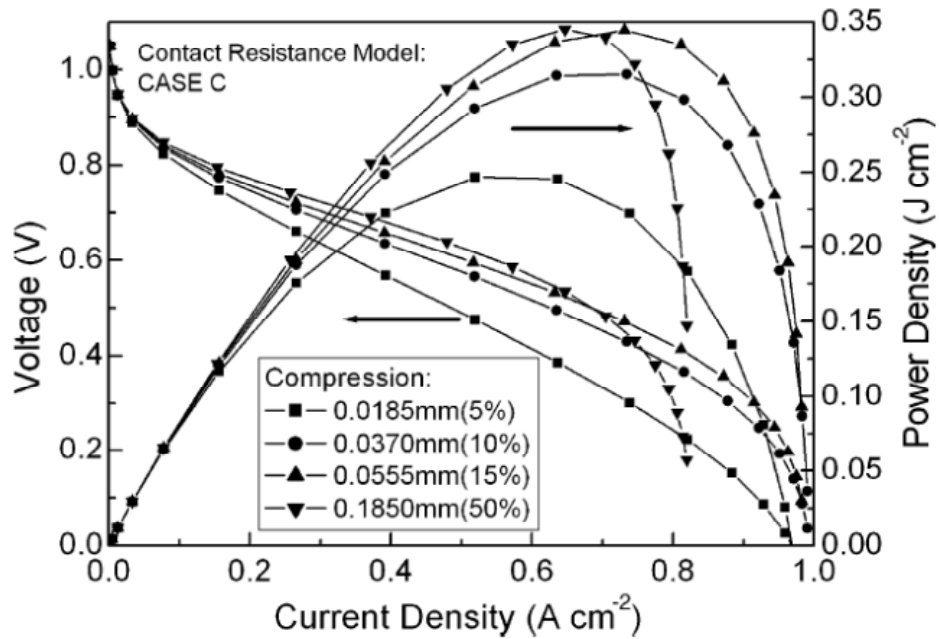


Figure 2.10. Polarization curves for several compression ratios as indicated [19].

Cleghorn [21] focused on a life test of a fuel cell which lasts three years. Although the main test concern was the MEA failure mechanism, they have found that on disassembly of the cell, the only visual change in the cell was the apparent degradation of the silicone/glass re-enforced gasket. Upon measurement, the gasket thickness was typically reduced by approximately  $25\mu\text{m}$ . This silicone degradation was so severe at active area edges, that in these areas only the glass re-enforcement remained. Silicone particles from the gasket were also observed on the surface of the gas diffusion media. He has concluded that gasket degradation affected the fuel cell performance by the increased load on the gas diffusion media, leading to decreased porosity and increased reactant transport resistance, increased hydrophilic behavior of the gas diffusion media, and poisoning of the catalysts by the degradation materials.

## CHAPTER 3

### FUEL STORAGE and SUPPLY SYSTEMS FOR PORTABLE PEM FUEL CELLS

Definition of portable is a device that can be carried by a firefighter. However, a portable fuel cell is not defined well in terms of power, weight or dimensions. Hoogers [12] defines PEM fuel cells delivering less than 1kW of power as portable. Barbir [6] divides this portable fuel cells into two categories as battery replacement portable fuel cells having less than 100W power and portable power generators which are between 100W and 1kW power. Agnolucci [22] states portable fuel cells as systems which weight up to 10kg and power up to 5kW.

#### 3.1 Hydrogen Storage and Supply Systems

Fuel storage and supply system are the important problems against the fuel cell commercialization. Especially, low power portable fuel cell systems (0-500W) require low weight fuel supply systems. Hydrogen has the lowest gas density and the second lowest boiling point of all known substances, making it a challenge to store as either a gas or a liquid. As a gas, it requires very large storage volumes and pressures. As a liquid, it requires a cryogenic storage system. Both are not suitable for a portable system. Neither compressed hydrogen nor metal hydride storage systems can solve the low weight requirement of portable fuel cells. It is quite impractical for a user to refill pressurized hydrogen gas to a compressed gas cylinder (100-200bar) or metal hydride cartridges (10 bar).

There are some alternatives to solve this hydrogen supply issue such as using alcohols. Methanol and ethanol are the most studied alcohols to supply fuel. There are two approaches for using methanol in a fuel cell (see Figure 3.1). First method is the supply of methanol directly to the anode side of the fuel cell. The major drawbacks of this approach are the methanol crossover to the cathode side and catalyst performance degradation at the anode electrode. Another widely studied fuel supply system for a small portable fuel cell system is the on-site reforming of methanol or ethanol. This technology requires highly active catalysts, a challenging reactor design and process control. In addition to these a highly efficient fuel purification unit is required since the products of the reforming process include CO which is a serious poison for the PEM fuel cell catalyst. CO<sub>2</sub> dilutes the fuel and causes recoverable performance loss. Moreover, for a portable system reforming temperature is quite high (>300°C). However, the research of the highly active and robust reforming catalysts working at relatively low temperatures will promote the use of this technology for portable systems. Researches also look for other fuel options like gaseous hydrocarbons and liquid hydrocarbons [23-27] . However, they are not suitable for an onboard or portable fuel conversion [23].

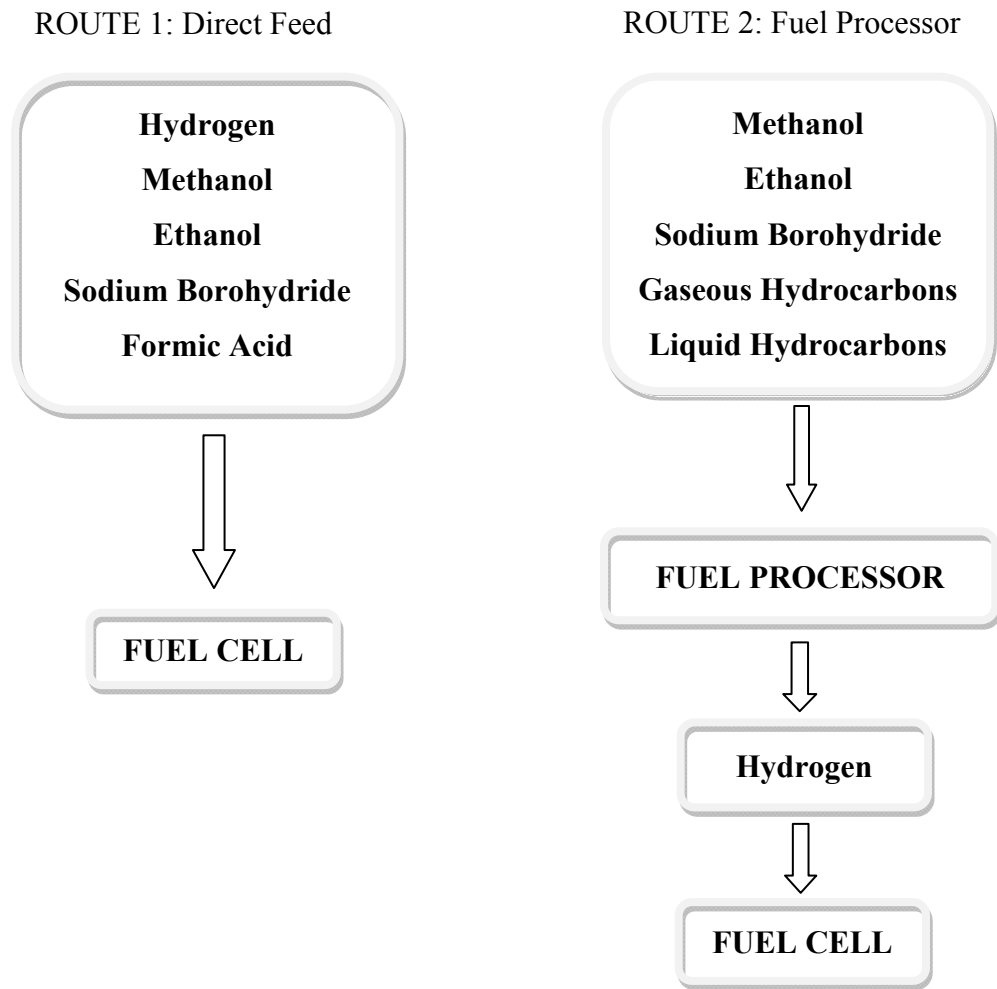


Figure 3.1 Fuel supply options for fuel cells

Another promising fuel supply can be achieved by the catalytic hydration of stable alkaline sodium borohydride ( $\text{NaBH}_4$ ) solution. This fuel supply system has a considerable advantage in weight and volume comparing with the conventional storage systems such as batteries, gasoline, methanol which is shown in Table 3.1. Any type of hydrogen storage has an advantage over the batteries. Gasoline is the lowest weight and volume storage capability. However, it is not possible to use

gasoline as energy storage for a portable fuel cell for the current technology status of the fuel cells. Another good energy storage material is methanol in both mass and volumetric densities. This advantageous status of the methanol encourages the researches for the utilization of methanol as a fuel cell energy storage material.

Table 3.1 Comparison of hydrogen storage systems each with 1 kWh of stored energy (~8h of operation of net 100W generating PEM fuel cell system)

	Total weight (g)	Weight of fuel (g)	Weight of container (g)	Volume (L)
Battery <sup>a</sup>	20460	-	-	8.19
Gasoline <sup>b</sup>	93	076	17	0.10
Methanol <sup>b</sup>	196	169	27	0.21
Aqueous sodium borohydride solution <sup>c</sup>	293	258	35	0.26
Hydrogen, metal hydride <sup>b</sup>	2659	28	2631	1.17
Hydrogen, gas at 250barg <sup>b</sup>	981	28	953	1.65
Hydrogen, gas at 350barg <sup>b</sup>	706	28	678	1.27
Hydrogen, liquid <sup>b</sup>	251	28	223	0.40

<sup>a</sup> calculation is based on commercially available Li-ion battery, GP1865T220

<sup>b</sup> calculation is based on Ballard course material “Introduction to Fuel Cell & Related Technologies”

<sup>c</sup> calculation is based on 28g equivalent of NaBH<sub>4</sub> solution

### 3.1.1 Recent developments in sodium borohydride hydrogen supply for PEMFC systems

A mass of 0.133 kg of  $\text{NaBH}_4$  and 0.125 kg of water with a total mass of 0.258 kg yields 28 g of hydrogen. This amount store 1kWh of energy similar to the storage systems shown in Table 3.1 The main advantage of  $\text{NaBH}_4$  over alcohols is its easy kinetics which includes the existence of highly active catalysts and low reaction temperature and high purity hydrogen production. Amendola et.al [28], Özkar and Zahmakıran [29] showed ruthenium can be used as highly active hydrogen production catalysts, Jeong et.al [30], Kim et.al [31] and Ingersoll et. al [32] investigated the catalytic hydrolysis of  $\text{NaBH}_4$  with non-noble Ni–Co–B catalyst. Platinum on carbon catalysts showed excellent hydrogen generation performances in hydrolysis reaction of  $\text{NaBH}_4$  solution which is a similar catalyst used in PEM fuel cells [33]. The recent developments in  $\text{NaBH}_4$  hydrolysis systems as a  $\text{H}_2$  generation system are summarized in Table 3.2.

Amendola et.al [28] developed a safe, simple, compact process generates high-purity hydrogen gas on demand from base-stabilized, aqueous solutions of sodium borohydride,  $\text{NaBH}_4$ , by using a ruthenium, Ru, catalyst. These  $\text{NaBH}_4$ -based solutions can store up to 7% hydrogen by weight and can generate significant amounts of  $\text{H}_2$  gas under ambient conditions. However, when in contact with Ru catalyst,  $\text{NaBH}_4$  solutions spontaneously hydrolyze to form  $\text{H}_2$  gas and sodium borate, a water-soluble, inert salt. When Ru catalyst is separated from the  $\text{NaBH}_4$  solution,  $\text{H}_2$  generation stops. This  $\text{H}_2$  generator promises to be safer, have quicker response to  $\text{H}_2$  demand, and have a greater  $\text{H}_2$  storage efficiency.

A 10 kW-scale hydrogen generator that generates high purity  $\text{H}_2$  gas from aqueous solutions of  $\text{NaBH}_4$  is developed [34]. The generator is made up of a fuel tank for the  $\text{NaBH}_4$  solution, a pump for the solution, the byproduct ( $\text{NaBO}_2$ ) solution storage

tank, a separator and a hydride reactor. The reactor contained a honeycomb monolith coated with Pt-LiCoO<sub>2</sub> catalyst. The maximum H<sub>2</sub> generation rate is 120 nl/min.

Table 3.2 Summary of the published NaBH<sub>4</sub> hydrolysis catalysts and H<sub>2</sub> generation rates

Catalyst	H <sub>2</sub> generation rate	T °C	Solution composition	Integration to a PEMFC system	Reference
Ru	2.4 L/(min g)	40	7.5%NaBH <sub>4</sub> 1%NaOH	No	[28, 34]
Pt-LiCoO <sub>2</sub>	0.5 L/(min g)	100	25%NaBH <sub>4</sub>	No	[34]
Co-B	1.2 L/(min g)	20	20%NaBH <sub>4</sub> 10%NaOH	No	[30]
Ru nanocluster	53 L/(min g)	40	0.57% NaBH <sub>4</sub> 0%NaOH	No	[29]
Ni-Co-B	2.6 L/(min g)	28	2.7w% NaBH <sub>4</sub> 15%NaOH	No	[32]
Pt/C	29.6 L/(min g)	20	10%NaBH <sub>4</sub> 5%NaOH	No	[33]
Co-B/Ni foam	2.5L/(min g)	80	20%NaBH <sub>4</sub> 1%NaOH	Yes Steady-state	[31]

Jeong et.al. [30] prepared Co-B catalyst for hydrogen generation from an aqueous alkaline NaBH<sub>4</sub>. To design a hydrogen generator, hydrogen generation rate is

measured using the Co-B catalyst as a function of solution temperature, amount of catalyst loading, NaBH<sub>4</sub> concentration, and NaOH (a base-stabilizer) concentration. Compared to Ru catalysts, the low-cost Co-B catalyst exhibited comparable activity for the hydrogen generation reaction.

Özkar and Zahmakıran [29] showed that water-dispersible ruthenium(0) nanocluster highly active catalyst in the hydrolysis of sodium borohydride which can be used as an effective source for producing H<sub>2</sub>. Using ruthenium (0) nanoclusters catalyst provides the lowest activation energy ever found for the hydrolysis of sodium borohydride. Thus, the catalytic hydrolysis sodium borohydride can be performed at ambient temperature and hydrogen gas can be generated at an appreciable rate.

Ingersoll et al. [32] investigated the catalytic hydrolysis of NaBH<sub>4</sub> with a novel, non-noble, catalyst Ni-Co-B that could positively contribute to an enhanced efficiency of hydrogen generation. The hydrogen generation rate of NaBH<sub>4</sub> with a Ni-Co-B-2 catalyst is found to be 2608 ml min<sup>-1</sup> g<sup>-1</sup> catalyst with a highly stable 15 wt% NaOH solution at 28 °C. This value is remarkably high and 11 times faster than the reported rates with an initial NaBH<sub>4</sub> concentration of 0.16 g. The rate of hydrogen generation in the catalysis of alkaline NaBH<sub>4</sub> solution is shown to increase with increase in NaOH concentration and displays a parabolic trend by reaching a maximum value around a concentration of 15 wt% of NaOH and subsequently decreasing with further increase in NaOH concentration. The hydrogen generation rate is almost constant with respect to variation in the NaBH<sub>4</sub> concentration, which is a rare observation with a Ni-Co-B catalyst.

Bai et.al. [33] synthesized Pt/C catalysts which show excellent hydrogen generation performances in hydrolysis reaction of NaBH<sub>4</sub> solution. When 10% NaBH<sub>4</sub>-5% NaOH solution is pumped into with a speed of 10 ml/min, a hydrogen generation system with 100 mg 13.1% Pt/C catalyst has the ability to achieve a maximum hydrogen generation rate of 29.6 l/min/g, and give sustaining H<sub>2</sub> supply for a

PEMFC with an average hydrogen generation rate of 23.0 l/min/g, and achieve approximately 100% hydrogen generation efficiency.

A NaBH<sub>4</sub> hydrogen generator integrated fuel cell system is generated by Kim et.al. [31]. A hydrogen generation system using Co–B/Ni foam from NaBH<sub>4</sub> solution is developed. The system can produce >6 L min<sup>-1</sup> of hydrogen. They integrate this generator to operate a 450W PEMFC stack. The operating conditions are: optimum flow rate of NaBH<sub>4</sub> aqueous solution = 17.5 mL min<sup>-1</sup>; appropriate concentrations of NaBH<sub>4</sub> and NaOH in the feed solution = 20 and 1 wt %, respectively. The system consists of five parts: hydrogen generation, spent fuel retrieval, product cooling, gas-liquid separation, and purification. In addition, a power-conditioning control board is installed to provide system control.

A promising fuel supply can be achieved by the catalytic hydration of stable alkaline sodium borohydride (NaBH<sub>4</sub>) solution. The main advantage of NaBH<sub>4</sub> over alcohols is its easy kinetics which includes the existence of highly active catalysts and low reaction temperature and high purity hydrogen production. This fuel supply system has a considerable advantage in weight and volume comparing with the conventional storage systems. A demand exists for the development of a portable PEM fuel cell system which has a NaBH<sub>4</sub> fuel supply system. Although NaBH<sub>4</sub> is an expensive material to use as a fuel currently, some specific applications such as military power units might be considered independent from its cost. Therefore, this technology can be directly applied to an unmanned air vehicle or soldier power unit to supply thermal cameras, wireless communications etc. The most critical part of such a system is to balance supply and demand of hydrogen for changing electrical load. The unit must not starve hydrogen when a sudden increase in the power demands. The solution to the problem requires synchronous synergetic effects of electronic, chemical and electrical issues. There is a need for an extremely fast response for the changing load demands.

## CHAPTER 4

### EXPERIMENTAL

The methods for the manufacturing of the key components of the PEM fuel cell stack, bipolar plate coating, and performance testing for the developed and manufactured MEAs, single fuel cells or fuel cell stacks are described in this chapter.

#### 4.1 Membrane Electrode Assembly Preparation Technique

##### 4.1.1 Spray gun method

The preparation technique of MEA can affect the performance of a PEM fuel cell seriously. The techniques shown in Figure 4.1 can be applied for MEA preparation. In the first technique, a pneumatic spray gun is used for coating the catalyst to the hydrophobically treated layer of the gas diffusion media. Once a single ultra thin layer is coated, the surface is dried by a hot air gun set at 80 °C or infrared heating lamp. This coating-drying cycle is repeated many times. The catalyst coated gas diffusion layer (GDL) is weighted in order to determine if the desired catalyst load is reached or not. When the desired load is reached for anode and cathode, the catalyst coated GDLs are hot pressed onto the both sides of the Nafion membrane. The second technique involves the use of Teflon sheet as an electrode transfer medium. First, catalyst ink is sprayed as described in Method 1, and the electrode is transferred to Nafion membrane by hot pressing the electrode coated Teflon sheet to the membrane. The third method is the application of spray method directly to the Nafion membrane placed on a heated vacuum table kept at 80 °C.

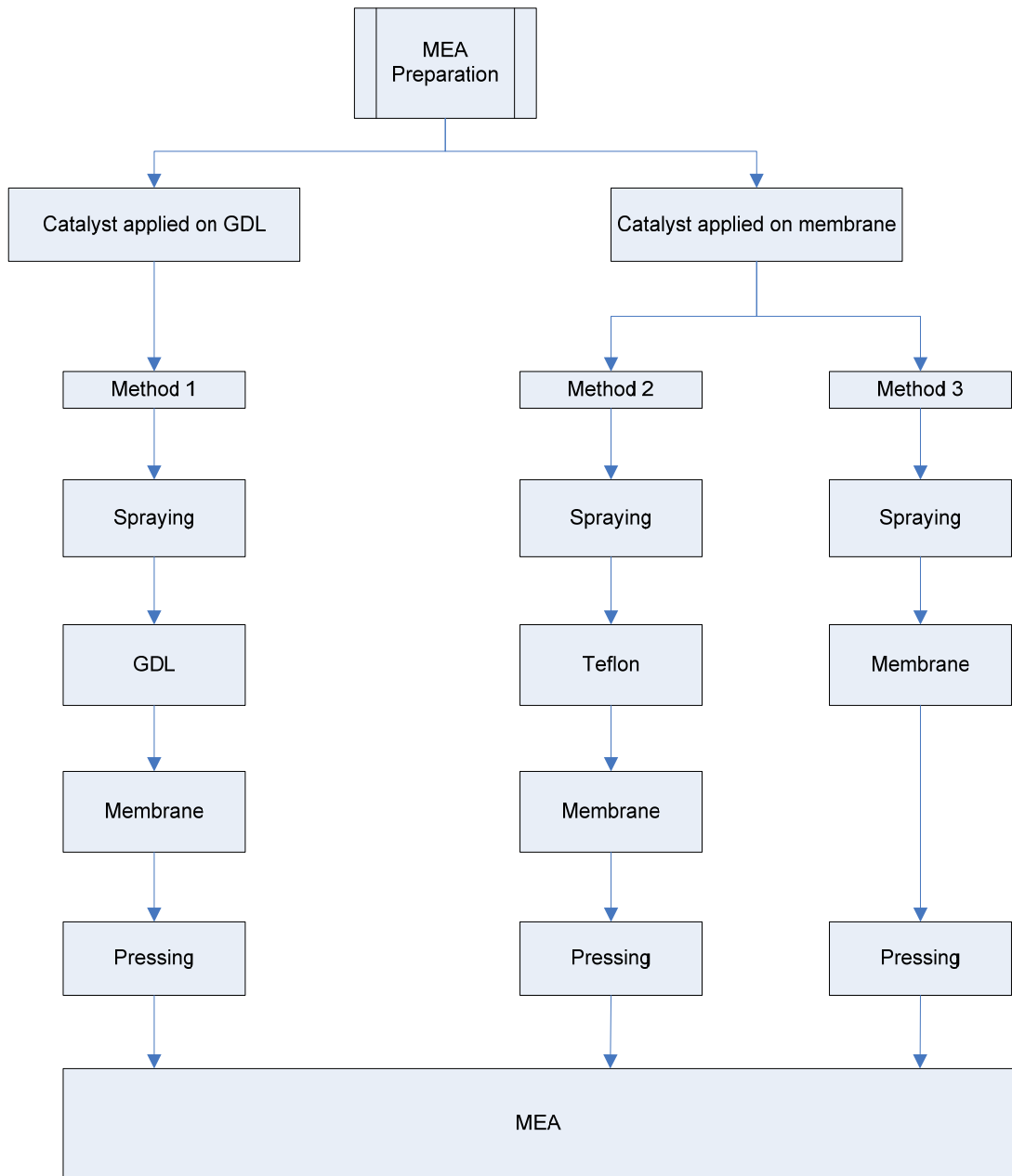


Figure 4.1 MEA Preparation Techniques

The membrane electrode assemblies (MEAs) were prepared by spraying catalyst ink onto the GDLs (GDL 30 BC) from SGL Carbon (Germany) via spray gun. The platinum loading was  $0.4 \text{ mgPt/cm}^2$ , whereas Nafion<sup>®</sup> loading was set to 30wt% dry basis in catalyst ink. The catalyst ink was sprayed until the desired catalyst loading ( $0.4 \text{ mgPt/cm}^2$  for both anode and cathode sides) was achieved. After spraying the catalyst ink onto the GDL a five-layer MEA was prepared by pressing these GDLs onto the membrane at  $130 \text{ }^\circ\text{C}$ ,  $172 \text{ Ncm}^{-2}$  (250psi) for 3 min. Nafion<sup>®</sup> 212 which has a nominal thickness of  $50 \text{ }\mu\text{m}$  was used as the proton exchange membrane [4, 5].

#### 4.1.2 Newly developed MEA preparation procedure

In order to improve the performance and enable consistent quality membrane electrode assemblies a new method has been implemented. Hand operated spray gun method has been improved by integrating computer automated tools. The experience showed that uniform coating of the electrodes cannot be achieved for large electrode areas with hand controlled spraying. Moreover, electrode structure depends on the operator of the sprayer. The new method is also a spraying method but spraying mechanism is different. An ultrasonic nozzle is used for the atomization of the ink. When liquid is added to a resonating nozzle, waves are formed on the atomizing surface. Increasing the power causes the wave peaks to get so high that droplets fall off the tips of the wave. The uniform thin film coating achieved with ultrasonic retains the porosity of the electrode and does not impede the transport of reactants due to flooding of the electrode surface. The nozzle is attached to a computer controlled and programmable XYZ motion device. Therefore, high performance and reproducible electrodes can be produced.

A coating machine (SonoTek, USA) has been purchased and installed (see Figure 4.2). The coating is based on the coating to support which is either membrane or GDL by ultrasonic atomization of the catalyst ink material. Coating process is fully

computer controlled and can be programmed according to the coating area. Catalyst ink flow rate, spray head speed, spray width, stop times between the adjacent coatings can be changed. These parameters are listed in Table 4.1. Newly developed method is called “ultrasonic spray coating method”.

Table 4.1 Ultrasonic machine parameters during electrode coating

Spray head frequency	48 kHz
Catalyst ink flow rate	0.3 ml/min
Spray head speed	20 mm/sec
Spray width	5 mm
Brake time between cycles (to allow drying of the layer)	5 sec

The catalyst ink composition was exactly same as the ink used in spray gun method as reported in previous studies carried out in the METU Fuel Cell Technology Laboratory [4]. It is composed of either 20, 40, 50 or 70 % Pt/C catalyst, 30 wt% Nafion (dry basis) and 1:7 ratio of water, 2-propanol. The prepared catalyst ink is mixed in ultrasonic cleaner at least 15 minutes prior to filling the syringe pump of the coating machine. The number of passes was either 88, 110 or 132 applied to either membrane or GDL to reach the desired catalyst loading. Catalyst loading was verified by gravimetric method.



Figure 4.2 A view of the ultrasonic coating machine

#### 4.1.3 MEAs used for the stacks

Two MEA preparation procedures were followed for the preparation of the MEAs used in the stacks. The first two stacks (Design 1 and Design 2 stacks) were assembled with the MEAs prepared by hand operated spray gun. The third and fourth stack designs (Design 3 and Design 4 stacks) have been assembled with the MEAs prepared with ultrasonic coating machine as developed during the study.

The catalyst ink is composed of 70% Pt/C catalyst, 30 wt% Nafion (dry basis) and 1:7 ratio of water, 2-propanol. The prepared catalyst ink is mixed in ultrasonic

cleaner at least 30 minutes prior to filling the syringe pump of the coating machine and syringe was ultrasonically mixed continuously during entire coating process. The catalyst loading was verified by gravimetric method. The picture of the catalyst coating process onto the GDL is shown in Figure 4.3.

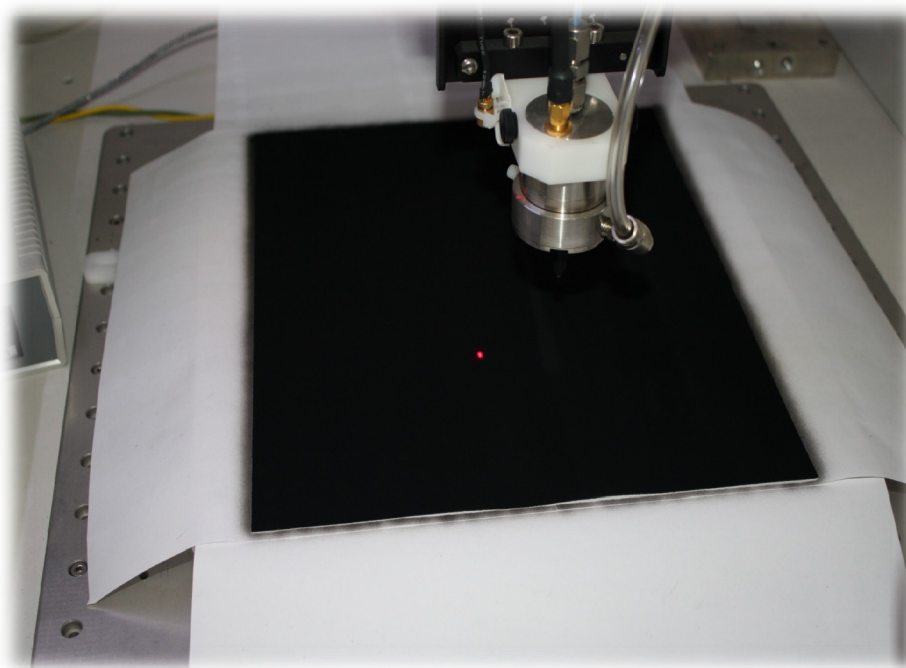


Figure 4.3 The picture of coating machine in action

The gas diffusion electrode (GDE) prepared were cut in 5cm x 4.1cm rectangles and pressed onto the both sides of Nafion 212 ionomer at 130°C temperature and 250psi pressure. Total active area of the MEAs prepared is 492 cm<sup>2</sup>. The picture of the prepared MEAs is shown in Figure 4.4.

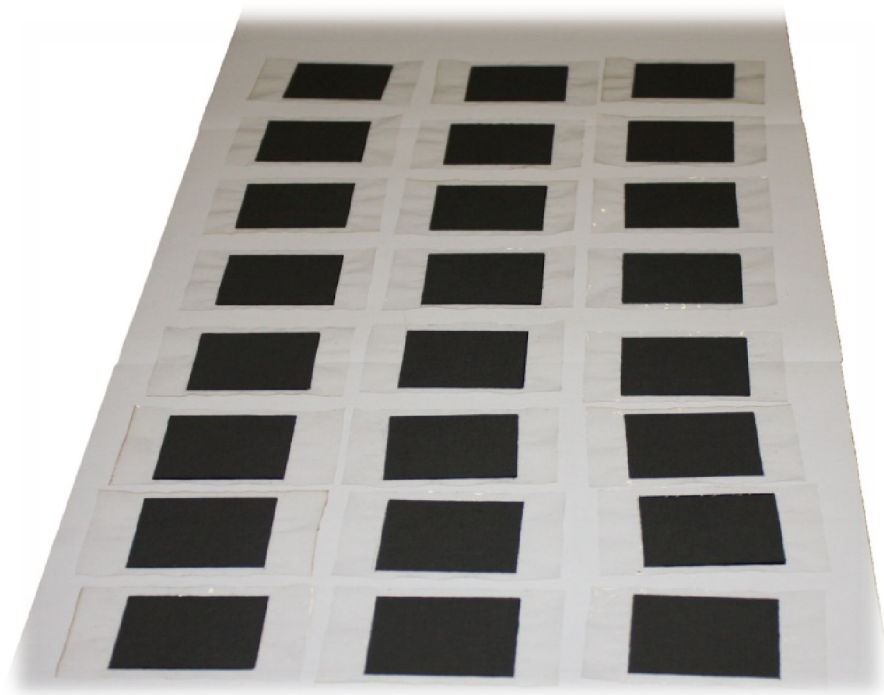


Figure 4.4 The picture of the prepared MEAs of the 100W fuel cell stack

## 4.2 Bipolar Plate Manufacture

The 3-D design is finished in Solidworks software. In order to machine parts, the drawing vectors were exported from the Solidworks in dxf format and imported into ArtCam Pro Computer aided milling (CAM) software for the creation of the toolpaths. The toolpaths generated by the software were saved in a universal machining code file which is called G-Code. Then, this G-code file was loaded to a CNC controller software (KCAM4 CNC Controller, Demo) to machine graphite and aluminum parts. The flow chart of the bipolar plate design and machining is shown in Figure 4.5.

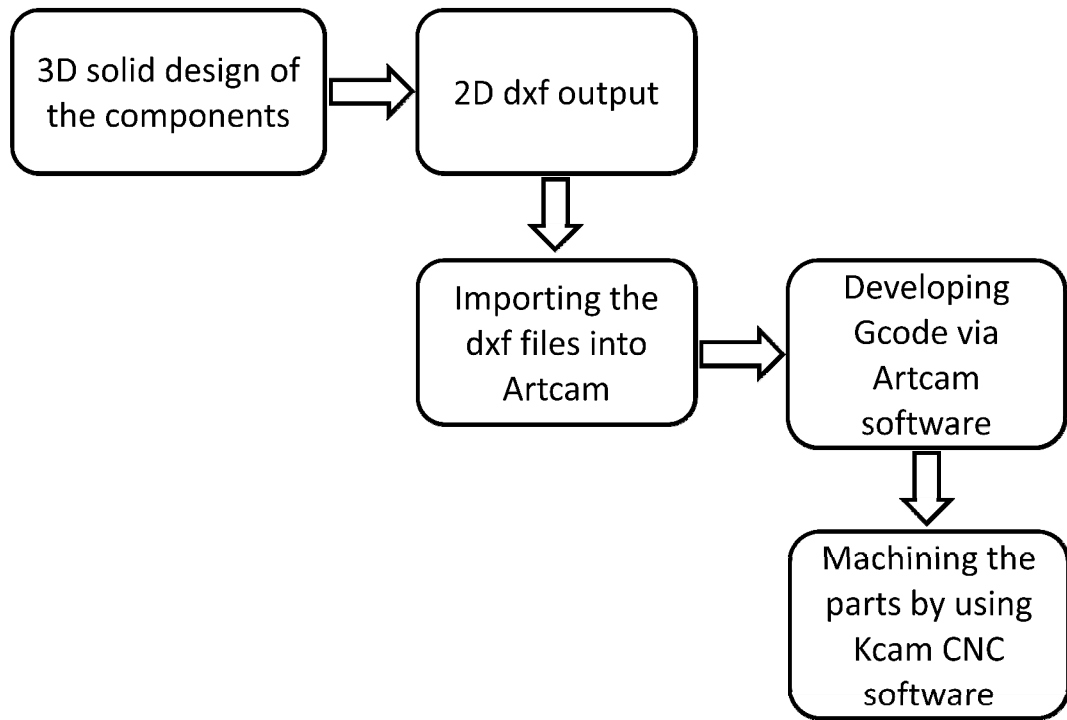


Figure 4.5 The steps for bipolar plate machining

For the preparation of single cells and PEM fuel cell stacks a computer numeric control (CNC) router milling machine illustrated in Figure 4.6 is used (HIZAL CNC, Ankara).

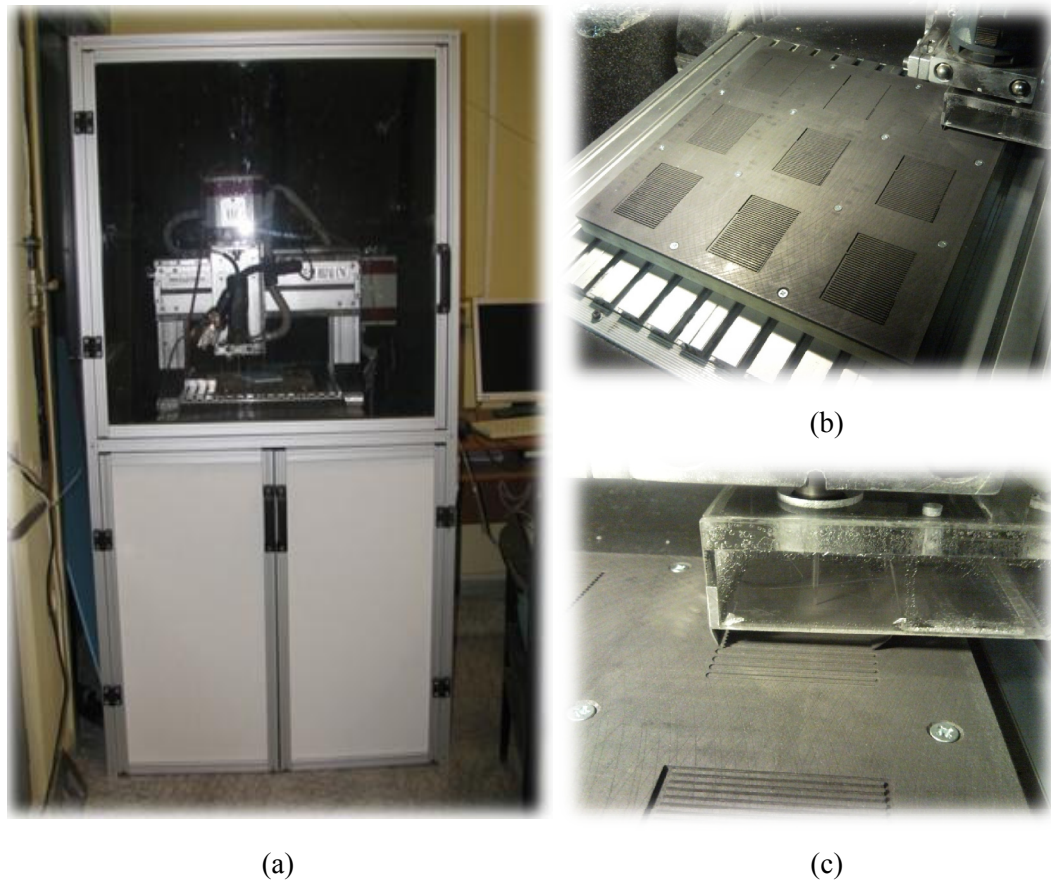


Figure 4.6 The photographs of (a) CNC router machine and (b),(c) bipolar plate machining

### 4.3 Bipolar Plate Coating

The use of metallic bipolar plates has many advantages such as suitability for mass production, high heat and electrical conductivity, and mechanical durability. However, they have a disadvantage that the interface for electron transfer between GDL and flow field loses its electrical conductivity during operation. Coating is required in order to prevent the surface from corrosion. Electrolytic or electro-less coatings such as nickel or gold plating can be applied to the base metal. Another

approach is coating the metal with solder. Other than metal coatings, graphite composite coatings with a suitable binder might also be used.

#### 4.3.1 Electrolytic plating

The bipolar plates of Design 3 are machined by aluminum. The aluminum itself cannot be plated with nickel directly. In order to plate nickel onto aluminum conversion plating is required. This plating is called zincate treatment. The adherence quality of nickel is dependent on the quality and adherence of this zinc layer. Double zincating is also applied in order to increase the adherence of nickel over aluminum [35, 36]. The manufactured bipolar plates were plated with preventive materials such as zinc and nickel in order to conduct electrons on gas diffusion layer. The work is performed by metal plating professional. Nickel coating was performed as described in Figure 4.7. The picture of the back and front side of the nickel plated bipolar plate is shown in Figure 4.8

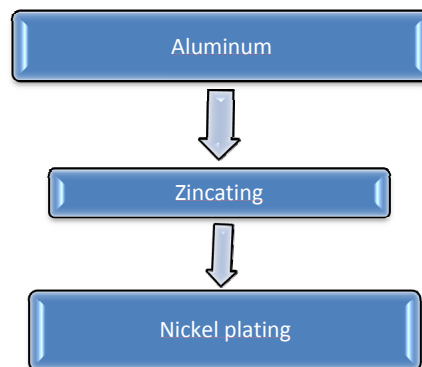


Figure 4.7 Process for Ni plating on aluminum bipolar plate

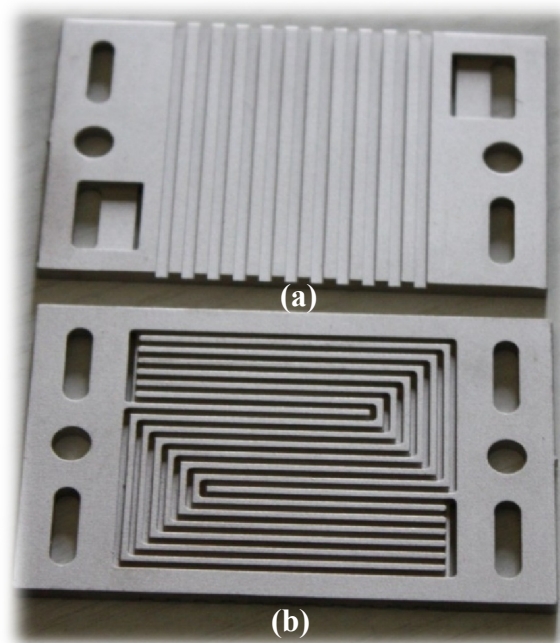


Figure 4.8 Picture of Ni plated aluminum bipolar plate  
( a) air cooling side, (b) flow channels

#### 4.3.2 Coating with soldering

In order to obtain a corrosion resistant coating on the flow field, a Sn-Ti-Ag alloy based solder is used to form a thin film layer. The alloy is obtained in the wire form. A single test cell having  $5\text{cm}^2$  active area was produced by machining of aluminum. The part was heated to  $250^\circ\text{C}$  and the solder was applied with a steel brush and spatula. The plate was cooled down to room temperature. Then, the surface of the active area was grounded with 2000 grits sandpaper to clean the surface of the alloy from the formed oxides.

### 4.3.3 Coating with conductive composite paint

Conductive paints might be used for the protection of the conductive interface of the bipolar plates. A conductive interface has to be highly conductive and chemically durable in the fuel cell environment. Composite bipolar plates are produced with blends of graphite and/or carbon black and thermoplastics such as poly vinylidene fluoride (PDVF), polypropylene, polyethylene and thermoplastics such as epoxy resin, phenolic resin, furan resin and vinyl ester [2]. In order to prepare a conductive coating paint 0.425 g natural graphite flake powder (-325 mesh) (graphitstore, USA) and 0.075 g polyvinylidene fluoride (PVDF) (Sigma Aldrich) mixed in 5ml N,N-dimethylacetamide ( $\text{CH}_3\text{C}(\text{O})\text{N}(\text{CH}_3)_2$  DMAc) (Merck). The ink observed was sprayed onto the aluminum plate having 5 cm<sup>2</sup> active area at 120°C. The coated 5cm<sup>2</sup> active area fuel cell plate is shown in Figure 4.9.

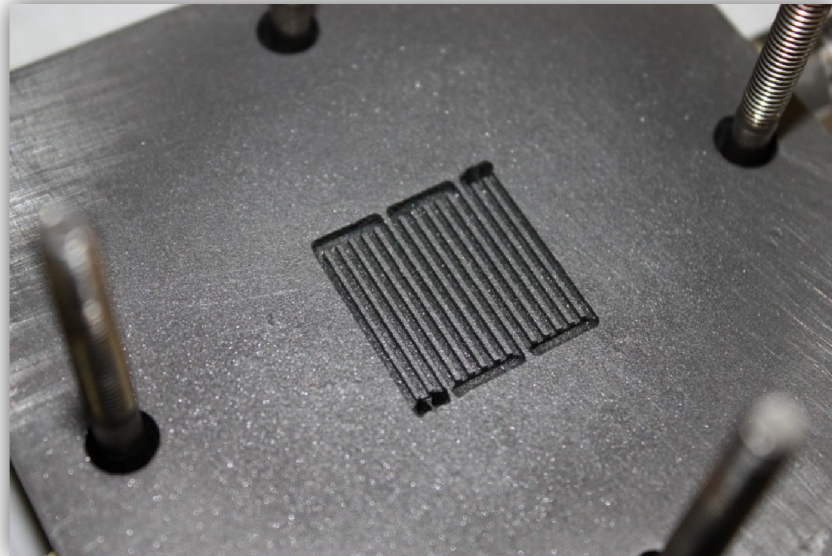


Figure 4.9 Graphite-PVDF composite painted aluminum fuel cell test plate having 5cm<sup>2</sup> active area

#### 4.4 Electrochemical Impedance (EIS) Tests

The impedance characteristics of the the coatings are measured with an electrochemical impedance analyzer (Gamry, PCI 750 potentiostat with EIS300 system, USA). The experimental setup for the electrochemical impedance spectrometry measurements is shown in Figure 4.10. The test was performed from 0.01 Hz to 60 kHz. The silicone gasket used in the fuel cell tests is used in order to achieve the same compression obtained during the fuel cell tests and prevent plates from electrical short circuit.

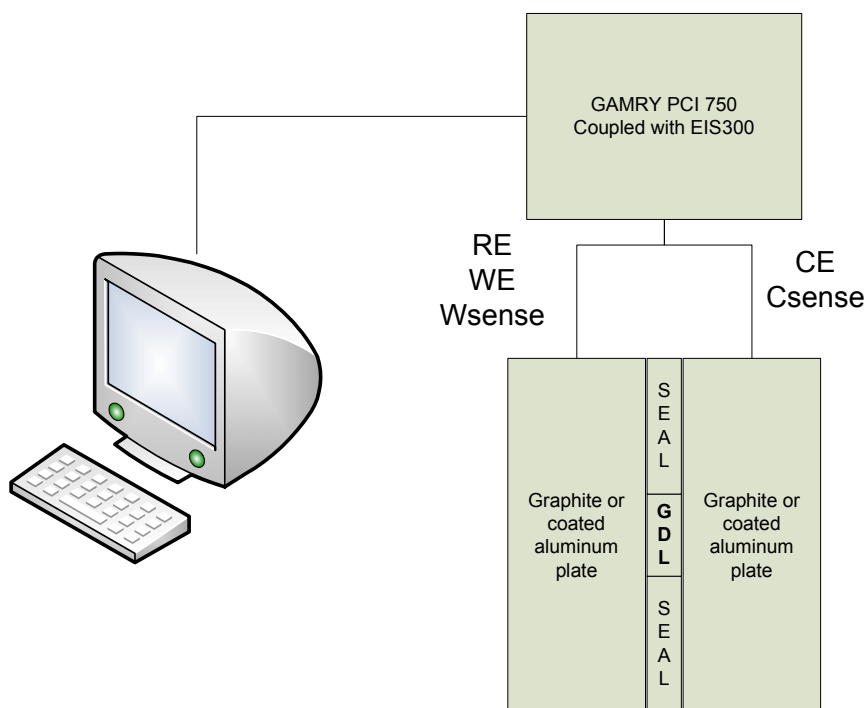


Figure 4.10 The experimental setup for the electrochemical impedance spectrometry measurements

#### 4.5 Test Station and Performance Tests

There is not a consensus about fuel cell testing although many researchers have been carried out more than twenty years. It is well known that the operating conditions affect the performance of a fuel cell. In addition to this, it was understood that testing procedures and sequence can affect the results obtained from a fuel cell. In the recent years US Fuel Cell Council (USFCC) was published a single cell test protocol in order to standardize a reproducible single test results [37]. In this test, after some safety checks, a cell break-in and a polarization curve procedures are applied.

PEM fuel cells are tested in the devices called “Fuel Cell Test Station”. A PEM fuel cell performance is a strong function of fuel cell temperature, reactant flow rates, reactant relative humidity, and fuel cell pressure. Therefore, these parameters have to be controlled. For that purpose some researchers prefer to build their own test systems which generally do not allow unattended automatic operation. The commercially available reliable test systems are Fideris (Tessol), Henatech, Fuelcon, Teledyne, Greenlight. It is not possible to purchase a test station and use it for a complete power range of fuel cells. The selection of the mass flow controllers (MFC) defines the upper limit of the controllable gas flow rate. When a MFC is selected, it is not possible to control the flow rates lower than 2% of the full scale.

There are two humidification designs in the test station market. The easiest humidifier design is achieved by passing reactant gasses through bubbler tank. The thermodynamic equilibrium is achieved in the tank and the humidification level can be controlled. However, this design has a very high response time. It is not possible to change the humidity level dynamically. In a more complicated humidifier design, the necessary water to produce desired relative humidity is calculated and injected to an evaporation chamber by precise metering pumps. This design allows dynamic relative humidity change with 3-5 second response time. The drawback of this design

is that a complex script is required to calculate and set the water injection rate for the actual flow rate, temperature, and pressure of the stream.

Two fuel cell test station is used throughout the study. First of the test stations is a system built in house and capable of single cells and small stacks up to 120W. The second test station is a commercial equipment (Fideris, USA) which is capable of testing large area single cells and stacks up to 2kW of electrical output.

#### 4.5.1 Procedure for leakage test

Prior to the beginning of a test, a short circuit test is made by measuring the resistance of the assembled cell via multimeter. Then an internal and external leak tests are performed. Nitrogen gas is used for leak test. First, anode and cathode are filled with 3 psi nitrogen gas. The pressure of the cell is adjusted by using the backpressure regulators installed on the test station. Inlet is isolated and the pressure is gauged for 5 minutes. Then, internal leak test is performed. Cathode side is pressurized to 3 psi with nitrogen gas. The inlet of the anode is isolated and the exhaust of the anode connected to a beaker filled with water. The test is approved if there is no bubble observed at the beaker for 5 minutes.

#### 4.5.2 Procedure for operation

The temperature of the cell is set at 70°C which is controlled via a resistive pad heater connected to PID temperature controller (Delta DTA Series, Taiwan). The anode and cathode are purged with 100% RH humidified nitrogen gas until the cell reaches the operating temperature. Then hydrogen and air are supplied to the anode and cathode respectively. Then the cell put in the constant 0.55V for break-in. After the cell reached a constant current (within %5 of the previous current data measured in hourly basis), the potentiostatic polarization data is taken. The polarization curves

from OCV conditions to 0.35 and 0.35 V to OCV conditions are taken. This procedure is repeated until no more performance increase was observed. At least three stable and repeatable polarization curves are reported as the performance of the tested cell at given temperature, humidity, and flow conditions.

#### 4.5.3 Homemade single cell test station

The single cell tests are performed in a homemade fuel cell test station which is shown in Figure 4.11, Figure 4.12 and Figure 4.13. It is used for testing PEM fuel cell components developed by the METU research team such as catalyst and composite and alternative membranes [4, 5, 13, 38-40]. The test station is capable of testing single PEM fuel cells and small PEM fuel cell stacks up to 120W with one oxidation gas and up to three gas mixtures as a fuel. In order to access the required power, reactant gas flow rates were adjusted with mass flow controllers (Aalborg GFC 171). The flow rates for the anode and cathode were adjusted as having 1.2 and 2.5 stoichiometric ratio, respectively. Prior to entering the fuel cell stack, these gases were humidified to 100% relative humidity (RH) by passing them through the water columns contained in stainless steel cylinders and heated with resistance heaters. The 316L stainless steel gas lines were heated to prevent the condensation of the water in the lines. The temperature in the humidifiers, the gas lines and the fuel cell were controlled by PID temperature controllers. The purge gases left through the water columns placed at the exit of the fuel cell. The load on the stack was adjusted by a 400 W electronic load (Dynaload RBL488, TDI) that was controlled by means of the fuel cell testing software (FCPower). The same software was also used for data logging. Voltages for each cell was monitored and logged by a cell voltage monitor (CVM) system (Yokogawa MX100).

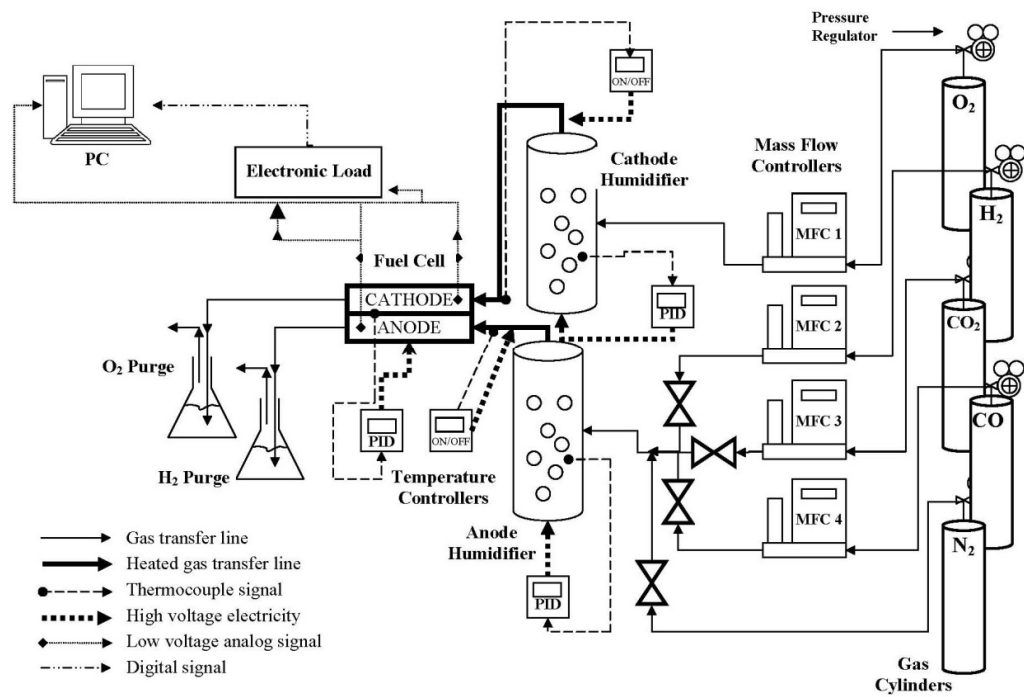


Figure 4.11. Schematic view of the homemade test station which is used for single cell testing

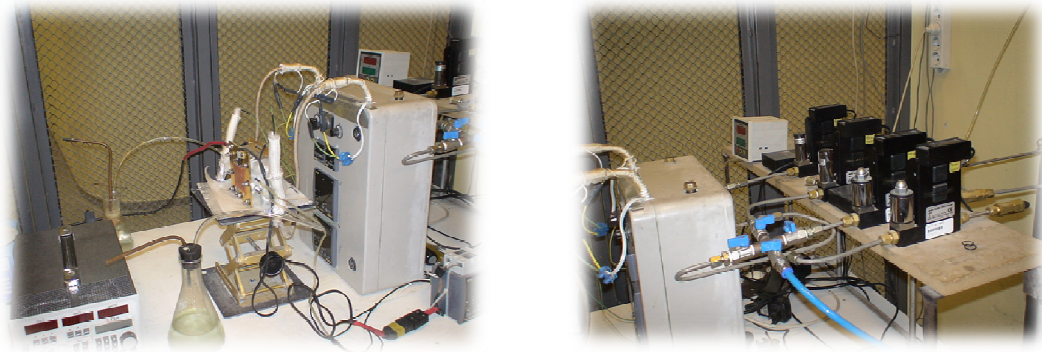


Figure 4.12. Photograph of the homemade test station which is used for single cell testing



Figure 4.13. Photograph of the homemade test station during stack testing

#### 4.5.4 Commercial 2kW PEM fuel cell test station

A commercial test station is used for testing and understanding of performance and durability of 100W-2 kW PEM fuel cells (Fideris, USA). It is fully automatic and controlled with computer. It can be programmed via Visual Basic Script language and built in playback programming. A script was written for the adjustment of the stoichiometric flow rates of the reactants. The script sets the mass flow controllers for the required stoichiometric gas flows according to the current dissipated at the electronic load. A minimum gas flow flow can be set then a minimum gas flow always exist even the load is off. The flow rates for the anode and cathode are adjusted as having 1.2 and 2.5 stoichiometric ratio, respectively. Prior to entering the fuel cell stack, these gases are humidified to 100% relative humidity (RH) by passing them through reactant gas humidifiers. The heated gas transfer lines are used to

prevent the condensation of the water in the lines. The gas feed temperatures are measured (anode-cathode in). The load on the stack is adjusted by an electronic load (Dynaload RBL488, TDI) that is controlled by means of the fuel cell testing software (FCPower). The same software is also used for control of the test station and data logging.



Figure 4.14 Photograph of the commercial test station which is used for stack testing

## CHAPTER 5

### PEM FUEL CELL STACK DESIGN

A PEM fuel cell is an electrochemical electrical energy producing device having a polymer proton conducting membrane between anode and cathode. Hydrogen fed to the anode is divided into two protons and two electrons. The cathode is fed with oxygen which usually comes from air although there might be applications which uses pure oxygen. The oxygen molecule is separated into its  $O^{2+}$  ions. While the electrons produced in the anode side, they are not allowed to pass through the cathode side, the charge formed has a potential of 1.229V between the anode and cathode at ideal (theoretical) conditions. The schematic of a PEM fuel cell at ideal conditions is illustrated in Figure 5.1. The theoretical cell potential cannot be observed because of the electron and hydrogen leaks to the cathode through the membrane.

A typical open circuit voltage (OCV) can be observed from a PEM fuel cell is 0.9 to 1V. When an external load is connected to the cell, the circuit is closed and the electrons produced at the anode flows through the cathode. A typical operating potential of a PEM fuel cell is 0.5 to 0.7V and the corresponding current observed might be 1 to 0.5A, respectively. The reaction occurs in the PEM fuel cell is exothermic. Then a cooling system is essential for proper operation of a PEM fuel cell stack. The schematic view of a single PEM fuel cell operating at the rated power is shown in Figure 5.2.

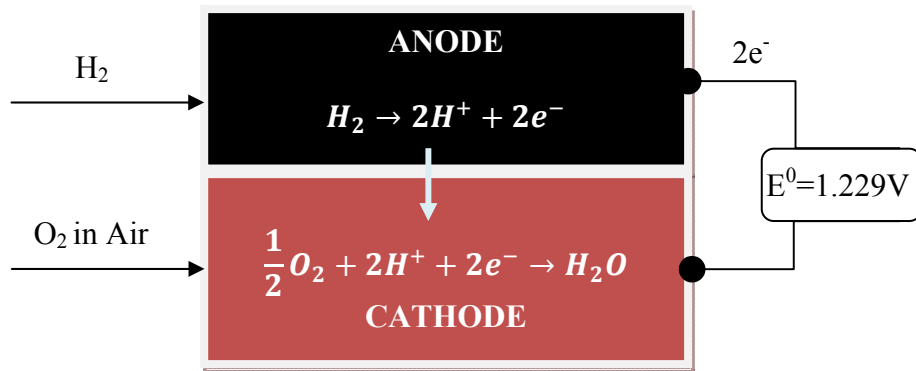


Figure 5.1 The schematic view and reactions of a single PEM fuel cell at ideal conditions

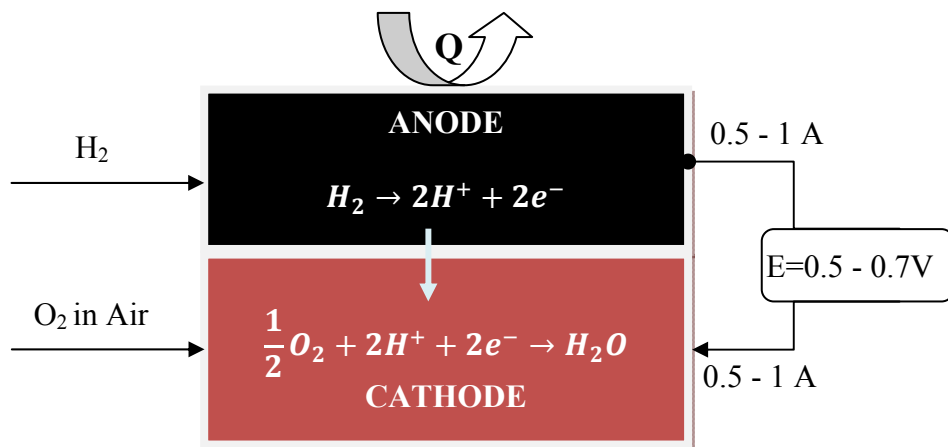


Figure 5.2 The schematic view and reactions of a single PEM fuel cell at maximum load operating conditions

## 5.1 Conceptual Design

A single cell produce electricity at 0.5-0.7V on maximum rated power load conditions. In order to produce electricity useful for many applications, many cells must be connected in series as illustrated in Figure 5.3 to form a fuel cell stack. Bipolar plates are the physical backbone of a fuel cell stack. They also conduct the electrons produced by the reaction, distribute the reactants on the active area of the MEA and exchanges heat generated by the reaction with a suitable cooling medium such as air or water.

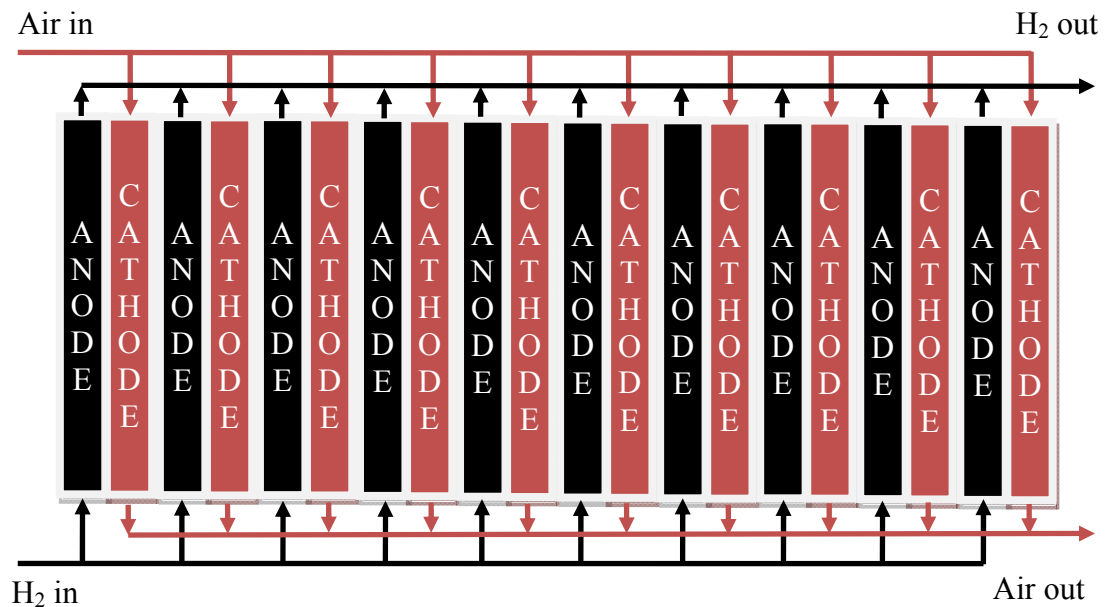


Figure 5.3 The schematic view of a PEM fuel cell stack formation and gas feeds and exhausts

### 5.1.1 Design basis

Stack development is one of the important parts of this study. The starting point of the development of a fuel cell stack is to reveal the design basis of the stack required. The design basis of the stack developed in this study is summarized in Table 5.1. The voltage of the stack at the rated power was selected as 12V since the majority of the portable applications require 12 V. 100W is a sufficient power necessary for many portable applications from various military systems to portable consumer electronics. Due to the fact that the system itself consumes power in order to keep the system in operation, the stack must be designed delivering more power than the net output power. This power consumed is called parasitic losses and it includes the power needed for pumps, compressors, valves, sensors and control system. The current density at the target cell potential of 0.6V is 500mA/cm<sup>2</sup>. This value is the actual current density value that can be observed in stable with air supplied to cathode although more than twice current density can be observed when pure oxygen fed to the cathode. Hydrogen stoichiometric ratio, which is defined as actual feed rate divided by theoretical feed rate, is selected as 1.01 since anode operation mode is selected as dead-end. The air is fed with 2.5 stoichiometric ratio which is a conventional value for an air cathode. There are two options for a cooling system of a PEM fuel cell. Although liquid cooling allows higher amount of heat removal, an air coolant is sufficient and easier for a portable small stack. Although it is possible to select 50 °C to 80°C operating temperature, as a starting calculation basis, 60°C target operation temperature was selected.

Table 5.1 PEM Fuel Cell Stack Design Basis

Potential	12V
Nominal electrical power	100Watt
Parasitic losses	17 W
Current density at 0.6V	500 mA/cm <sup>2</sup>
Stoichiometric ratio of hydrogen	1.01
Stoichiometric ratio of oxygen (supplied as air)	2.5
Cooling	Air
Operating temperature	60°C
Anode humidification	None
Cathode humidification	100% RH
Air supply temperature	25°C
Air and hydrogen exhaust temperature	60°C

### 5.1.2 Design strategy

Design strategy of a PEM fuel cell stack is given below;

- i. Determine the number of cells according to the design potential and target efficiency at nominal power
- ii. Determine active area according to the current density at nominal power
- iii. Estimate the hydrogen consumption from the current
- iv. Estimate the air consumption and water generation from the mass balance equations
- v. Estimate heat dissipation from energy balance
- vi. Select bipolar plates and estimate pressure drop through flow channels
- vii. Estimate cooling air flow rate by heat transfer relations

The sample calculation for 117W stack including mass and energy balance, pressure drop, and heat transfer (cooling) calculations is supplied as a Mathcad worksheet in Appendix 1. The assumptions considered during calculations are as follows:

- i. Steady-state conditions retains
- ii. Stack is operated at a maximum electrical power of 117W
- iii. The ambient temperature is 25 °C
- iv. The fuel cell stack is operating at 60 °C isothermal conditions
- v. Air is fed to the system at 100% relative humidity (RH)
- vi. Hydrogen is pure and it is fed to anode completely dry
- vii. 1% of hydrogen is purged from the anode outlet
- viii. Negligible hydrogen crossover occurs from the anode to the cathode

### 5.1.3 The mass balance for fuel cell

The overall mass balance for a PEM fuel cell at steady state is given in Equation 5.1;

$$\sum (\dot{m}_i)_{in} = \sum (\dot{m}_i)_{out} \quad (5.1)$$

where i represents H<sub>2</sub>, O<sub>2</sub>, N<sub>2</sub>, H<sub>2</sub>O<sub>(g)</sub>, and H<sub>2</sub>O<sub>(l)</sub> for a fuel cell operating with pure hydrogen fuel, and air

The inlet flow rates of H<sub>2</sub>, Air, O<sub>2</sub>, N<sub>2</sub> can be calculated by Equation 5.2 to 5.5, respectively.

$$\dot{m}_{H_2,in} = S_{H_2} \cdot \frac{M_{H_2}}{2F} \cdot I \cdot n_{cell} \quad (5.2)$$

$$\dot{m}_{Air,in} = S_{O_2} \cdot \frac{M_{Air}}{4F} \cdot I \cdot n_{cell} \quad (5.3)$$

$$\dot{m}_{O_2,in} = S_{O_2} \cdot \frac{M_{O_2}}{4F} \cdot I \cdot n_{cell} \quad (5.4)$$

$$\dot{m}_{N_2,in} = \dot{m}_{N_2,out} = S_{O_2} \cdot \frac{M_{N_2}}{4F} \cdot \frac{1 - r_{O_2,in}}{r_{O_2,in}} \cdot I \cdot n_{cell} \quad (5.5)$$

where  $S_{H_2}$  and  $S_{O_2}$  are the stoichiometric ratios which determines the excess amount of feed for hydrogen and oxygen, respectively,  $r_{O_2,in}$  is the oxygen mole fraction in the air and  $F$  is Faraday constant which is 96485 coulombs.

The inlet mass flow rates of the water in  $H_2$  feed and air feed are calculated by Equation 5.6 and 5.7.

$$\dot{m}_{H_2O,in,H_2,in} = S_{H_2} \cdot \frac{M_{H_2O}}{2F} \cdot \frac{\varphi_{an} P_{(T_{an,in})}^{vap}}{P_{an} - \varphi_{an} P_{(T_{an,in})}^{vap}} \cdot I \cdot n_{cell} \quad (5.6)$$

$$\dot{m}_{H_2O,in,Air,in} = \frac{S_{O_2}}{r_{O_2}} \cdot \frac{M_{H_2O}}{4F} \cdot \frac{\varphi_{ca} P_{(T_{ca,in})}^{vap}}{P_{ca} - \varphi_{ca} P_{(T_{ca,in})}^{vap}} \cdot I \cdot n_{cell} \quad (5.7)$$

where  $\varphi_{an}$  and  $\varphi_{ca}$  are the relative humidity of anode and cathode feed streams,  $P_{(T_{an,in})}^{vap}$  and  $P_{(T_{ca,in})}^{vap}$  are vapor pressure of water at the anode and cathode inlet stream temperatures, and  $P_{an}$  and  $P_{ca}$  are the total pressure of anode and, respectively.

The outlet flow rates of H<sub>2</sub>, Air, O<sub>2</sub>, N<sub>2</sub> can be calculated by Equation 5.8 to 5.11, respectively.

$$\dot{m}_{H_2_{out}} = (S_{H_2} - 1) \cdot \frac{M_{H_2}}{2F} \cdot I \cdot n_{cell} \quad (5.8)$$

$$\dot{m}_{Air_{out}} = \dot{m}_{O_2_{out}} + \dot{m}_{N_2_{in}} \quad (5.9)$$

$$\dot{m}_{O_2_{out}} = (S_{O_2} - 1) \cdot \frac{M_{O_2}}{4F} \cdot I \cdot n_{cell} \quad (5.10)$$

$$\dot{m}_{N_2_{out}} = \dot{m}_{N_2_{in}} = S_{O_2} \cdot \frac{M_{N_2}}{4F} \cdot \frac{1 - r_{O_2,in}}{r_{O_2,in}} \cdot I \cdot n_{cell} \quad (5.11)$$

#### 5.1.4 The energy balance

The energy balance for a PEM fuel cell operating at steady state can be described as illustrated in Equation 5.12;

$$\sum (H_i)_{in} = W_{el} + \sum (H_i)_{out} + Q \quad (5.12)$$

where  $(H_i)_{in}$  is the enthalpy of component “i” at the inlet stream,  $(H_i)_{out}$  is the enthalpy of component “i” at the outlet stream,  $W_{el}$  is the electrical work or power produced, and Q is the total heat dissipated.

#### 5.1.5 The results of the mass and energy balance

There are four streams that enter and leave the PEM fuel cell stack as given in Figure 5.4. The results of the mass balance calculations based on the 117.6W net electrical power delivering PEM fuel stack are shown in Table 5.2 and the enthalpies of the streams are given in Table 5.3.

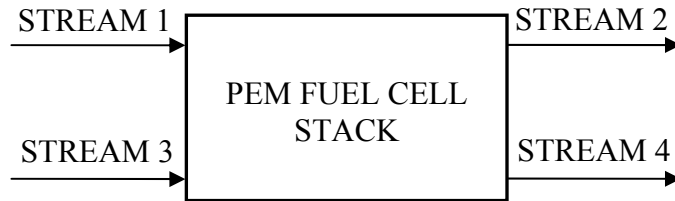


Figure 5.4 Streams that enter and leave the PEM fuel cell stack

Table 5.2 Mass balance table for 117W PEM fuel cell stack

<b>Stream</b> <b>Component</b>	<b>Stream 1</b> <b>Hydrogen Feed</b> <b>(g/h)</b>	<b>Stream 2</b> <b>Hydrogen Out</b> <b>(g/h)</b>	<b>Stream 3</b> <b>Air Feed</b> <b>(g/h)</b>	<b>Stream 4</b> <b>Air Out</b> <b>(g/h)</b>
<b>H<sub>2</sub></b>	7.4	0.074	-	-
<b>O<sub>2</sub></b>	-	-	146	88
<b>N<sub>2</sub></b>	-	-	483	483
<b>H<sub>2</sub>O<sub>(v)</sub></b>	-	-	28	54
<b>H<sub>2</sub>O<sub>(l)</sub></b>	-	-	-	39
<b>Total (g/h)</b>	7.4	0.074	657	664

Table 5.3 Enthalpies of the streams for 117W PEM fuel cell stack

<b>Stream</b> <b>Component</b>	<b>Stream 1</b> <b>Hydrogen Feed</b> <b>Enthalpy (W)</b>	<b>Stream 2</b> <b>Hydrogen Out</b> <b>Enthalpy (W)</b>	<b>Stream 3</b> <b>Air Feed</b> <b>Enthalpy (W)</b>	<b>Stream 4</b> <b>Air Out</b> <b>Enthalpy (W)</b>
<b>H<sub>2</sub></b>	293.23	2.91	-	-
<b>O<sub>2</sub></b>	-	-	1.3	0.78
<b>N<sub>2</sub></b>	-	-	4.89	4.89
<b>H<sub>2</sub>O<sub>(v)</sub></b>	-	-	1.08	0.99
<b>H<sub>2</sub>O<sub>(l)</sub></b>	-	-	-	2.88
<b>Total (W)</b>	293.23	2.91	7.27	9.54
<b>T (°C)</b>	25	60	25	60
<b>Phase</b>	G	G	G	G/L

Rearranging Equation 5.12, Equation 5.13 is obtained. The enthalpies of the streams and the net electrical power are inserted into Equation 5.13. the amount heat dissipation of the system is calculated as 171.45W.

$$Q = \sum (H_i)_{in} - \sum (H_i)_{out} - W_{el} \quad (5.13)$$

$$Q = (293.23W + 7.27W) - (2.91W + 9.54W) - 117.6W$$

$$Q = 170.45 \text{ W}$$

It was specified in the stack design basis that air will be used as a coolant. The calculations for the cooling were performed considering the natural convection and radiation losses from the side and top walls of the stack. The additional heat is removed by forced convection of the ambient air with blower fans. Table 5.4

indicates the results of cooling calculations with respect to ambient conditions when the operating temperature of the fuel cell is kept at 60°C and operating at maximum power.

Table 5.4 Cooling duty with respect to varying ambient temperature (Top = 60 °C)

T <sub>ambient</sub> (°C)	Q <sub>gen.</sub> (P <sub>max</sub> =117.6W) (W)	Q <sub>nat. conv.</sub> (W)	Q <sub>rad.</sub> (W)	Q <sub>total loss.</sub> (W)	Q <sub>cooling</sub> (W)	V <sub>cooling air</sub> (m <sup>3</sup> /s)	V <sub>cooling air</sub> (ft <sup>3</sup> /min)
0	170.45	9.71	5.38	15.09	155.36	2.61x10 <sup>-3</sup>	5.38
10		7.70	4.69	12.39	158.06	3.81x10 <sup>-3</sup>	7.85
20		5.80	3.93	9.72	160.73	5.94x10 <sup>-3</sup>	12.25
30		4.03	3.08	7.11	163.34	0.01	21.16
40		2.41	2.15	4.57	165.88	0.02	43.65
45		1.68	1.65	3.33	167.12	0.03	70.77

Changing fuel cell power changes the heat duty. Table 5.5 shows the change of cooling duty with changing fuel cell operating power at 0°C ambient conditions in which temperature the natural convection and radiation losses are highest. Calculations revealed that if the stack operates at 11W of electrical power which is about the parasitic power, the stack will reach 60°C at steady state. When the electrical power produced by the stack is increased to 25 W, 21W of cooling duty is required.

Table 5.5 Duty with respect to operating power at 0°C ambient temperature

Power <sub>FC</sub> (W)	Q <sub>gen.</sub> (W)	Q <sub>nat. conv.</sub> (W)	Q <sub>rad.</sub> (W)	Q <sub>total loss.</sub> (W)	Q <sub>cooling</sub> (W)	V <sub>cooling air</sub> (m <sup>3</sup> /s)	V <sub>cooling air</sub> (ft <sup>3</sup> /min)
11	15.94	9.71	5.37	15.09	0.9 (~ 0)	0	0
25	36	9.71	5.37	15.09	21.14	6.58*10 <sup>-6</sup>	0.014

The heat transfer calculation results are summarized in Figure 5.5 and Figure 5.6. The heat dissipation and the amount heat to be removed by cooling air are calculated from 10°C to 40°C. When the ambient temperature is 10°C, the stack loses about 12.5W of heat by natural convection and radiation from the sides. When the ambient temperature is 40°C, the naturally transferred heat to the environment is only about 4.5W. Therefore, 158W to 166W of heat has to be removed by the forced convection of cooling air passing through the cooling channels of the stack.

The cooling air requirement is also calculated for different ambient temperatures. About 13.7 m<sup>3</sup>/h (5.38 CFM) air flow is required to keep the stack at the operating temperature of 60°C. When the ambient temperature is 40°C, the cooling air flow requirement increases to 72m<sup>3</sup>/h (43.6 CFM). The cooling fan must be selected as capable of delivering 45 CFM in order to keep the system at 60°C for the operation during hot summer days up to 40°C.

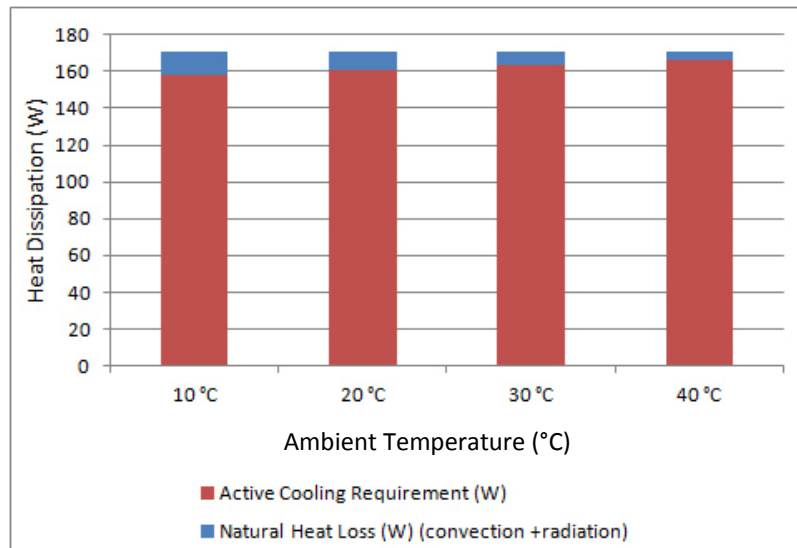


Figure 5.5 Heat dissipation of 117W net electrical power PEM fuel cell stack

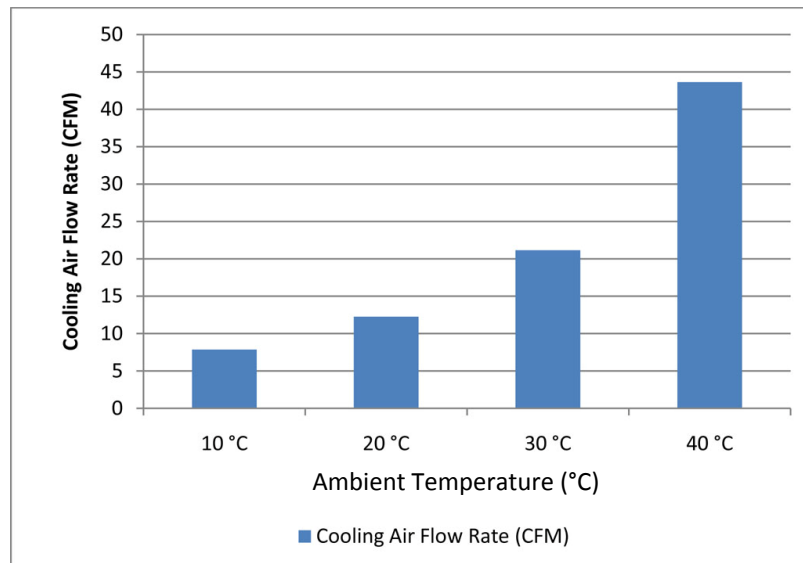


Figure 5.6 Cooling air requirement for 117W net electrical power PEM fuel cell stack at varying ambient temperature

The calculation presented is only for the fuel cell operating at the highest power at steady state. This is necessary because the selection of the air supply compressor, the cooling medium, and NaBH<sub>4</sub> circulation pump or blower fan must be selected according to the maximum conditions. A cooling fan must be provided that can manage to cool the stack. The Mathcad worksheet given in Appendix 1 can be easily adapted to any operating power of the present design's mass and energy balance and cooling duties. This worksheet is also a valuable tool for the future lower or higher power stacks. The effects of the ambient temperature, operating temperature, pressure, humidity of air and/or hydrogen stoichiometry, operating power, and design potential can be calculated.

The design assumes anode operates at dead-end mode in which mode, hydrogen is kept at a 3-5 psig pressure at the anode and flow is prohibited via a solenoid valve. When the potential of the last cell drops below 0.4V due to the decrease of hydrogen concentration, the solenoid valve is opened and small amount of hydrogen is allowed to exhaust. This operation mode is not suitable for humidified hydrogen stream.

## **5.2 Channel and Manifold Design**

Bipolar plates are used for distribution of reactants and forming the backbone of the fuel cell. It must be electrically conductive, chemically stable and light weight. Its mechanical design is also important since it affects the distribution of the reactants throughout the cells. Four different designs and two different materials were studied within this work.

Bipolar plates contain the necessary flow fields to distribute the reactants and drain the water generated and the cooling channels either for coolant air flow or water flow, and gasket grooves and mechanisms. The bipolar plate production is one of the most time consuming and expensive part of the fuel cell stack production. The major

techniques for the bipolar plate production include CNC machining, composite injection molding, metal pressure forming in mold, and metal chemical etching. CNC machining is applicable for the prototype production but it is not feasible for the mass production. Graphite-polymer binder composites can be injected molded for high number of bipolar plates. The stack and fuel cell system producers which sell their products commercially usually follow this approach. The main reason of using graphite and graphite composites is the chemical resistance of graphite. However, their electrical and thermal resistance is higher than metals. There are some efforts to use metallic bipolar plates. Their electrical and thermal properties are better than graphite. Mechanical properties are also perfect. The only problem with metallic bipolar plates is the surface corrosion and high contact resistance because of this corrosion. For the corrosion protection metallic coatings and conductive inks can be applied to active area interface of the bipolar plates.

#### 5.2.1 Bipolar plate Design 1

Bipolar plates having  $12.25\text{cm}^2$  shown in Figure 5.7 was designed and manufactured on graphite by means of the CNC router. Active area of the plates was machined  $300\mu\text{m}$  above the gasket area. The channels and lands are 1mm wide and 1mm depth. The active area of the plates designed and manufactured having three parallel serpentine flow channels.

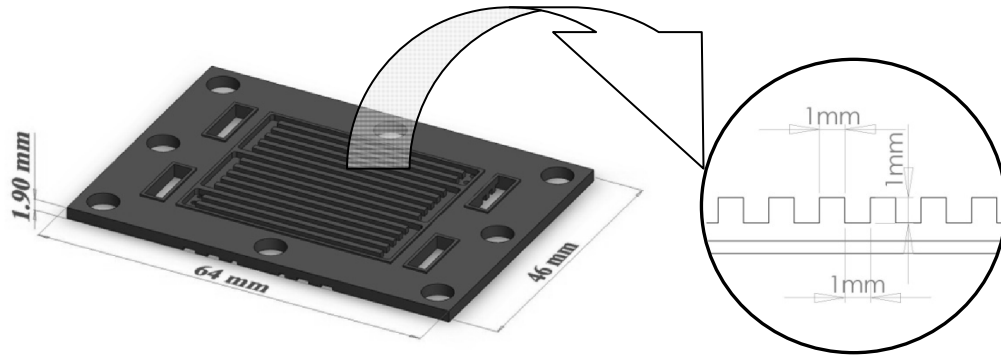


Figure 5.7 CAD solid model of graphite bipolar plate Design 1

### 5.2.2 Bipolar plate Design 2

Bipolar plate Design 2 has an active area  $34 \text{ cm}^2$  which is 2.8 times larger than the active area of Design 1. The manifolds and gasket system are changed. A gasket groove was designed in order to use  $500 \mu\text{m}$  gaskets. The schematic view of the bipolar plate is shown in Figure 5.8 and the exploded view including bipolar plates, gaskets and MEA is illustrated in Figure 5.9. In this design the thickness of the gasket will be optimized by adjusting the depth of the gasket groove. But in this design, since the gasket will be seated in a cavity of 2mm wide and not all of the remaining part other than MEA, the sealing problems between flow channels and manifold will not be observed. The final form of the stack is shown as a CAD model in Figure 5.10. The compression mechanism was completely renewed. The number of the compression rods was reduced from eight to two. The compression efficiency is expected to improve since the compression is applied from the center of the active area by a circular clamp designed. A closer look to the compression mechanism can be seen in Figure 5.11.

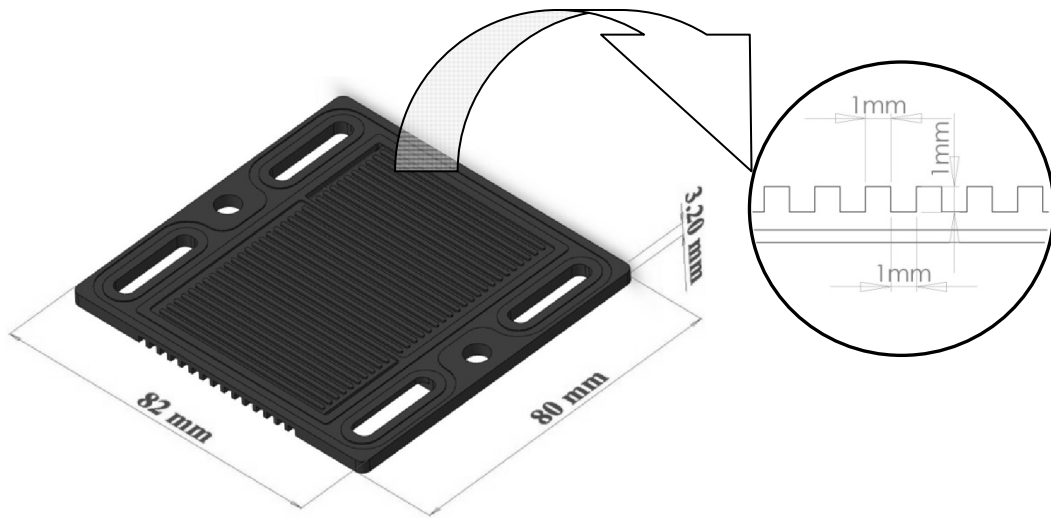


Figure 5.8 3D CAD drawing of graphite bipolar plate Design 2

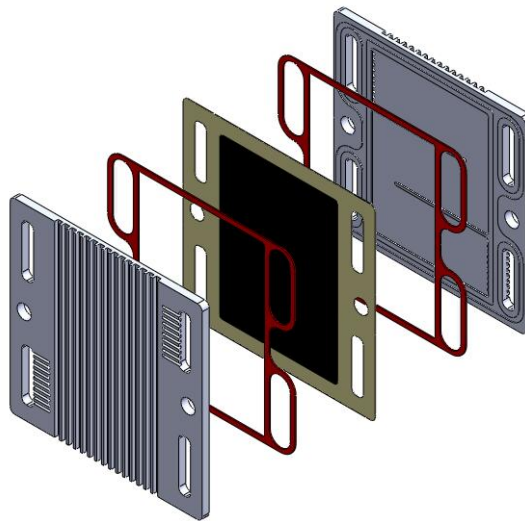


Figure 5.9 The exploded view of the single cell CAD model for bipolar plate Design 2 and gasket arrangement

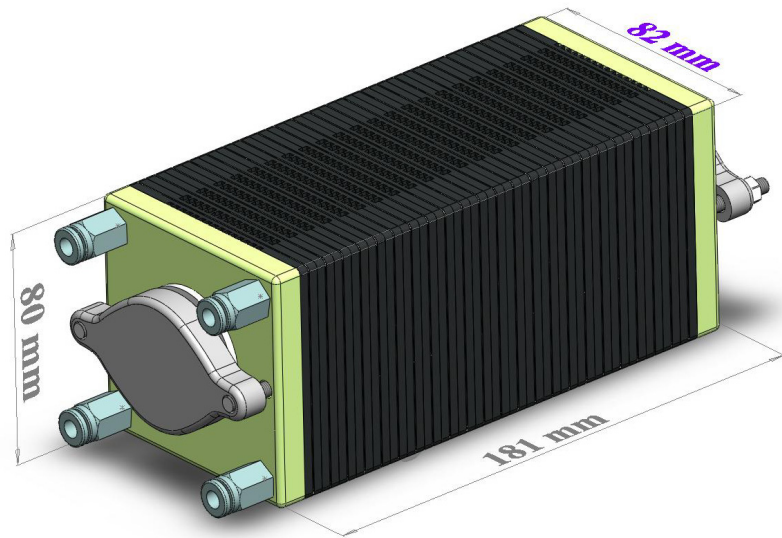


Figure 5.10 CAD Model view of the full stack assembled

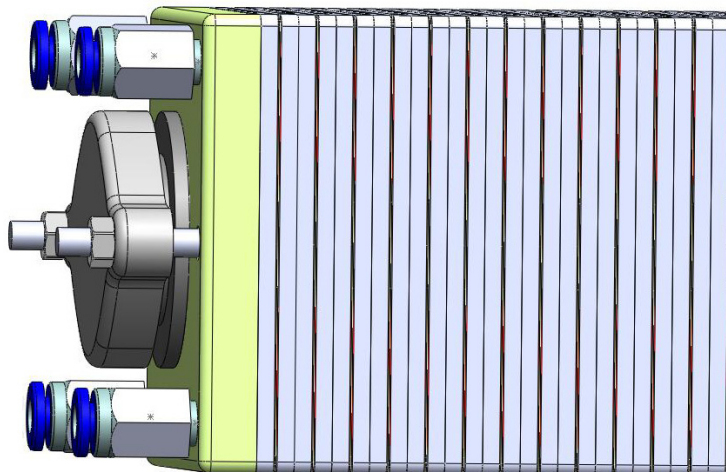


Figure 5.11 A Closer look to the compression mechanism of the stack

### 5.2.3 Bipolar plate Design 3

The bipolar plate and stack design proposed in Design 1 and Design 2 have resulted critical problems that must be solved. The problems are as follows;

- I) Epoxy is not a suitable material for compression plates due to its bending tendency at the temperatures of the operation
- II) Gas leakage could not be prevented.
- III) High contact resistance was observed.

The proposed bipolar plate and stack Design 3 is shown in Figure 5.12 and Figure 5.13, respectively. While designing the third stack, the problems of the previous designs were taken into account. The critical problems are solved as follows;

- I) The compression plates was designed and manufactured by aluminum alloy 5754. Therefore, the bending of the compression plate was reduced. The compression plate is also used as current collector.
- II) The vertical size of the cell is reduced to stop the gas leakage around the corners.
- III) The bipolar plate material was changed to aluminum which will enable solder joining of the cell plates to form bipolar plates. Therefore, the back side sealing problem and high contact resistance problems will be solved.

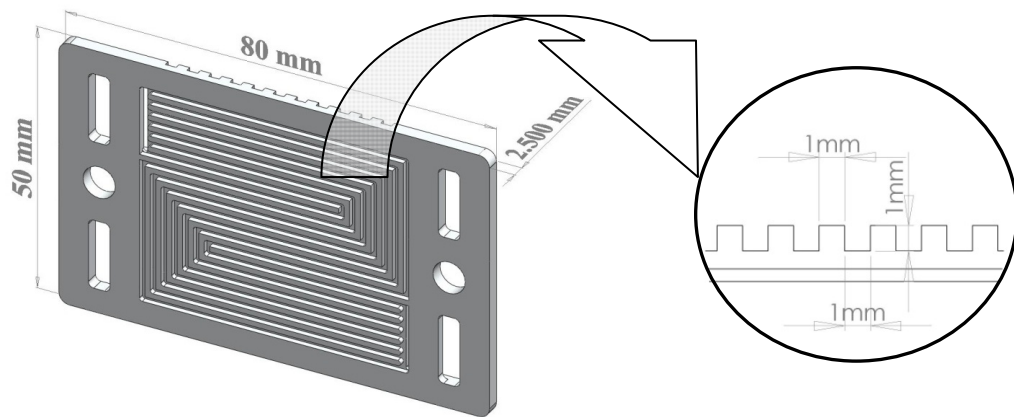


Figure 5.12. 3-D schematic view of the bipolar plate Design 3

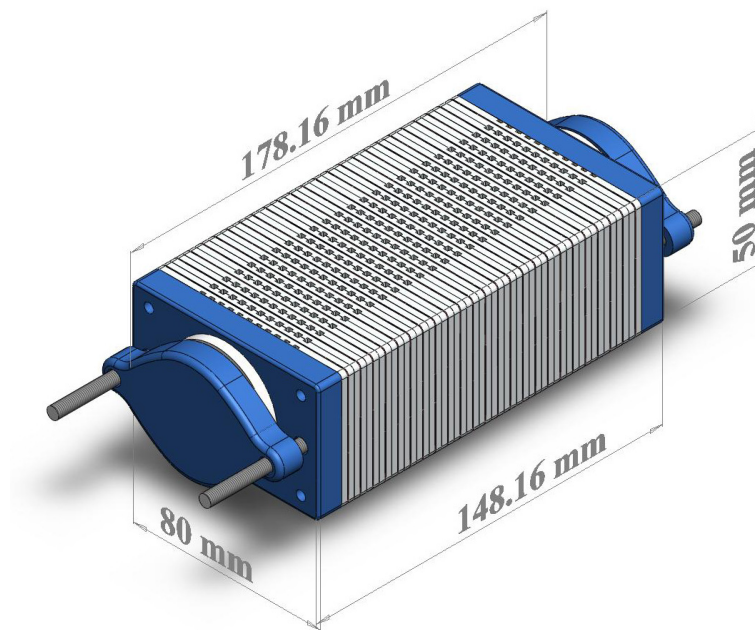


Figure 5.13. 3-D schematic view of the stack Design 3

#### 5.2.4 Bipolar plate Design 4

The fourth bipolar design is prepared in order to improve the sealing and assembling process. The flow field pattern and active area are the same as Design 3 and it is 23 cm<sup>2</sup>. The manifolds are not placed on the bipolar plates and they are designed externally as machined plastic (Delrin<sup>®</sup>) material. The proposed bipolar plate Design 4 is shown in Figure 5.14.

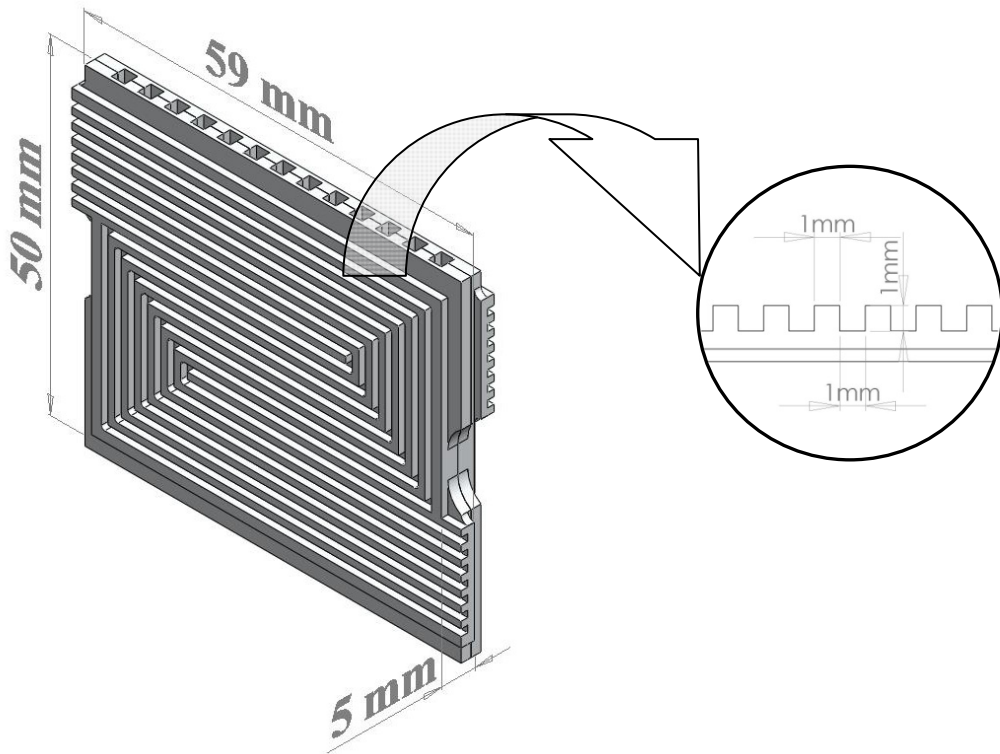


Figure 5.14 3-D schematic view of the bipolar plate Design 4

The end plates are redesigned in order to reduce the bending. The new design was made of aluminum 7075 alloy and the thickness was increased to 26.5 mm. The 3-D schematic view of the fourth stack design is illustrated in Figure 5.15.

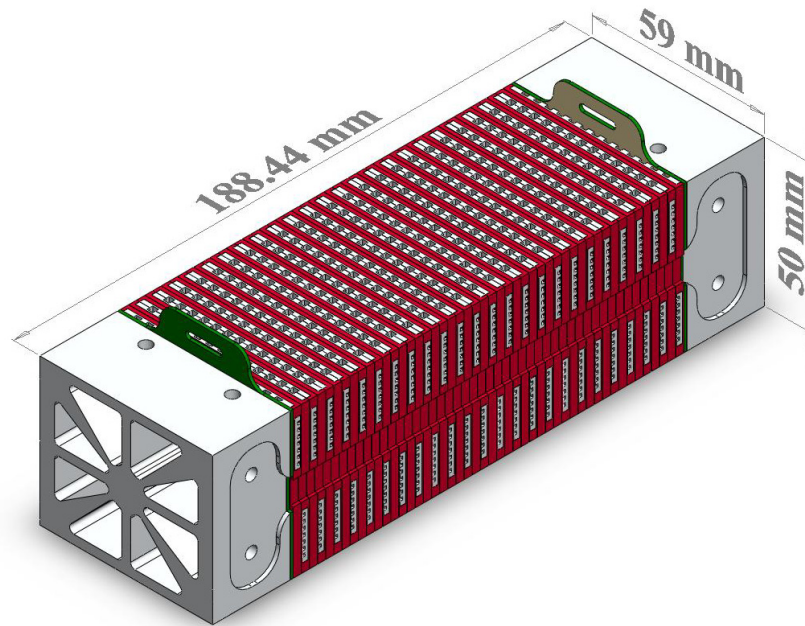


Figure 5.15 3-D schematic view of the stack Design 4 without the manifolds

### 5.3 Flow Modeling

The flow geometry of the bipolar plate Design 2 was modeled for the air flow of 0.45 slpm. For the flow modeling “Flow Simulation” tool of the Solidworks 3D CAD software was used. It should be noted that this is not a complete modeling of a fuel cell. The reaction and liquid phase flow is not considered. The assumptions of the calculations are;

- I) Isothermal flow at 60°C
- II) fully developed flow at the entrance of the channels
- III) No reaction takes place in the channel
- IV) Relative humidity is 100%
- V) No flow occurs normal to flow direction

And the boundary conditions are;

- I) Inlet flow rate is 0.45 slpm (32g/h)
- II) Outlet pressure is 1 atm

A second bipolar plate design (Design 3 and Design 4) was proposed and the same procedure was applied to model new design.

### 5.3.1 Flow modeling results of Design 2

The Flow Simulation of Solidworks software is a convenient tool for the flow modeling of the systems. When the necessary boundary conditions, thermodynamic conditions given to the tool, it can solve the equation of continuity, momentum, and energy to observe the flow behavior of the system to simulate the velocity, pressure, density, and temperature profiles.

The density profile of the air side of the flow channels is given in Figure 5.16. The right and left common channels results increasing density. The parallel channels have non-uniform densities. Therefore, some parts of the plates might not supply necessary amount of air to the reaction sites.

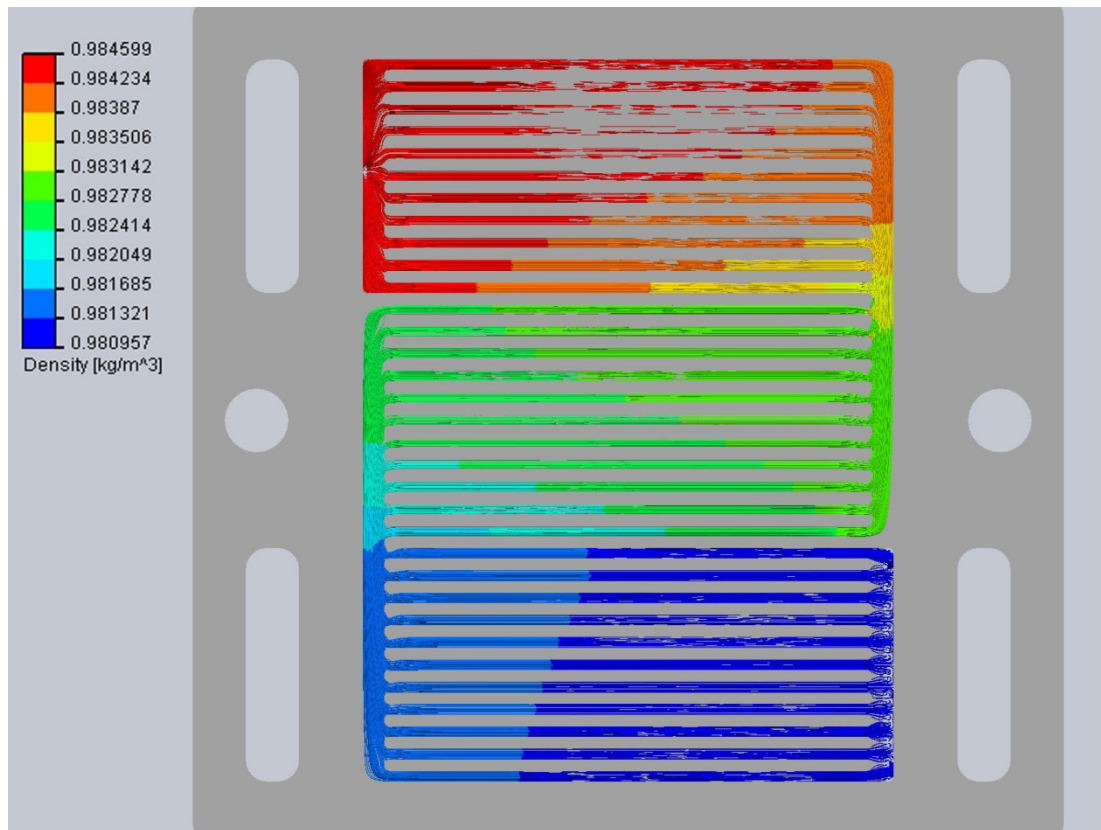


Figure 5.16 Air density profile in air flow channel of bipolar plate Design 2

The pressure distribution of the air side of the flow channels is given in Figure 5.17. The common channel on the left and right makes a sudden pressure drop which is understood from the sharp color change. Even the parallel channels have different pressure levels.

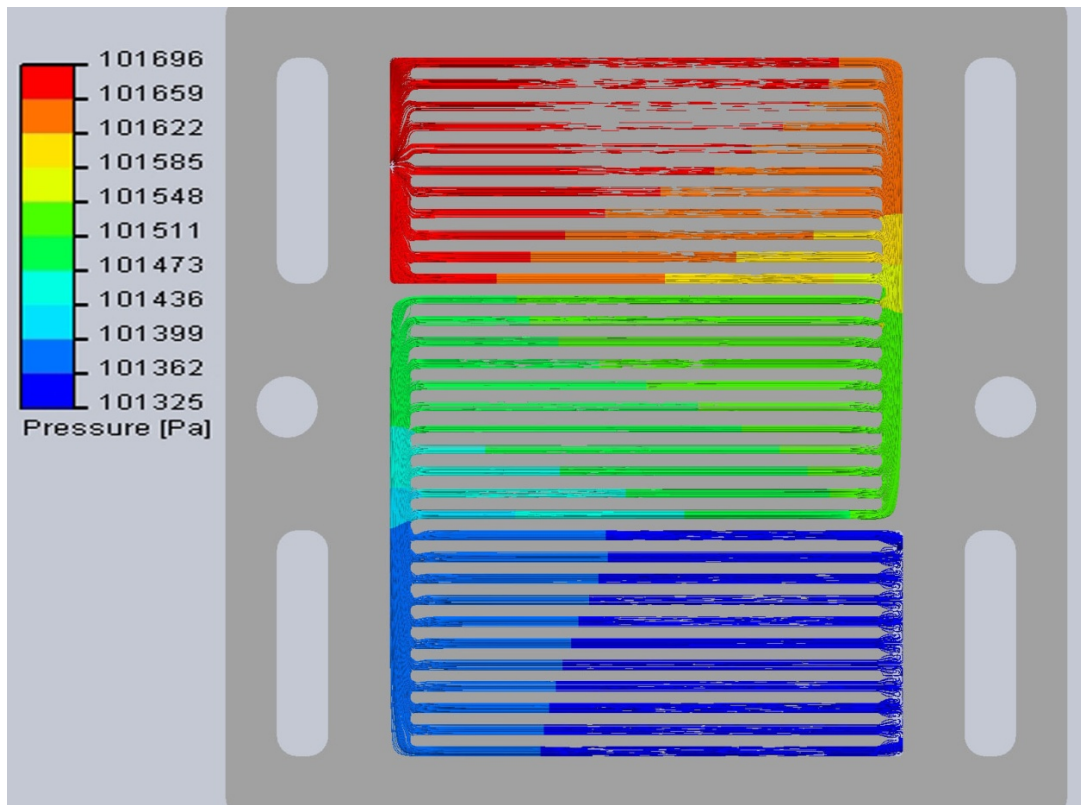


Figure 5.17 Air pressure distribution in air flow channels of bipolar plate Design 2

The velocity profile of the air side of the flow channels is a well indication of the non-uniformity of the flow as given in 5.18. The common channels have strong negative effect on the flow. As the air reaches the common channels, the velocity increases and the most of the gas reaches the far end of the channels. This means that many of the channels cannot be used since the gas does not prefer to flow from the channels shown as dark blue where the air is stagnant.

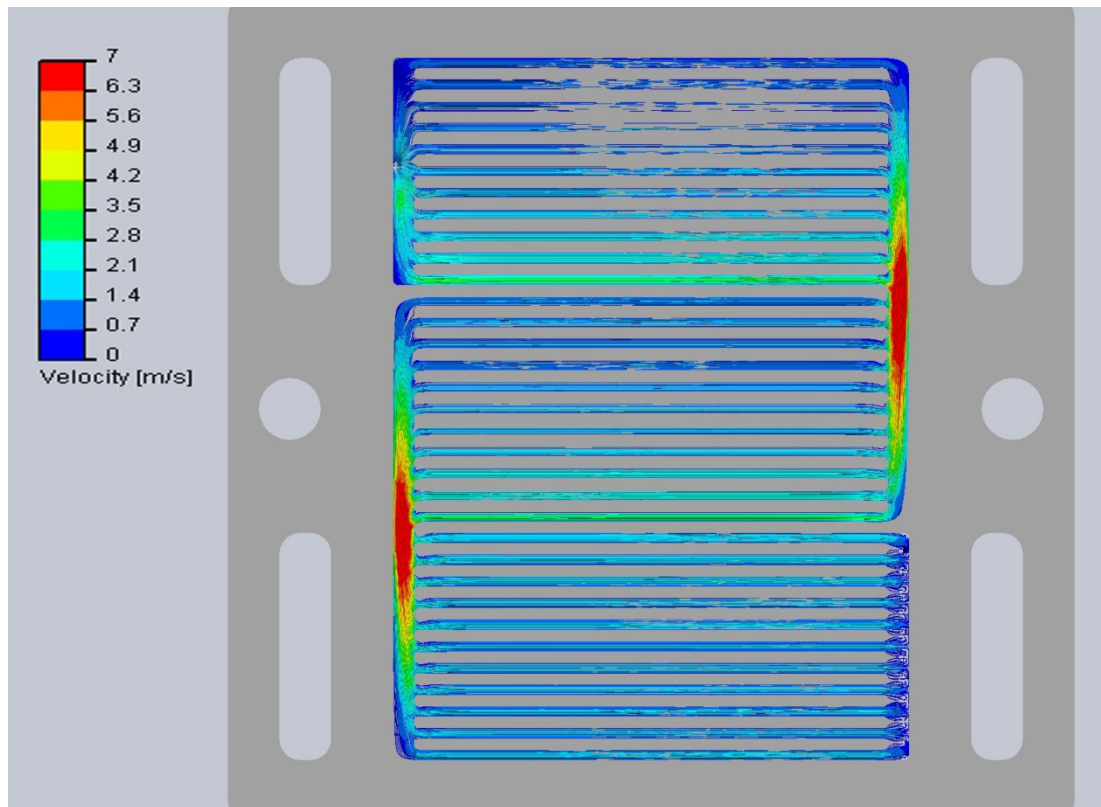


Figure 5.18 Air velocity profile of the bipolar plate channel Design 2

### 5.3.2 The modeling results of Design 3 and Design 4

Based on the information observed from the flow simulation studies shown in Figure 5.16 to 5.18, the necessity of changing the flow geometry was resulted. New flow channel geometry was designed and simulated. The density distribution, pressure and velocity profiles were given in Figure 5.19 to 5.21. The density of the air reduces similar to pressure change profile in the channels. Nearly uniform velocity distribution is observed throughout all the channels. Therefore, this flow geometry was decided to manufacture.



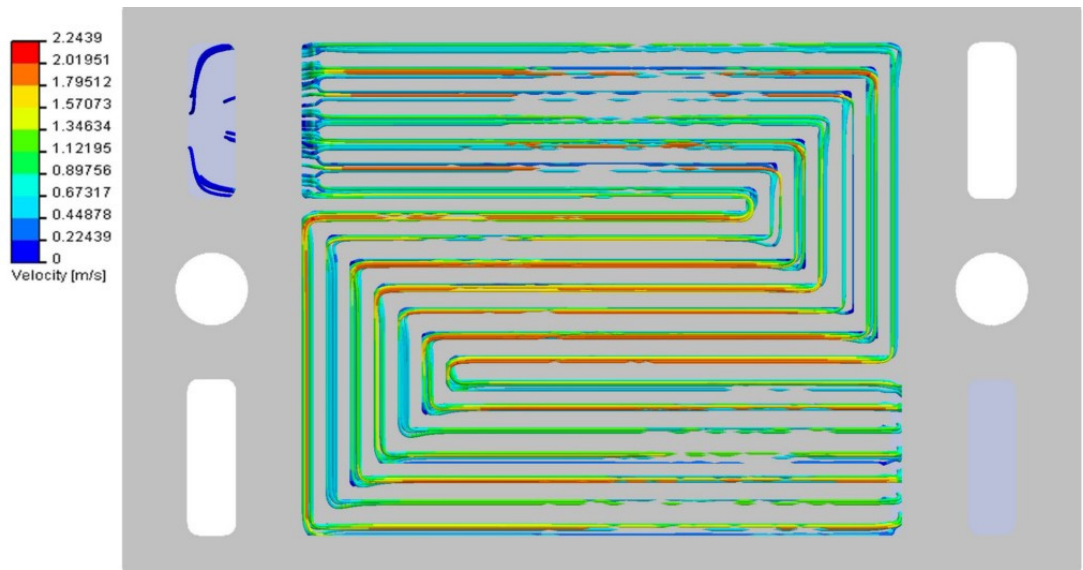


Figure 5.21 Air velocity profile of the bipolar plate channel Design 3 and 4

## CHAPTER 6

### RESULTS and DISCUSSION

The results of the membrane electrode assembly development, aluminum and graphite bipolar plate manufacturing methods, the durability of the bipolar plate coatings, and the performance of the developed and manufactured fuel cell stacks are illustrated and discussed in this chapter.

#### 6.1 Results and Discussion for MEA Development

##### 6.1.1 Performance of MEAs prepared with hand spray coating

The fuel cell prepared with the membrane electrode assemblies manufactured by hand spraying method was tested. The hydrogen and oxygen flows are set to 0.1 slpm. The cell temperature is controlled to be stable at 70°C. In order to supply the reactant gases at 100% relative humidity, the humidifier and heated transfer lines kept at 70°. The polarization curve obtained after stable conditions is given in Figure 6.1. The maximum power density is observed as 0.3 Wcm<sup>-2</sup> at 0.45V. The resistance of the cell which is calculated from the slope of the linear part of the polarization curve is 0.55Ω.

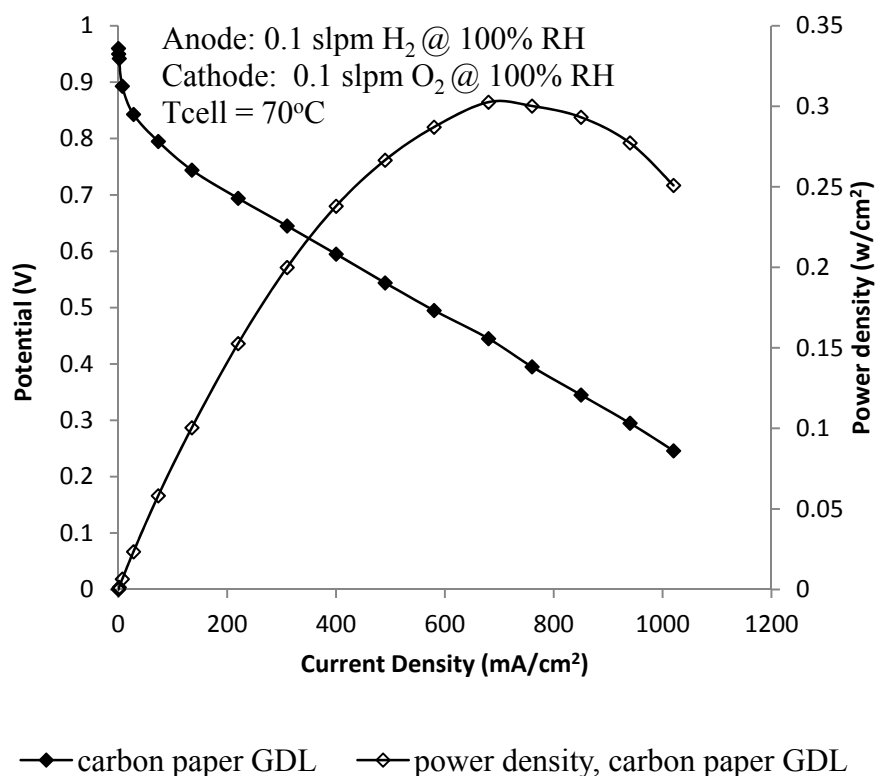
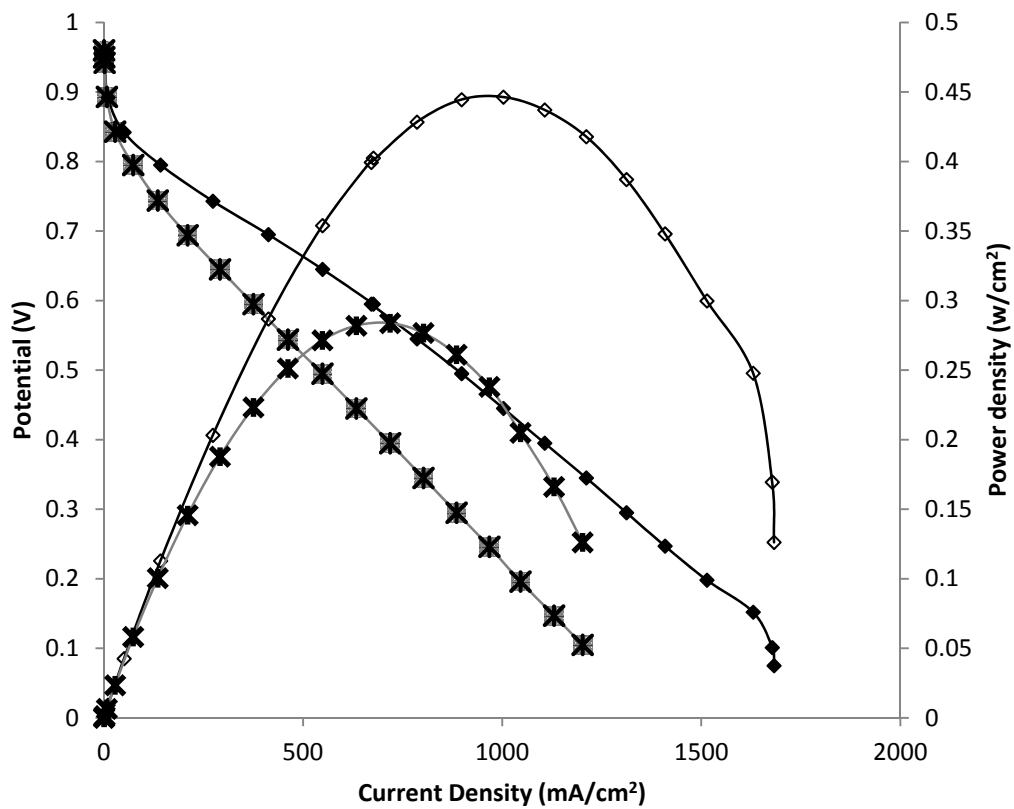


Figure 6.1 Polarization curve for the fuel cell assembled with the MEA prepared with 20%Pt/C catalyst by hand spraying method

### 6.1.2 The effect of gas diffusion media on the performance of PEM fuel cell

Both carbon paper and carbon cloth GDLs were tested with Electrochem's single cell hardware made of graphite with serpentine channels. The results of these tests are shown in Figure 6.2. The highest power density reached with the carbon paper GDL operating at 70°C cell temperature was 0.39Wcm<sup>-2</sup>. Whereas it was 0.28Wcm<sup>-2</sup> for carbon cloth GDL in the same cell with the same operating conditions. The cell built with the carbon paper GDL had a resistance of 0.51Ω whereas the resistance of the cell assembled with carbon cloth GDL was 0.60Ω.



- ◆— carbon paper GDL
- carbon cloth GDL
- ◇— power density, carbon paper GDL
- ×— Power density, carbon cloth GDL

Figure 6.2. The effect of GDL on the performance of serpentine channeled cell operated at 70°C in stable conditions

### 6.1.3 The effect of gasket thickness on the performance of PEM fuel cell

Figure 6.3 illustrates the effect of gasket thickness on the performance of Electrochem 5cm<sup>2</sup> active area cell assembled with the carbon paper GDL. It is clearly seen Figure 6.3 that by an increase in gasket thickness (110micron) the cell resistance increases from 0.51Ω to 0.94Ω. In consequence, the maximum power decreases from 0.45Wcm<sup>-2</sup> to 0.28 Wcm<sup>-2</sup>.

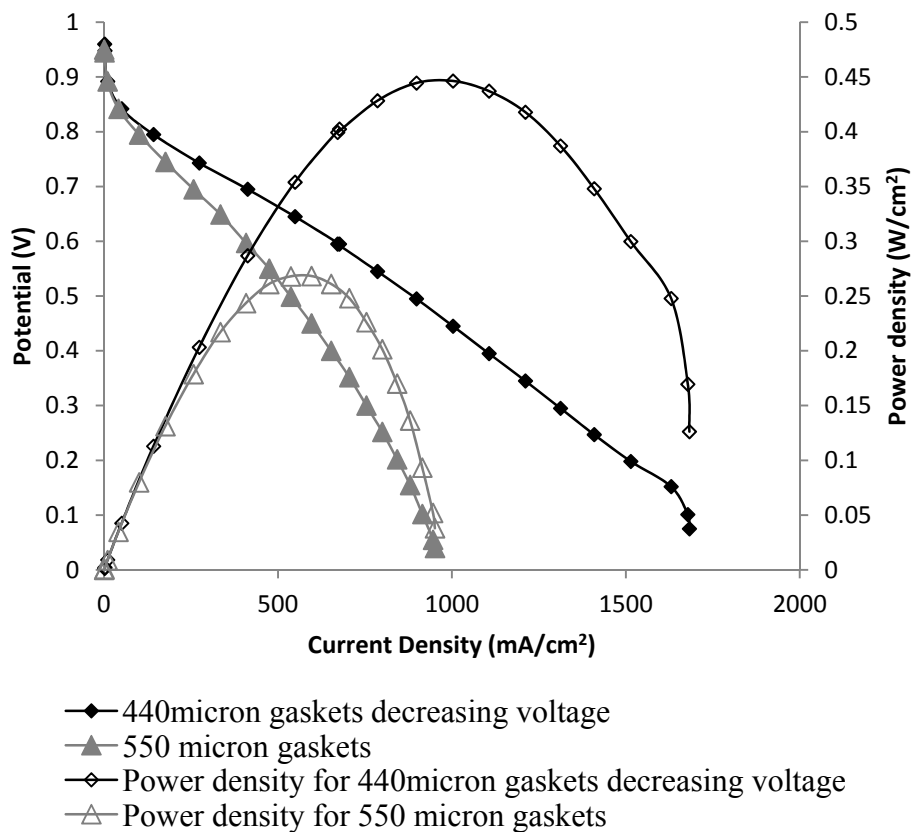


Figure 6.3. The effect of gasket thickness on the performance of serpentine channelled cell with GDL 30BC carbon paper GDL operated at 70°C in stable conditions.

#### 6.1.4 Performance of newly developed MEAs

Ultrasonic coating machine was used to prepare MEAs having 5 cm<sup>2</sup> active areas in order to determine the performance of the newly developed MEA production method. Two different techniques were tried. In first method, the catalyst ink directly coated to the membrane to form 3 layers MEA first and the GDLs were pressed to this 3 layer MEA to form a 5 layer MEA. In the second method, the catalyst ink was coated on the GDLs to form gas diffusion electrodes (GDEs) and these GDEs were pressed both side of the membrane to form 5 layers MEA.

The comparison of the performances of the MEAs prepared by membrane or GDL coating is shown in Figure 6.4. The same amount (0.32 mg Pt/cm<sup>2</sup>) of platinum loading was applied with 88 pass to both MEAs. Membrane coated MEA has the highest power at 0.4 V and the corresponding power is 0.42 W/cm<sup>2</sup>. Whereas, the MEA produced by GDL coating has the highest power at 0.5V and the corresponding power is 0.5 W/cm<sup>2</sup> which 20% higher than the membrane coated MEA. Both cells have the same resistance which is 0.32 ohm.

The performances of the GDL coated MEAs prepared by 88 pass (0.32 mg Pt/cm<sup>2</sup>) or 110 pass (0.4 mg Pt/cm<sup>2</sup>) are compared in Figure 6.5. A small increase in the power density is observed when the Pt loading is increased to 0.4 mg. However the characteristics of the both cells very similar by just looking the current-potential (IV) curves. However, an observation during the performance tests was interesting. The cell having lower platinum loading had a very quick response to show the given performance. However, the cell with higher Pt loaded MEA started with low performance and the performance increased gradually. This might be because of the electrode thickness and the porosity of the electrodes.

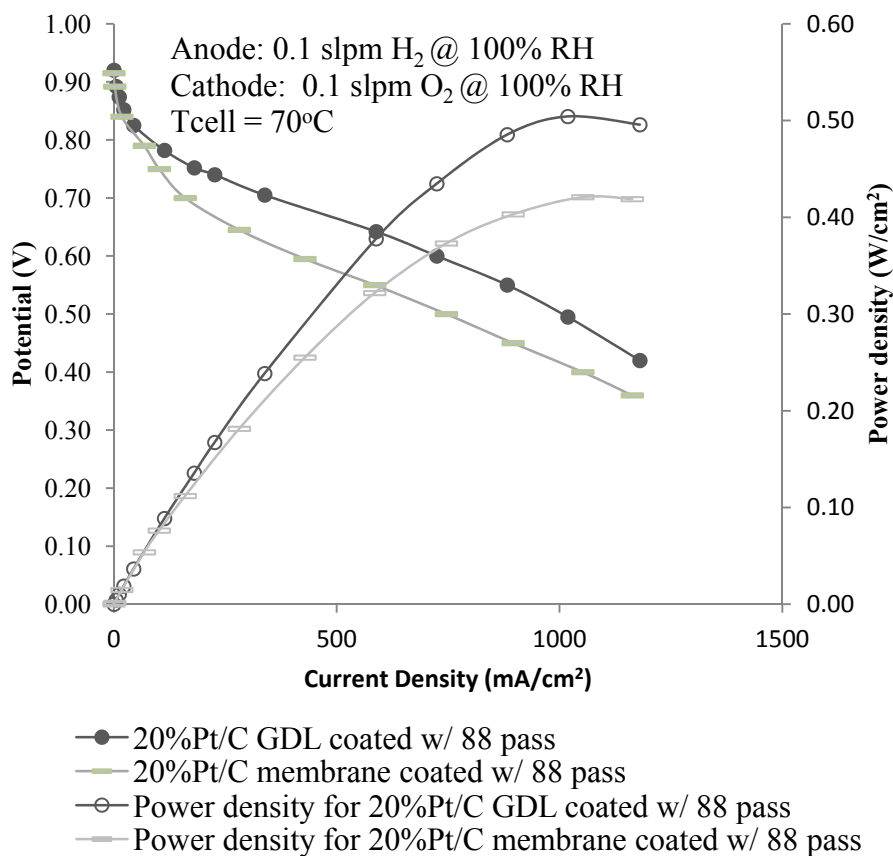


Figure 6.4 Comparison of the polarization curves of the MEAs produced by membrane coating or GDL coating

The effect of the catalyst Pt content on the performance of the fuel cells having MEAs prepared with ultrasonic coated electrodes is shown in Figure 6.6. The performance of the fuel cell with the MEA prepared using 40% Pt/C catalyst was incredibly high. The highest power reached with this cell is 0.74 W/cm<sup>2</sup> at 0.45 V which is not only a lab record, but also, the performance is higher than the commercial MEAs which were the highest performance MEAs ever tested in our laboratory, previously. The comparison of the performances of the MEAs produced in this work with the commercial MEA is shown in Figure 6.7.

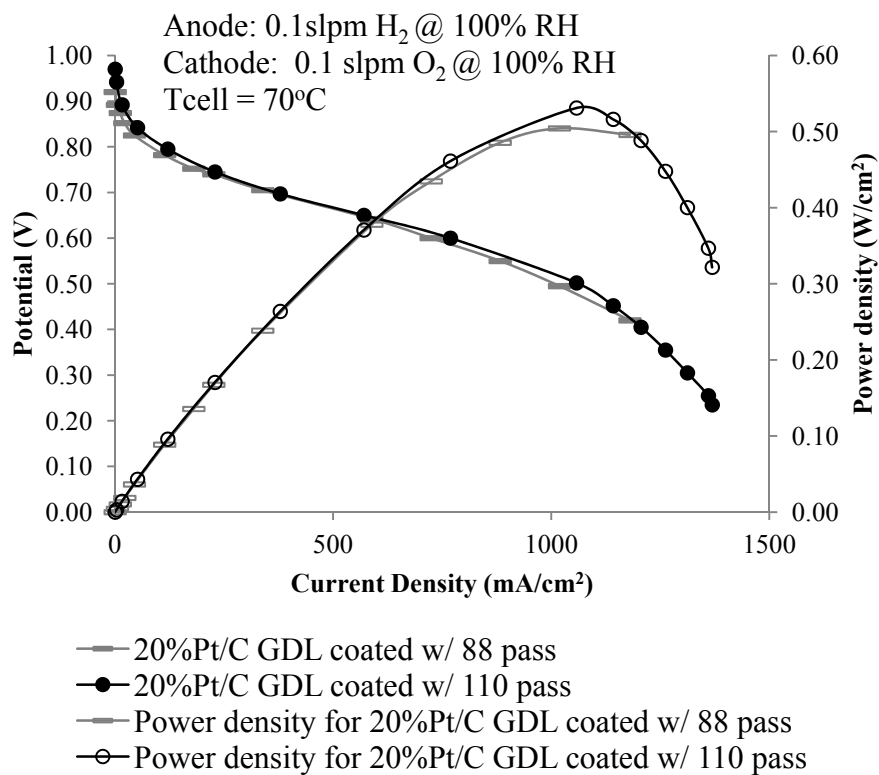


Figure 6.5 Comparison of the polarization curves of the GDL coated MEAs produced by 88 (0.32mg Pt/cm<sup>2</sup>) pass or 110 pass (0.4mg Pt/cm<sup>2</sup>) with the same catalyst ink

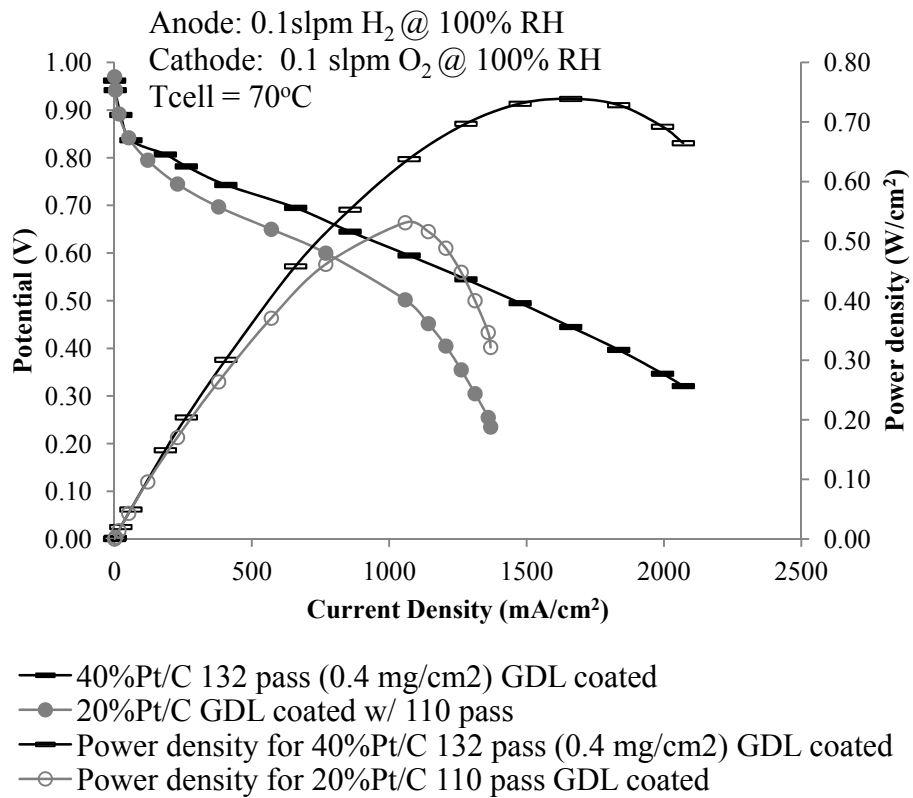


Figure 6.6 The effect of the catalyst Pt content on the performance of the fuel cells having MEAs prepared with ultrasonic coated electrodes

Even with the 20% Pt containing catalyst newly developed MEAs presented in this study have a better performance than the commercial OMG MEA which was the old record holder of our laboratory.

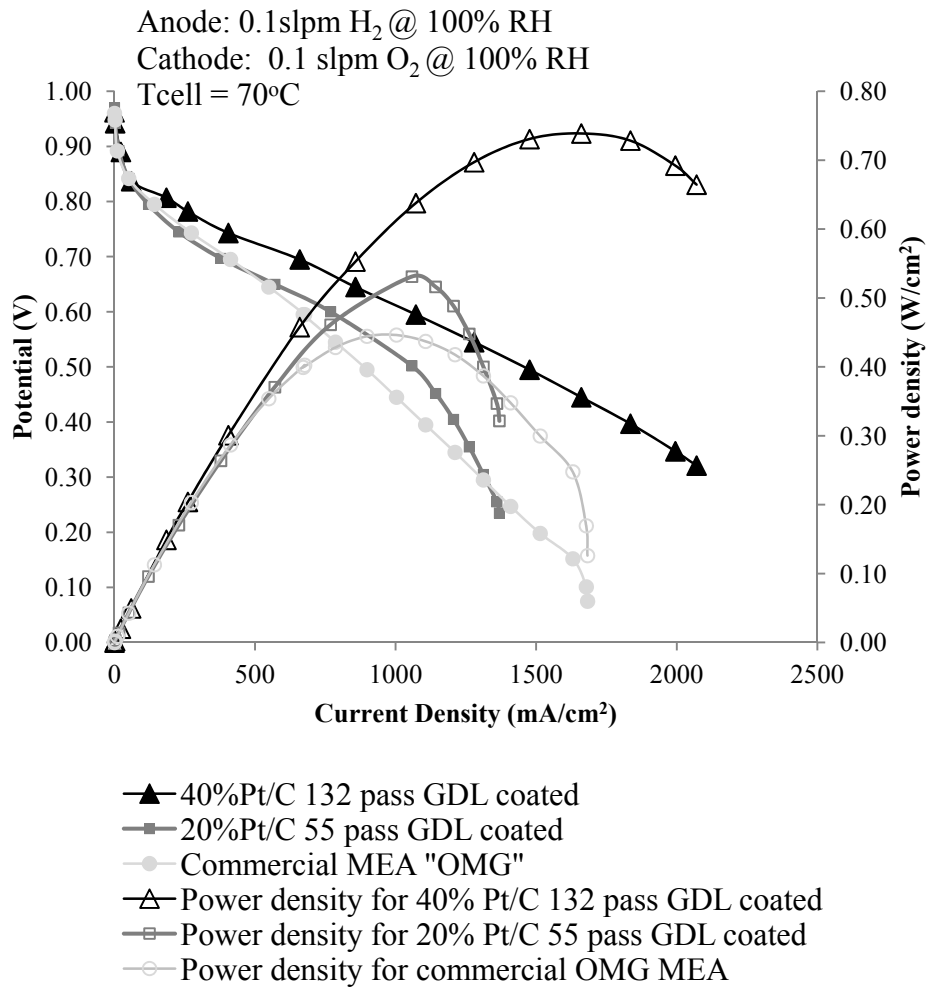


Figure 6.7 The comparison of the performances of the MEAs produced with 20% and 40% catalyst and commercial MEA

The comparison of the performances of the MEAs prepared by 40%, 50% or 70% catalysts coated onto GDL is shown in Figure 6.4. The same amount (0.4 mg Pt/cm<sup>2</sup>) of platinum loading was applied with 110 pass to MEAs. The MEAs prepared with 40%, 50%, and 70% Pt/C catalysts has the highest power at 0.45V, 0.45V and 0.5V, respectively. The corresponding power densities are 0.74, 0.77, and 0.88 W/cm<sup>2</sup>, respectively. The power or current density of a PEM fuel cell is affected by many

different parameters other than the MEA. The preparation method and materials of the MEA also differ in the published studies. There is no straightforward comparison with the literature. However, it is known that  $1000 \text{ mA/cm}^2$  current density is a typical value for a single PEM fuel cell operating at  $0.6 \text{ V}$  potential. Qi and Kaufman [41] achieved power densities as high as  $0.72 \text{ W/cm}^2$  at cell temperature of  $75 \text{ }^\circ\text{C}$ , for a cathode with a Pt loading of  $0.12 \text{ mg/cm}^2$ .

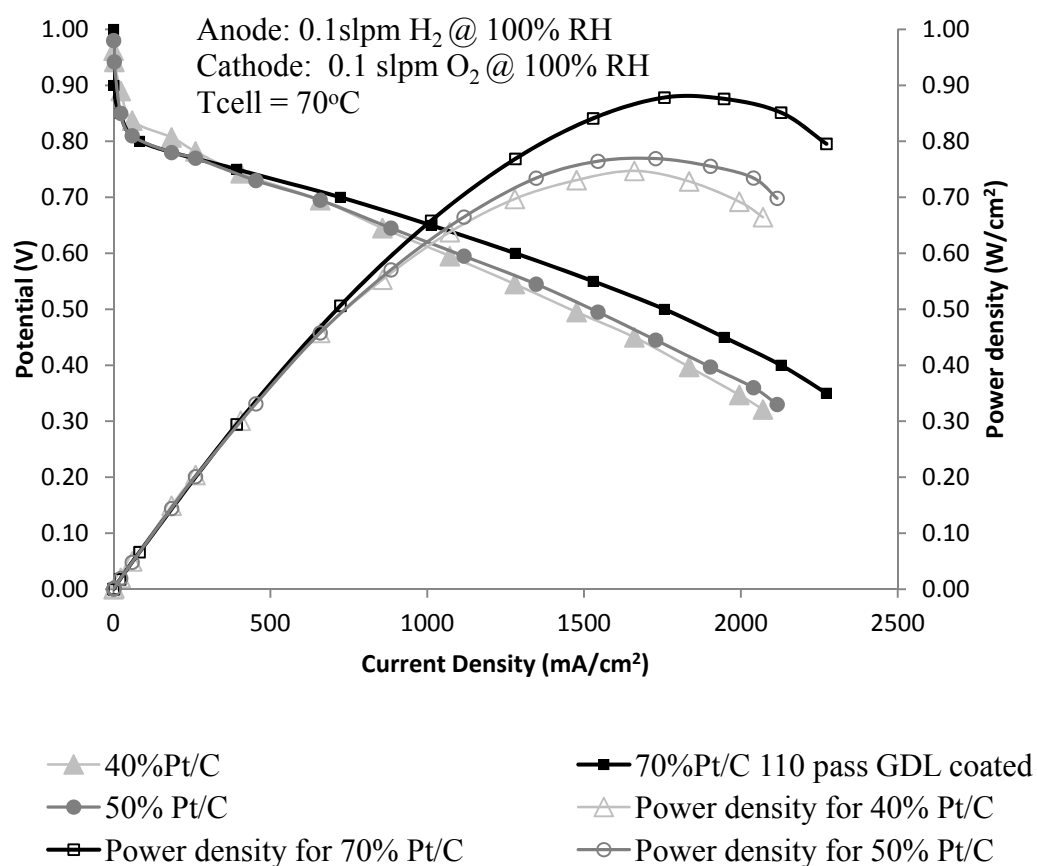


Figure 6.8 Comparison of the polarization curves of the MEAs produced 40%, 50% or 70% Pt/C catalysts

Endoo et.al. [42] studied the identification of the key variables for the MEA preparation that affects the PEM fuel cell performance. The maximum performance achieved is  $393 \text{ mA/cm}^2$  (Pt loading:  $1 \text{ mg Pt/cm}^2$ ) and  $566 \text{ mA/cm}^2$  for the in-house prepared and commercial MEAs, respectively. Thanasilp and Hunsom [43] evaluated the effect of MEA fabrication techniques on the performance of Pt-Pd/C catalyst used in PEM fuel cell. The maximum power density achieved is  $0.21 \text{ W/cm}^2$  at  $0.6 \text{ V}$  cell potential with catalyst loading of  $0.15 \text{ mg/cm}^2$ .

The resistances calculated from the linear part of the polarization curve are  $0.24$ ,  $0.22$ , and  $0.19 \text{ } \Omega$  for the fuel cells assembled with MEAs prepared with 40%, 50% and 70% Pt/C catalysts, respectively.

## **6.2 Effect of Contact Resistance on PEMFC Performance**

Before manufacturing the stack components, a single cell is assembled and tested to verify the performance status of the components. Problems with the flow field, a gasket problem resulting reactant leak or a compression problem are identified. Figure 6.9 shows the exploded view of the tested single cell assembly for Design 2. Liquid gasket was used for the seals of the gas connections between the compression plate and the copper current collectors and also for between the current collectors and graphite plates. Polarization curve data were measured from collecting the voltage data from the points  $V_{m1}$  and  $V_{m2}$  shown in Figure 6.9. Current was drawn from the current collectors in both of the cases.

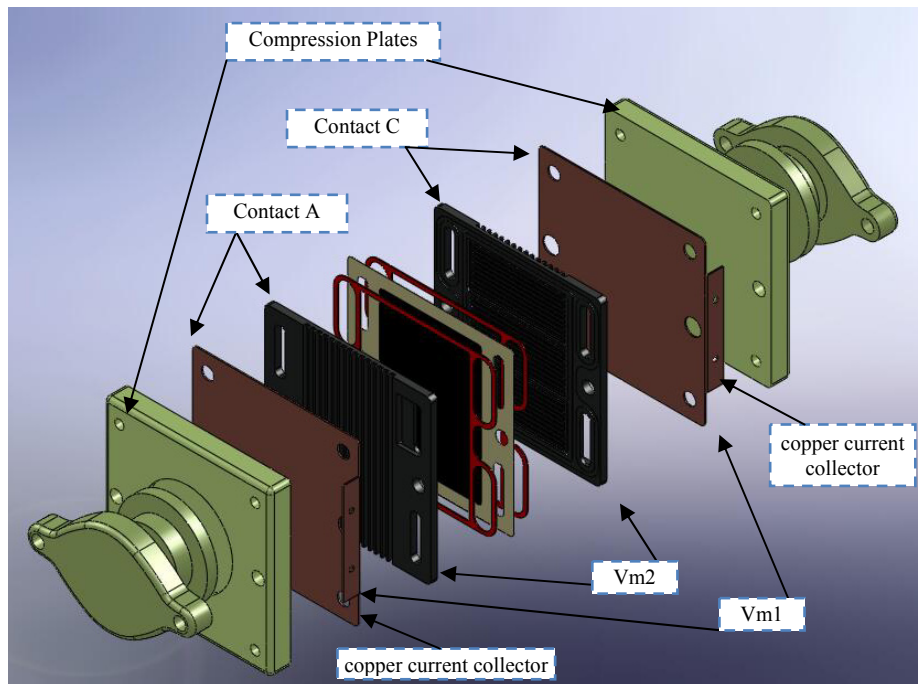


Figure 6.9. Exploded view of the single cell assembly for Design 2

Single cell assembly for Design 2 was tested as described in Section 4.5 with the Fideris test station. The cell was operated with air and oxygen to compare the results. Initially, as usually performed, the voltage measurement is obtained from the load cables which are connected to current collector plates shown as Vm1. During the test it was realized that the actual potential at the cell (voltage measured directly from the graphite plate, Vm2) is much higher than the voltage measured from the current collector plate. Figure 6.10 shows the polarization curve of the cell at 50 °C operating temperature with pure oxygen fed to cathode. Since the slope of the linear region of the polarization curves give the total ohmic resistance of the cell, it is observed from the curves that the contact resistance had a significant effect on the performance of the whole cell. The resistance of the cell eliminating the copper current collector plate was calculated as 0.76 ohm (the slope of the light grey curve,  $R=V/I$ ). When the polarization curve data taken with the voltage measured from the

current collector plate, the resistance was 1.58 ohm. That means that the difference of the resistance comes from the contact resistance of the copper current collector plate with the graphite plate which is 0.82 ohm. That means that the contact resistance of the current collector plate is even higher than the contact resistance of GDL plus resistance of GDL itself plus the ionic transfer resistance. The reason of the high contact resistance between the graphite plate and copper current collector plate is most probably the rapid corrosion of the copper contact surface. Although it was planned to have a gold coating on the surface of the copper plate, it was thought that it might be tolerable for short period of time at least for the initial testing for few days. However, the results shown in Figure 6.10 and Figure 6.11 state that even a few hours of operation with a copper plate is not possible. Moreover, it is an indication of importance of the contact resistance between the graphite plates in the stack. Since all of the cells will be connected in series, even a small amount of resistance at the contacts become very significant which becomes even higher than the resistance in the GDL and membrane as proton transport. If one discards the contact resistance at the current collector and graphite plate interface, the highest power density reached with the oxygen is  $0.2 \text{ W/cm}^2$  which reduces to approximately  $0.1 \text{ W/cm}^2$  if the contact resistance exists. In either case since the load observes the additional 0.82 ohm resistance, it was not possible to get the polarization behavior of the cell below 0.5V since the load measures actually 0V and the rest of the electrical energy is dissipated in the resistance of interface to heat.

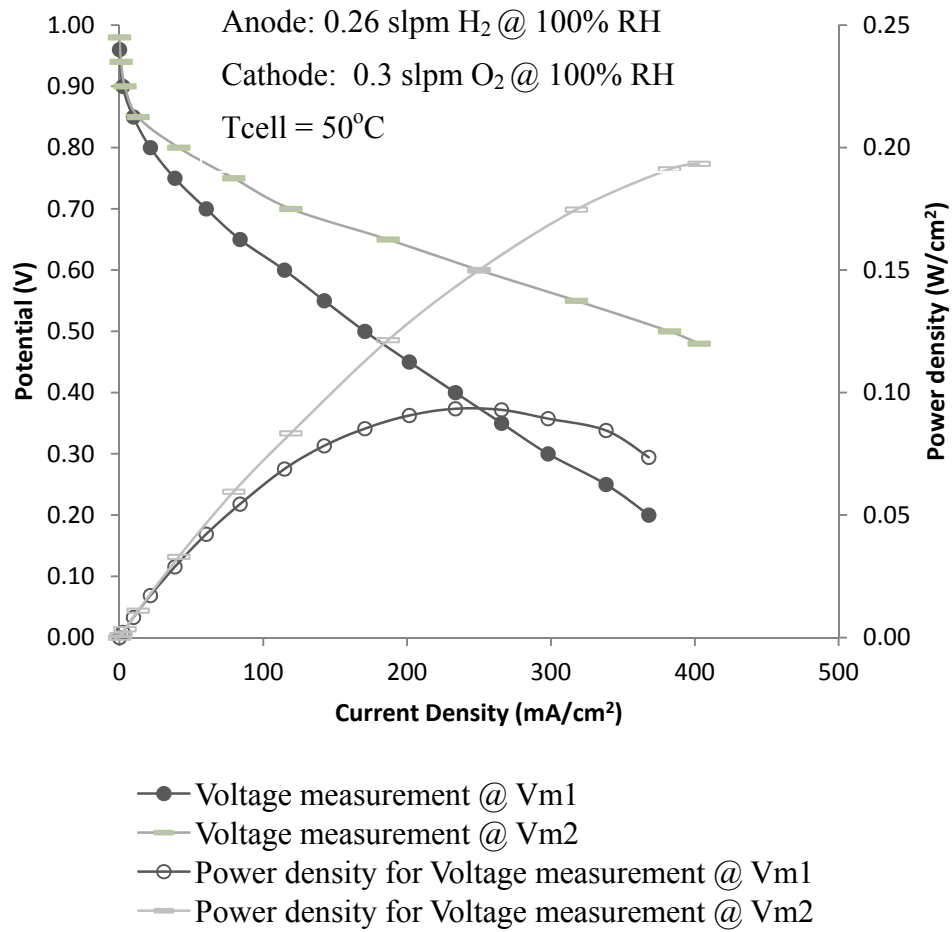


Figure 6.10. Polarization curve of the assembled single cell with oxygen operation – cell voltage was measured two different points

A similar behavior was also observed when the cell is operated with air fed to cathode to supply oxidant (see Figure 6.11). In this case the maximum power was obtained as approximately 0.12W/cm<sup>2</sup> which is 60% of the pure oxygen operation. The resistance of the cell eliminating the copper current collector plate was calculated as 1.35 ohm (the slope of the light grey curve,  $R=V/I$ ). When the polarization curve data taken with the voltage measured from the current collector plate, the resistance was 2.46 ohm. That means that the difference of the resistance

comes from the contact resistance of the copper current collector plate with the graphite plate which is 1.11 ohm. The contact resistance cannot be related with the reactant fed to the cathode. This increase of the contact resistance might be because of the continuing corrosion of the copper surface. Since the test with air was performed after the test with oxygen the contact resistance the increasing corrosion resulted to reduction of performance and increase of contact resistance.

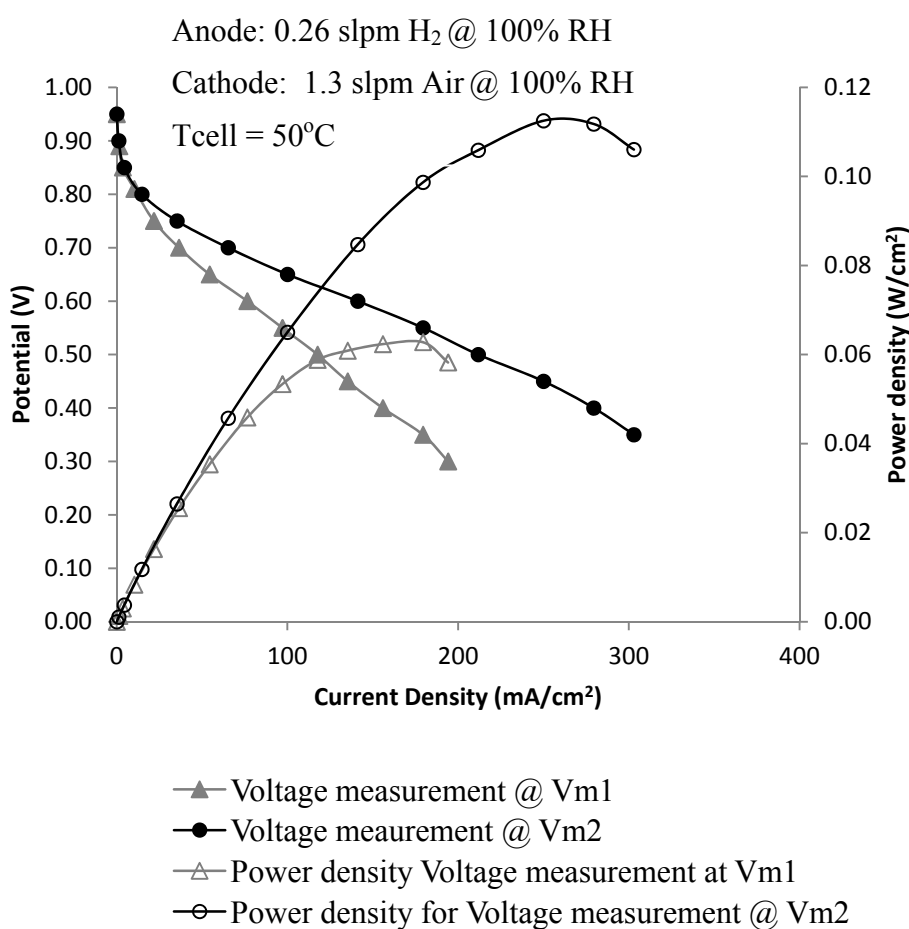


Figure 6.11. Polarization curve of the assembled single cell with air operation – cell voltage was measured two different points

The comparison of the polarization curves of the 34cm<sup>2</sup> single cell with oxygen and air operation is given in Figure 6.12. The open circuit potential (OCV) of the cell operated with pure oxygen at cathode was 0.98 V. When the operation switched to air the OCV was reduced to 0.95V as it is expected. The performance of the PEM fuel cell operating with oxygen has higher than operating with air because of two reasons. The Nernst equation and the exchange current density are dependent on the partial pressures of H<sub>2</sub>, O<sub>2</sub> and H<sub>2</sub>O as illustrated in Equation 6.1 and Equation 6.2, respectively [6].

$$E = E_0 + RT \ln\left(\frac{P_{H_2} P_{O_2}^{0.5}}{P_{H_2O}}\right) \quad (6.1)$$

$$i_0 = i_0^{ref} \left(\frac{P}{P_0}\right)^\gamma \quad (6.2)$$

where  $i_0$  is the exchange current density,  $i_0^{ref}$  is reference exchange current density,  $\gamma$  is pressure coefficient.

For oxygen to air potential gain can be calculated as given in Equation 6.3 [6].

$$\Delta V = \frac{RT}{nF} \ln\left(\frac{1}{0.21}\right)^{0.5} + \frac{RT}{\alpha F} \ln\left(\frac{1}{0.21}\right) \quad (6.3)$$

where,  $\alpha$  is transfer coefficient.

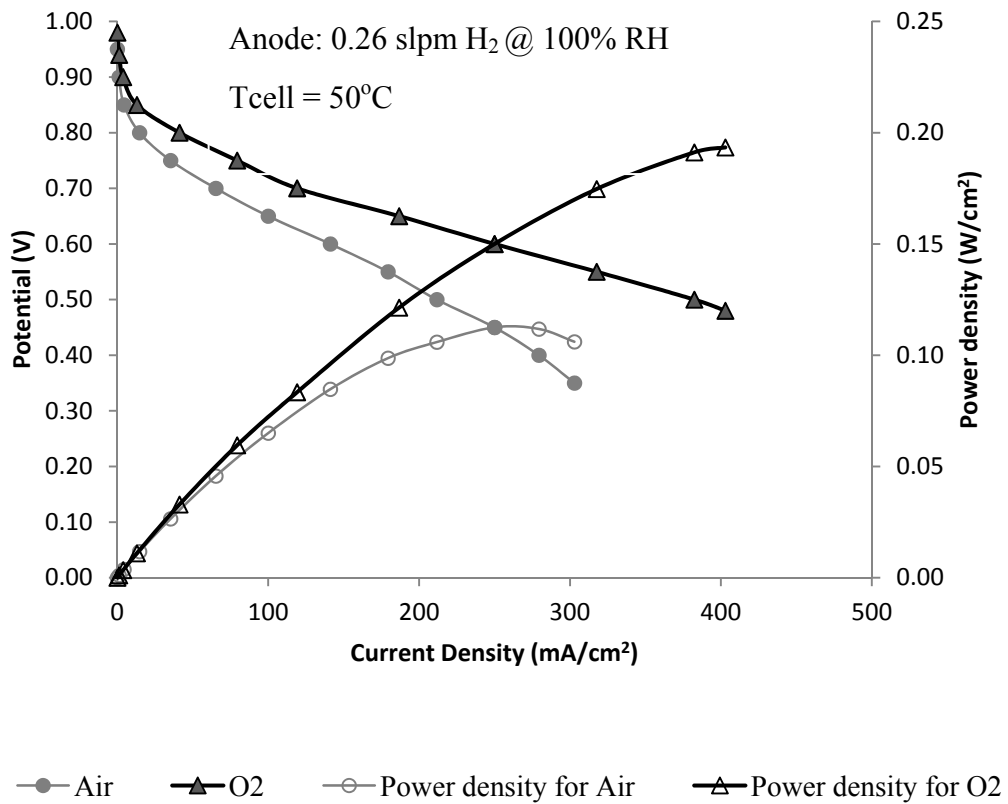


Figure 6.12. Comparison of the polarization curves of the assembled single cell with air operation and oxygen operation – cell voltage was at Vm2

When cathode pure oxygen supply switched to air potential drop,  $\Delta V$  is calculated as 57mV at 70°C operating temperature. The polarization curves obtained experimentally with the same cell using oxygen and air as oxidant are given in Figure 6.12. For the low current densities up to 150 mA/cm<sup>2</sup>, the experimental values are in accordance with the calculated potential loss. However, the higher current densities results more than the calculated potential loss. This is an evidence of the existence of mass transport limitation.

### 6.3 Results of Bipolar Plate Coating

#### 6.3.1 Performance and durability of Ni coated bipolar plates

The Ni coated bipolar plates of third stack design was tested by forming a single cell. Figure 6.13 shows the polarization curves obtained between 105<sup>th</sup> and 2425<sup>th</sup> minutes. As the time passes the performance of the fuel cell reduces. The most abrupt decrease is observed in between operation times 1645<sup>th</sup> and 2425<sup>th</sup> minutes. The continuous decrease in performance may be explained by the corrosion of the surface of active area.

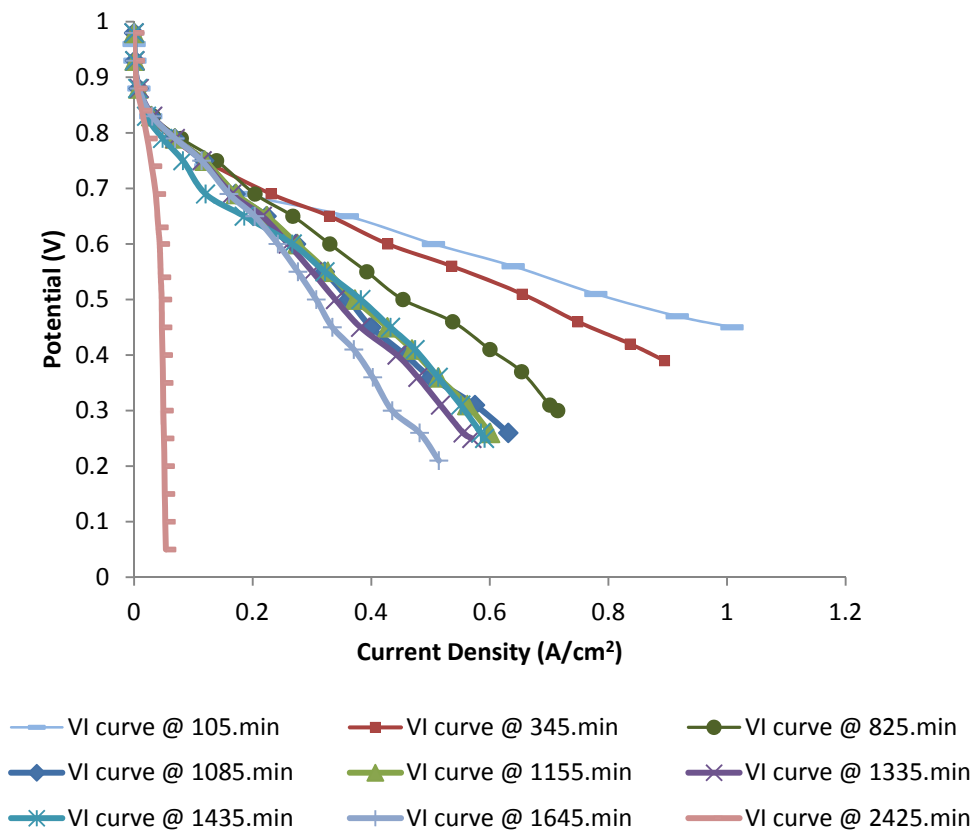


Figure 6.13 Polarization curves for nickel plated aluminum bipolar plates

Figure 6.14 illustrates the change of current density at a fixed 0.6V cell potential and the change of cell resistance throughout the continuous operation of the cell. The current density at 0.6V cell potential reduces significantly as the operation time increases. The starting current density is about 0.5A/cm<sup>2</sup> at 105<sup>th</sup> minute of operation. It reduces to 0.242A/cm<sup>2</sup> when the cell operation time is 1645<sup>th</sup> minute. It reduces nearly all of the current density at 2425<sup>th</sup> minute. Similarly, cell resistance increases as the increasing operating time. The breakthrough of the cell resistance is again 1645<sup>th</sup> minute. The cell resistance increases from 1.34 ohm to 17.65 ohm as the operating time increases from 1645<sup>th</sup> minute to 2425<sup>th</sup> minute. The degradation rate of the cell operating at 0.4 A/cm<sup>2</sup> is calculated by Equation 6.4. The degradation rate of the PEM fuel cell assembled with nickel plated bipolar plates is 6.2x10<sup>-3</sup> W/cm<sup>2</sup>h. The most probably reason of this behavior is corrosion of the contact sides of the active area on the bipolar plates. Therefore, one can conclude that Ni plating itself has not ability to protect the interface from corrosion and the aluminum plates with Ni plating is not suitable material for bipolar plate production.

$$Degradation\ rate = \frac{i(V_0 - V)}{t} \quad (6.4)$$

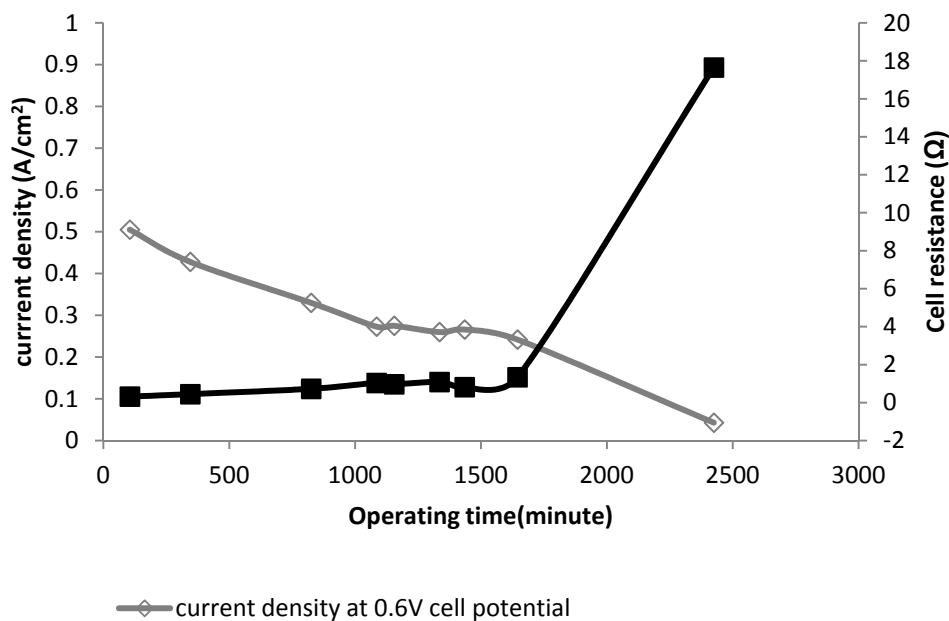


Figure 6.14 The change of current density at 0.6V cell potential and the cell resistance for nickel coated fuel cell plates

### 6.3.2 Performance and durability of solder (Sn-Ag-Ti) coated bipolar plates

The fuel cell tests are performed for Sn-Ag-Ti coated single test cell. Polarization curves were recorded between the operation times from 145<sup>th</sup> minute to 3120<sup>th</sup> minute as shown in Figure 6.15. The polarization curve obtained at 1630<sup>th</sup> minute is the best performance curve obtained throughout the test of Sn-Ag-Ti alloy coated fuel cell plate. The test is conducted up to 3120<sup>th</sup> operation time of the fuel cell and a reduction in performance was observed.

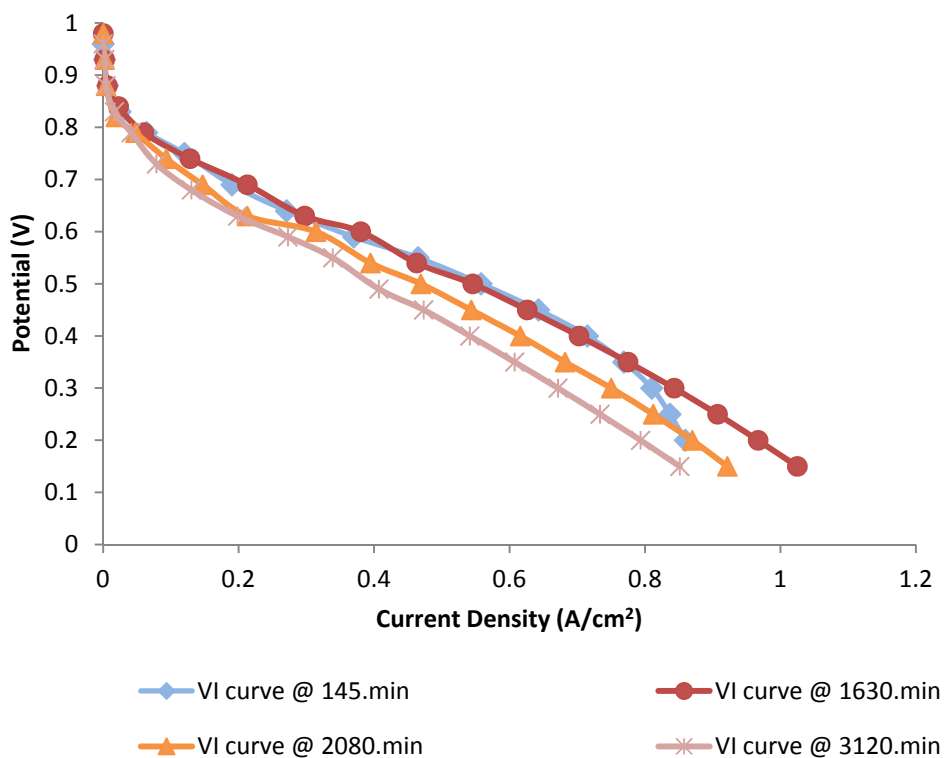


Figure 6.15 Polarization curves for Sn-Ag-Ti alloy coated single cell aluminum plates.

Figure 6.16 shows the current density change at 0.6V fixed cell potential and cell resistance change for operation time up to 3120 minute for Sn-Ag-Ti alloy coated aluminum single cell. The degradation rate of the PEM fuel cell assembled with Sn-Ag-Ti alloy coated bipolar plates is  $7.7 \times 10^{-4} \text{ W/cm}^2\text{h}$ . When the aluminum is coated with Sn-Ag-Ti alloy, degradation rate is an order of magnitude less than the fuel cell assembled with nickel plated bipolar plate. Some increase in the cell resistance is observed but no breakthrough of resistance observed up to 3120<sup>th</sup> minute. Although Sn-Ag-Ti coating is more durable than nickel coating the cell resistance observed is

too much for a fuel cell. This coating might be a conversion coating since it has high bulk electrical conductivity and very high adherence to aluminum.

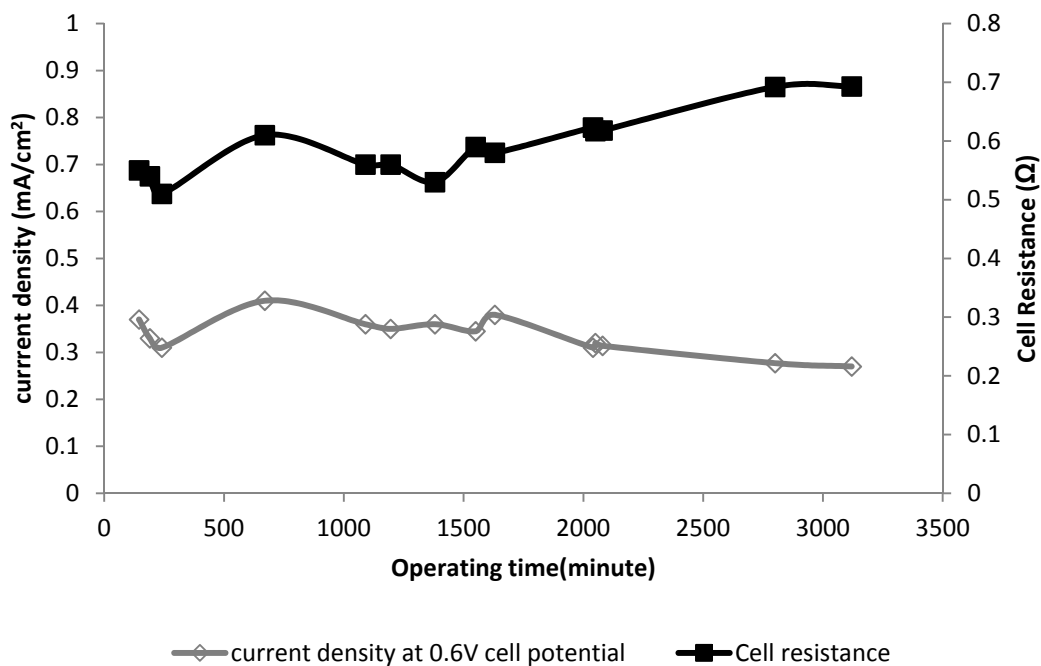


Figure 6.16 The change of current density at 0.6V cell potential and the cell resistance for Sn-Ag-Ti alloy coated single cell aluminum plates

### 6.3.3 Performance of graphite-PVDF composite coated bipolar plates

Aluminum fuel cell plates coated with graphite-PVDF composite paint was assembled with MEA prepared with 0.4mg Pt/cm<sup>2</sup> loaded MEA prepared with ultrasonic spraying technique. The polarization curve shown in Figure 6.17 was obtained. The maximum power observed is 0.2W/cm<sup>2</sup> which is the quarter of the

power density reached with graphite single cell plates. Cell resistance calculated from the slope of the linear region of the polarization curve is  $0.8\Omega$ .

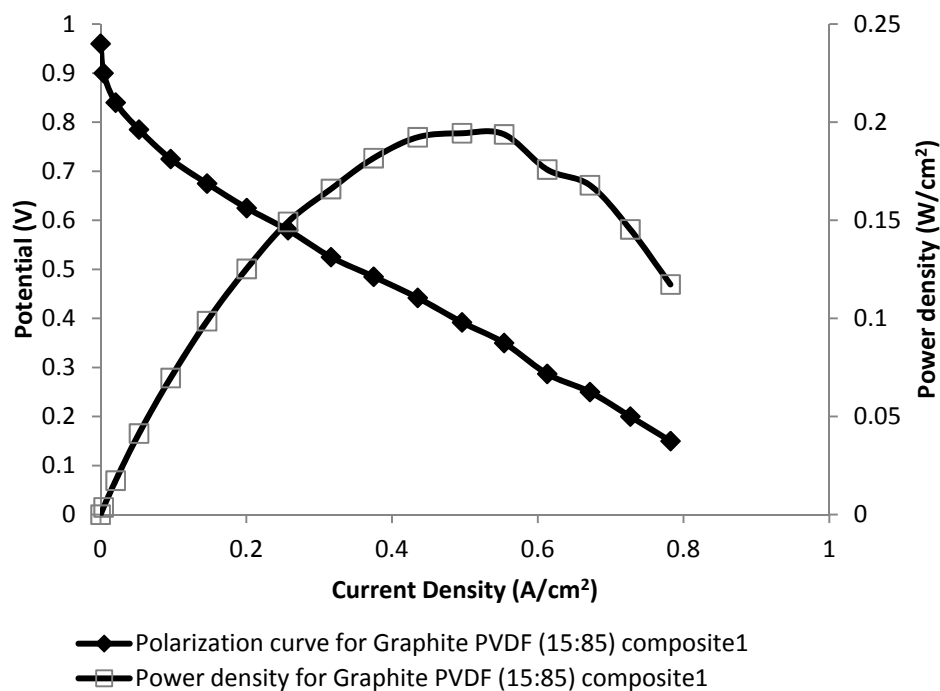


Figure 6.17 Polarization curves for graphite-PVDF (0.85:0.15) composite coated single cell aluminum plates

The impedances of the cell assembled with a GDL and graphite plates or graphite-PVDF composite coated plates is illustrated in Figure 6.18. The overall impedance at the contacts, bulk resistance of the GDL and the bulk bipolar plate material determines the current that can be obtained from the cell. The electrical ohmic resistances have a strong effect of the cell resistance which is measured as the linear region of the polarization curve of a fuel cell. The graphite plate has the lowest

impedance which is 0.014Ω. Graphite-PVDF composite coated plates have 0.077 Ω when there was no further processing. When the coating surface is polished or the coating is pressed at 160°C, the impedance reduces to 0.055Ω. The composition, processing, treatments may affect the resistance. Therefore, further study might be performed in order to observe better coating compositions or techniques. The importance of the contact resistance might be understood better if the Ohm's Law shown in Equation 6.5 is applied to the impedances measured experimentally. The current flow limited by Ohm's law can be calculated by Equation 6.6.

$$E = i \times R \quad (6.5)$$

$$i = \frac{E}{R} \quad (6.6)$$

The current that can flow from the cell at 0.5V potential difference becomes 7.14A/cm<sup>2</sup>, 1.3A/cm<sup>2</sup> and 1.82A/cm<sup>2</sup> for graphite, graphite-PVDF coated aluminum plate and polished or 160°C hot-pressed graphite-PVDF coated aluminum plates, respectively.

While Ohm's Law is a well known relationship, its use is limited to the ideal resistor. An ideal resistor has several simplifying properties. It obeys Ohm's Law at all current and voltage levels, its resistance is independent of frequency and AC current and voltage signals though resistors are in phase with each other. The real world contains circuit elements that exhibit much more complex behavior. The simple concept of resistance is abandoned by these elements. Impedance is used in its place, which is a more general circuit parameter. Like resistance, impedance is a measure of the ability of a circuit to resist the flow of electrical current. Unlike resistance, impedance is not limited by the simplifying properties listed above.

A signal with a known amplitude and frequency can be defined as in Equation 6.7.

$$I = I_{max} \sin(\omega t) \quad (6.7)$$

where,  $I_{max}$  is signal amplitude (A),  $\omega = 2\pi f$ ; f is frequency in Hz, t is time (s).

The corresponding response is given by Equation 6.8.

$$V = V_{max} \sin(\omega t - \varphi) \quad (6.8)$$

where,  $V_{max}$  is amplitude of the response and  $\varphi$  is phase angle.

Most of the circuit elements of real circuits are common electrical elements such as resistors, capacitors, and inductors. Table 6.1 lists the common circuit elements, the equation for their current versus voltage relationship, and their impedance.

Table 6.1 Common electrical elements

<b>Component</b>	<b>Current vs. Voltage</b>	<b>Impedance</b>
resistor	$E = IR$	$Z = R$
inductor	$E = L \, di/dt$	$Z = j\omega L$
capacitor	$I = C \, dE/dt$	$Z = 1/j\omega C$

The impedance of a resistor is independent of frequency and has only a real component. Because there is no imaginary impedance, the current through a resistor is always in phase with the voltage. The impedance of an inductor increases as frequency increases. Inductors have only an imaginary impedance component. As a result, an inductor's current is phase shifted 90 degrees with respect to the voltage. The impedance versus frequency behavior of a capacitor is opposite to that of an inductor. A capacitor's impedance decreases as the frequency is raised. Capacitors also have only an imaginary impedance component. The current through a capacitor is phase shifted -90 degrees with respect to the voltage.

The impedances of the cells assembled with a GDL shown in Figure 6.18 are agreed with the impedance vs. frequency behavior of the inductors. This behavior is interesting since two plates with separated with an insulator plate or a contact resistance should behave like a capacitor. The reason of this behavior might be because of the GDL in between two conductive plates. GDL is a material consists of arbitrary arrangement of carbon fibers as SEM image shown in Figure 2.1. These arbitrary arranged fibers might behave like an inductor. The magnetic fields in the GDL might cause back currents at higher frequencies like an inductor does.

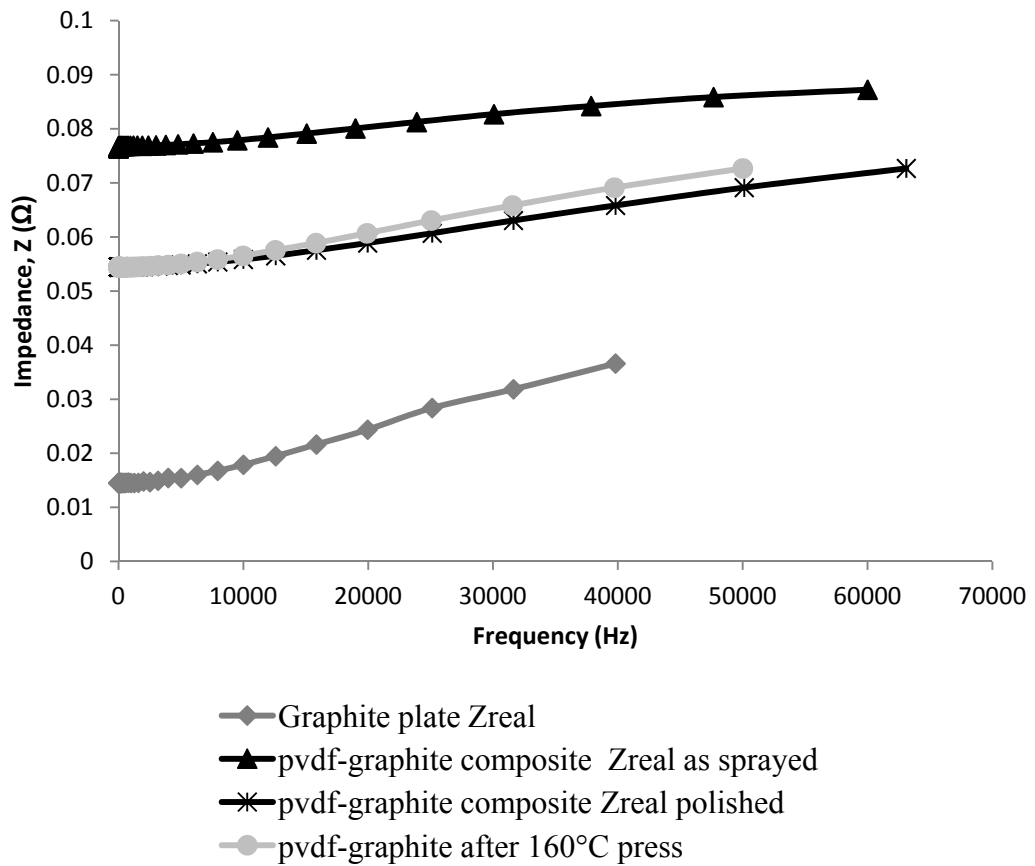


Figure 6.18 Impedances of the cell assembled with a GDL with graphite, graphite-PVDF composite as coated, graphite-PVDF composite as polished after spraying and graphite-PVDF composite as hot pressed at 160°C after spraying.

In this work both graphite and metallic (aluminum) bipolar plates have been studied. Aluminum bipolar plates have been coated with nickel, Sn-Ag-Ti alloy and graphite-PVDF composite coating. Nickel coating was not found to be durable in real fuel cell environment. The performance significantly dropped after 1645<sup>th</sup> minute of operation. When the operation time was 2425<sup>th</sup> minute, about no useful current density remained. Sn-Ag-Ti ternary alloy used for aluminum soldering was coated to the active area surface. The durability of this coating was much better than nickel

plating. The cell was operated more than 3100 min and no abrupt decrease in performance was observed. The maximum power density with Sn-Ag-Ti coating was  $0.28\text{W}/\text{cm}^2$  and the remaining power density at 3120<sup>th</sup> minute was  $0.22\text{W}/\text{cm}^2$ . The power density observed with PVDF-graphite composite coating on the surface of the active area was  $0.2\text{W}/\text{cm}^2$ . The reason of this low power density was because of the resistance of the film layer. The resistance measured with the PVDF-graphite coated plates was 4-5 times higher than the resistance measured with graphite plates. Therefore for the final design graphite bipolar plates has been manufactured by CNC machining technique.

## **6.4 Results of PEMFC Prototype Stack**

### **6.4.1 Performance of Prototype Stack 1**

Prototype Stack 1 was assembled with 20 cells, 20 MEAs and 40 gaskets and tested with test station as shown in Figure 4.12 a, b and c in order to determine the characteristics of the stack. The stack temperature was kept at  $60^\circ\text{C}$  during the test. The cell voltage distribution results obtained during the tests are given in Figure 6.19. Most of the cells have around 1.1V open circuit voltage (OCV). Whereas, four cells which are the first, second, third and twentieth cells have lower OCVs than the other cells. Especially the third cell has an OCV of 0.84V which is very low. Some voltage drop was observed as expected when the stack was connected to the external electrical load. When the cell voltage becomes 14V the average voltage of the cells are 0.7V since there are 20 cells in the stack. At 14V stack potential, the first, second, third and twentieth cells have lower voltage than 0.7V. When the stack voltage is 12V, that is the average cell voltage is 0.6V, the third cell potential is 0.36V or nearly the half of the average cell voltage. The first, second, third and

twentieth cells, which have lower OCVs, are observed to have lower potentials than the average cell voltages.

The polarization curve for the stack which shows the decrease of total stack voltage for increase in the stack current is shown in Figure 6.20. Due to the low performance of the first, second, third and twentieth cells, the total current which can be withdrawn from the stack was decreased. Although the stack was designed to operate at 110W; it operates at 60W as illustrated in Figure 6.20.

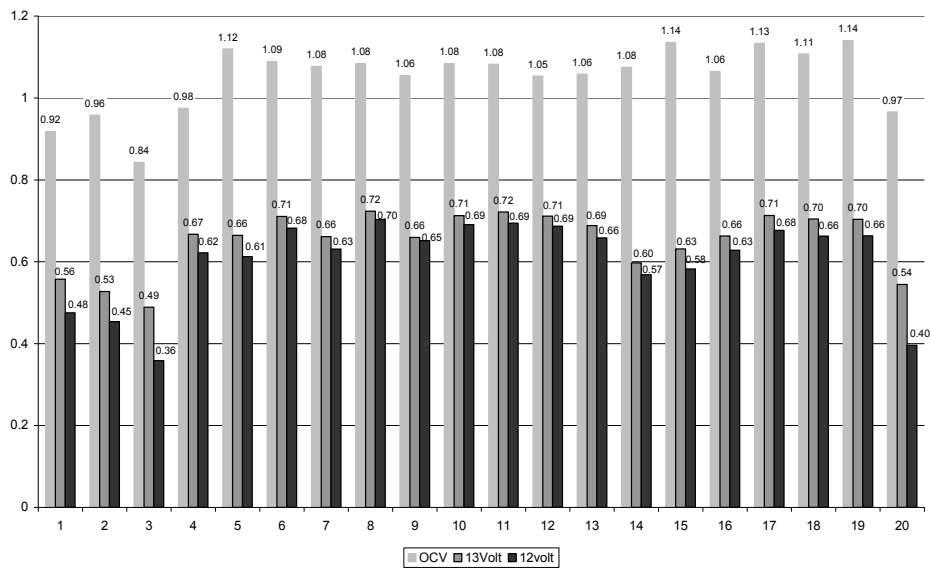


Figure 6.19 Cell voltage distribution

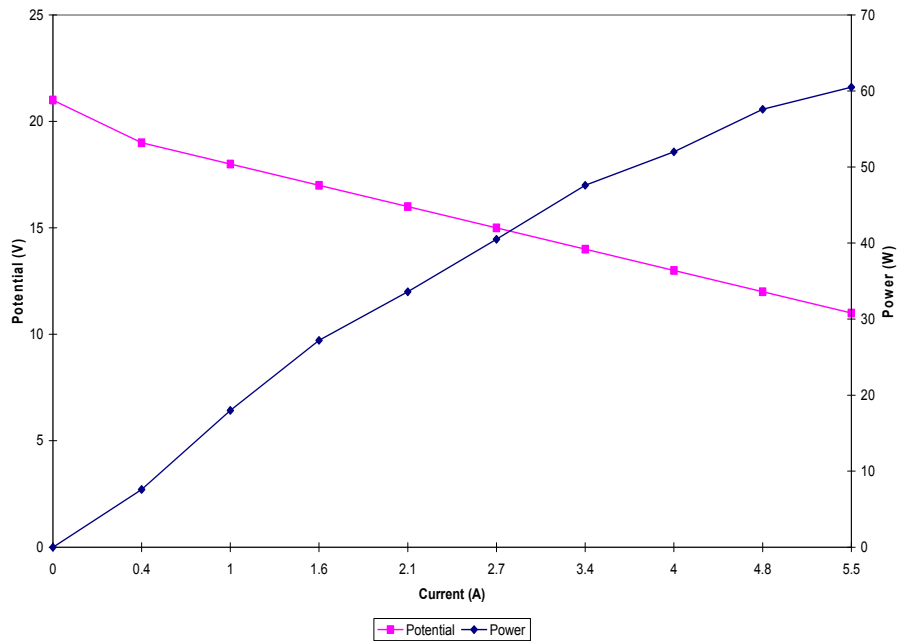


Figure 6.20 Polarization curve for the tested stack

It was shown that some of the cells did not operate properly. A similar non-uniform distribution pattern is observed by Scholta et. al. [44]. It is found that the voltage distribution of cell voltages for 14 cell stack at a current density of  $600 \text{ mA/cm}^2$ , the average cell voltage is  $569 \text{ mV}$  at a standard deviation of  $35 \text{ mV}$ . The cell voltages have a small increasing trend in increasing cell number. The reason of this phenomenon is attributed inhomogeneous cell humidification within the stack.

Giddey et.al. [45] designed and tested  $1 \text{ kW}$  stack with 15 cells. They reported the individual cell voltages of the stack. Although the voltages of the stack are not uniform, there is no relation for the low voltages with the cell numbers. Fourth, eleventh and thirteenth cells have lower potential than the others.

An air cooled 21 cell stack for portable applications was investigated by Sohn et.al [46]. It is reported that the cell voltages of 2 or 3 cells which are opposite the manifold inlet appears nearly 20% lower than the average cell potential. They have considered the cell potentials in acceptable uniformity and did not suggest a reason for this issue.

The gasket thickness could be adjusted with this approach. However, a sealing problem was appeared with this gasket design. Some shortcut was observed around the manifolds which caused performance loss and small explosions in the stack, and MEAs were damaged. A new cell design was considered as a solution and improvement to the problems noticed with the previous cell and stack design.

#### 6.4.2 Performance of Prototype Stack 2

The designed parts were produced by graphite as described in Figure 4.5 and assembled as shown in Figure 6.21. The assembled stack was tested in the test station with hydrogen at anode and air at cathode. The stoichiometric ratios of the gases fed to the anode and cathode were 1.2 and 2.5, respectively. Both gasses were fully humidified to 100%RH prior to feed to the fuel cell stack.

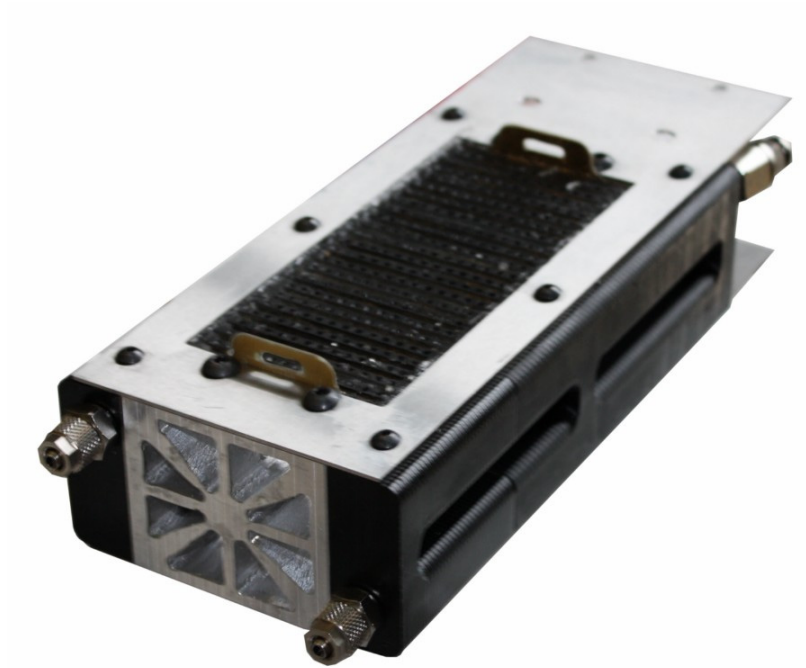


Figure 6.21 Manufactured and assembled fuel cell stack

The polarization curve obtained from the testing of the stack is shown in Figure 6.22. More than the desired fuel cell stack power is reached. The current density reached is 12.9A at 12 V stack potential and the corresponding power is 155W. This power is enough for parasitic losses such as compressor, pump, and electronic control and the required net 100W power output. The stack resistance is calculated from the linear part of the polarization curve is 0.63 $\Omega$ .

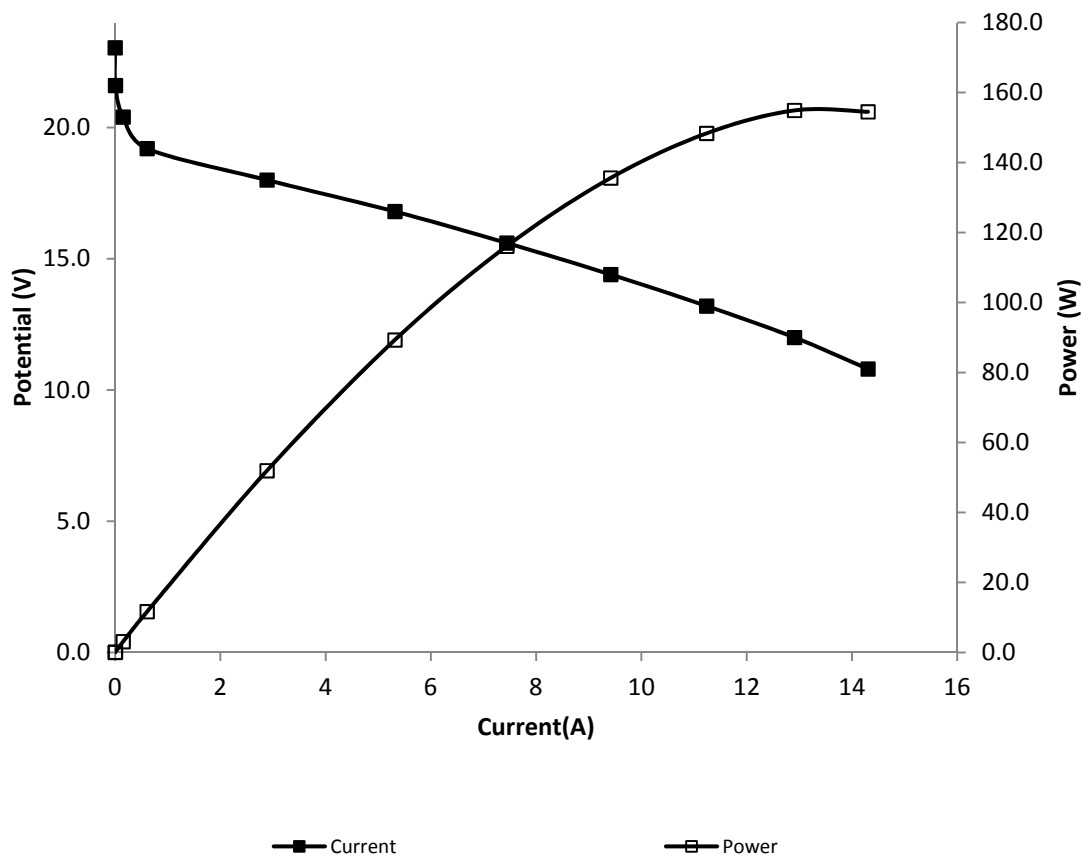


Figure 6.22 Polarization curve obtained from the fourth fuel cell stack design

A fuel stack development requires many tasks in order obtain a working high power density stack. The design, component development and manufacturing require high precision. The Membrane electrode assemblies developed during the study enabled a high power density stack. The comparison of the performances of the present study with the published performance results of the hydrogen-air PEMFC short stacks and stacks is given in Table 6.2. The performances reached in the present study are in accordance with the performance results published in the literature.

Table 6.2 Comparison of the published performance results of the hydrogen-air PEMFC short stacks and stacks

Stack Power (W)	Number of Cells	Active Area (cm <sup>2</sup> )	Power density (mW/cm <sup>2</sup> )	Oxidant	Cathode Backpressure (Barg)	Reference	Year
12 to 150	6 to 30	19 to 60	57 to 150	Air	0	[47]	2001
1011	15	225	300	Air	1.7	[45]	2004
14000	72	560	250	Air	0	[44]	2004
50.4	6	94.3	630	Air	0	[48]	2004
600	21	100	280	Air	0	[46]	2005
1.75	7	5	53	Air	0	[49]	2006
6	6	33	328	Air	0	[50]	2006
20	10	25	80	Air	0	[51]	2007
220	4	100	550	Air	0	[52]	2007
11	5	14	157	Air	0	[53]	2010
						Present	
50	20	12.25	250	Air	0	Study	2010
						Prototype 1	
						Present	
155	24	23	280	Air	0	Study	2011
						Prototype 2	

The developed stack during this study can be used for a portable 100W net power output system. The long term performance evaluation and durability of the developed stack is not performed within the scope of the thesis. The durability tests including long term static load, load cycling, and start-up and shut down tests must be performed in order to use the developed stack in an application.

## CHAPTER 7

### SYSTEM DESIGN AND AUXILIARIES

The proposed fuel cell system and the instrumentation list is shown in Figure 7.1 and Table 7.1, respectively. It includes a  $\text{NaBH}_4$  hydrogen generator (R1), a micro compressor (C1) to supply air to the cathode of PEM fuel cell stack, a membrane type heat and humidity exchanger (HHEX), a cooling blower (B1) and an electronic control unit (PLC1). Hydrogen is produced at the  $\text{NaBH}_4$  hydrolysis reactor as it is desired. A pressure regulator reduces and regulates the hydrogen pressure to 3-4psi. A normally closed solenoid valve controls if hydrogen will be supplied to the system. Hydrogen is directly fed to the anode of the PEM fuel cell stack. A solenoid valve opens if a purging command is sent from the controller. The cathode stream is the air which is supplied from the atmosphere. An air filter (F1) is required to clean the ambient air. The air is compressed to overcome the pressure drop in the humidifier and stack and supply the necessary air flow to the system. Air is supplied with a micro air compressor (Hargraves, USA). The cold and dry air passes through the heat and humidity exchanger and enters into the fuel cell stack's cathode side. As the reaction takes place, heat and water are generated. The exhaust air is nitrogen rich since oxygen is consumed during the reaction and it contains liquid and vapor water at the operating temperature of the stack, it leaves the cathode and enters the wet and hot stream side of the heat and humidity exchanger. The heat and water are transferred through the membrane in the heat and humidity exchanger. It loses some of its energy and water and leaves the humidifier as gaseous and liquid phase.

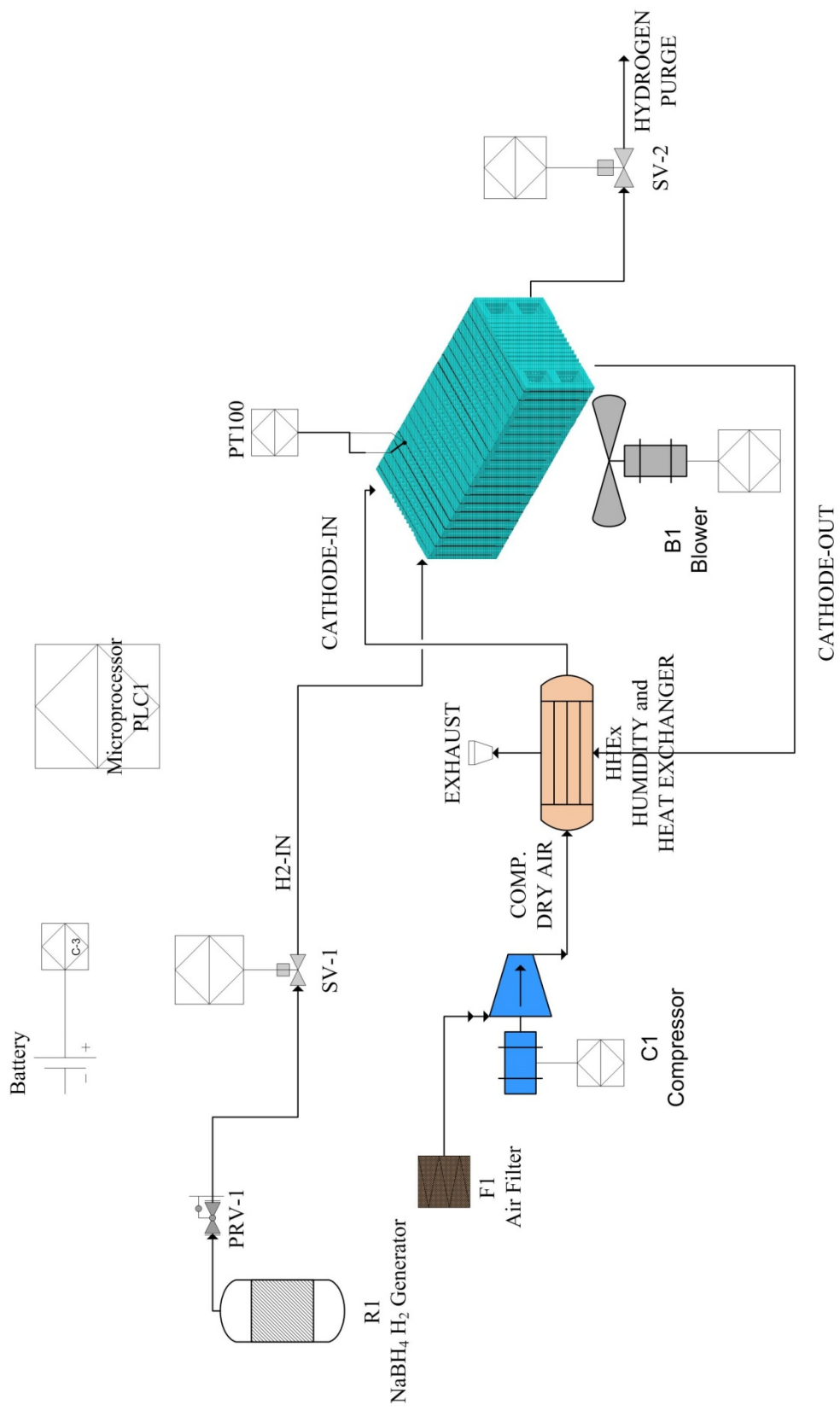


Figure 7.1 The flow sheet of the 100W Portable PEM Fuel Cell System

Table 7.1 Instrumentation list for the PEM fuel cell system

Equipment code	Description
R1	Sodium borohydride hydrolysis reactor
PRV-1	Pressure reducing valve for regulating the hydrogen feed to the fuel cell stack at 3-4 psig.
SV-1	Solenoid valve for controlling hydrogen feed
SV-2	Solenoid valve for controlling hydrogen purge
C1	Micro air compressor capable of 11 spm air
B1	Blower for coolant air supply
HHEX	Heat and humidity exchanger
PLC1	System controller, programmable logic controller
PT100	Temperature sensor

The temperature of the stack must be controlled. Since it is an air cooled stack, a controlled blower fan is required. In order to measure the stack's actual temperature a temperature sensor (PT100) is used.

Fuel cells require a system which handles the reactant supply, reactant conditioning, excess reactants and product exhaust, temperature control. These controls are listed below.

- i. *NaBH<sub>4</sub> reactor*: Hydrogen generation rate must be controlled in order to supply on demand hydrogen to fuel cell stack
- ii. *Hydrogen supply (supply on/off and purge)*: When the fuel cell stack is started by the system controller, the hydrogen supply to the fuel cell stack

should be permitted by controlling a solenoid valve. For a dead-end operation the hydrogen must be purged according to a specified purge cell voltage.

- iii. *Air supply (flow rate)*: The air fed to the stack must be calculated according the current generated by fuel cell stack.
- iv. *Stack temperature*: It must be kept constant at a defined temperature.
- v. *Room temperature*: Might be monitored in order to allow stack to be operated or not.
- vi. *Battery voltage and charge management*: Start up energy comes from a battery pack. Therefore, its condition must be controlled.
- vii. *Cell voltage state*: Cell voltage must be monitored in order to save the cells from being damaged due to very low voltage or cell potential reversal.
- viii. *Cooling fan management*: Cooling fan speed must be controlled in order to keep the stack temperature constant.
- ix. *Start up - shut down management*: A programmed start-up and shut down script must be performed by the controller
- x. *Power output enable/disable*: The power output must be opened only when the fuel cell system is available to deliver power.

Among the various available process options anode dead-end and cathode open flow system was selected. The major advantage of anode dead-end mode is the efficient use of hydrogen in other words high fuel efficiency. In this mode hydrogen supplied to the anode as a dry gas at 3-4 psig and let the fuel cell system to consume hydrogen as current drawn from the fuel cell stack. Therefore, the use of hydrogen flow controller becomes unnecessary. Moreover, the hydrogen is not continuously exhausted. The disadvantage of dead-end mode is that the supplied hydrogen must be pure. Even the inert gases cannot be tolerated for the proper operation when high current or power conditions required. The water molecules or nitrogen coming from cathode is also accumulated on the anode during the normal operation. The rate of accumulation of inert molecules increases with the increase of current produced by the stack. The increase in the accumulation of inert gas at anode reduces the partial

pressure of hydrogen at the cathode. The decrease of the partial pressure of hydrogen is observed firstly at the cell which is most far to the hydrogen feed. The reduced hydrogen partial pressure results cell voltage decrease compared to the average cell potential. When an allowed cell voltage decrease measured, a hydrogen purge is allowed to the atmosphere for short period of time. Therefore, the anode is cleaned from the inert molecules and cell potential is recovered to the average cell potential state.

The cathode side works simply in open flow configuration. A micro air compressor supplies necessary air to the system. The air is humidified with a humidifier. The source of the heat and water is supplied from the exhaust of cathode. The humidified and heated air is fed to the cathode of the stack.

## **7.1 Controller Selection**

There are some alternative controllers for controlling such a system. These controllers may be constructed from programmable logic controllers (PLCs), microcontroller units (MCU) with custom designs and Cubloc. Among these PLCs and MCUs are well known and widely used ones. They have some advantages and disadvantages.

The advantages of PLCs are their low cost, easy programmability (via Ladder logic), and extremely reliability. However their disadvantages are that they require many modules for AI/AO and they are too large for such a portable system.

Microcontroller units (such as PIC) based custom circuits can also be used as a system controller. The advantage of MCU is their very low cost. The disadvantages of MCU are that they are not reliable, programming is not simple as PLC (ladder logic), and they require electronic design which is not within the scope of this work.

Another controller alternative is not a well known but very advantageous controller Cubloc with its base board. The advantages of Cubloc are that their cost is low, their programming is very easy and does not require compiler, basic and ladder logic program works simultaneously, they can process complex math easily, they are reliable, and they have a base board which includes many input output features. The disadvantage of Cubloc is that Ladder library is not as rich as a PLC.

The picture of the Cubase 32M board is shown in Figure 7.2.



Figure 7.2 Image of Cubloc Cubase 32M board to be used in system controller

The technical specifications of Cubloc with its base board Cubase 32M is shown in Table 7.2.

Table 7.2 Technical specifications of Cubloc with Cubase32M

Model	CUBASE-32M
Processor	CB280
Program Memory (Flash)	80KB
Data Memory (RAM)	2KB(BASIC)+1KB(Ladder Logic)
EEPROM	4KB
BASIC Execution Speed	36,000/sec
Ladder Scan Time	10ms (Turbo-mode: ~100µsec)
Serial Ports for Communication	- 2 High-speed hardware independent serial ports (Channel 0 & 1: RS232C 12V) - Configurable Baud rates: 2400 to 230,400 bps
Digital Inputs	16 Opto-Isolated 5 to 24V
Digital Outputs	12 Opto-Isolated 12 or 24V NPN TR
Analog Inputs	6 Channel 10-bit ADCs Configurable Input Voltage: 0 to 5V
Analog Outputs	6 Channels 16-bit PWMs Configurable Modes: PWM or DAC(0 to 5V)
Counters	2 Channel 16-bit High Speed Counters for 7.5 to 24V DC Pulse Input (up to 2Mhz)
Timer	1 Configurable Timer, Configurable Interval = 10ms
Power	Required Power: DC 12 to 28V Current Consumption w/ ports unloaded: @ 24VDC: 20mA

Figure 7.3 illustrates the schematic representation of the inputs and outputs of the Cubloc system. Cubloc has opto-isolated 16 outputs and 12 inputs. These I/Os will be used to control many features. It also contains 6 analog inputs to measure various sensors and 6 analog outputs which allow PWM control for motor (fan, compressor, pump etc.) speeds. Multiplexers are devices used for switching many analog inputs to single analog input. They can be controlled with some digital output ports. For example with three digital outputs  $2^3=8$  different input can be directed to a single input with a scanning time of less than 1 ms. Multiplexers allow scanning of inputs at nanosecond time.

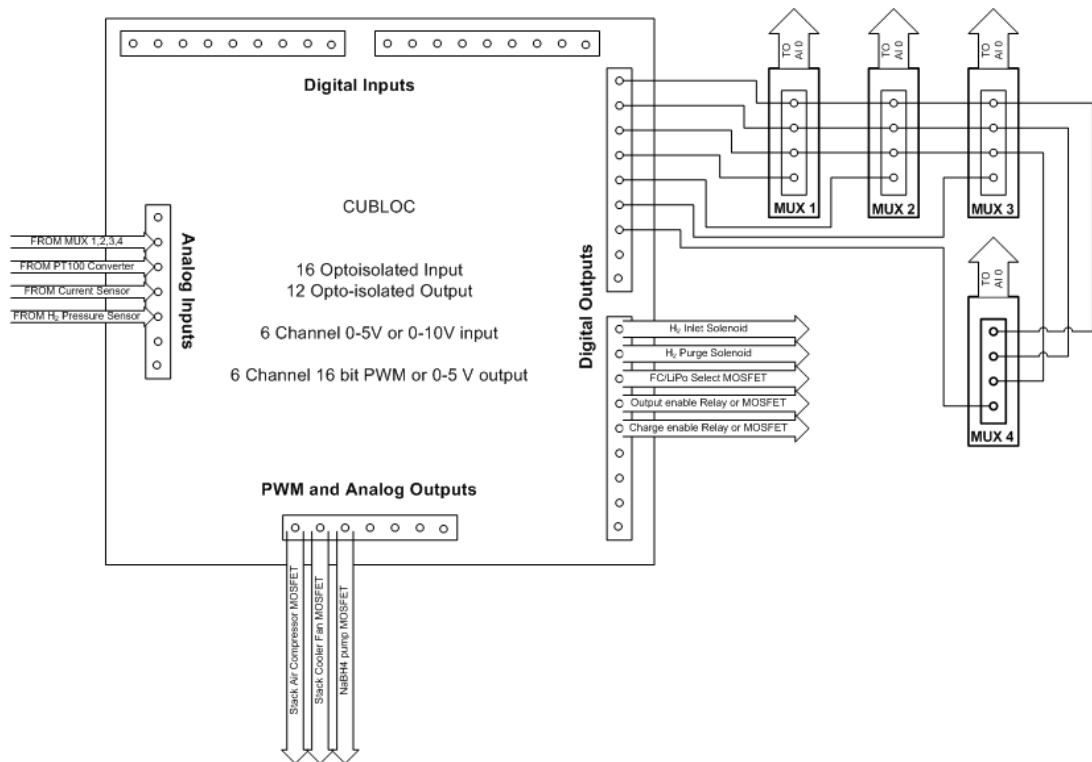


Figure 7.3 Schematic diagram of Cubloc input outputs (I/Os)

## 7.2 Control Peripheral Cards

Cubloc alone is not sufficient for the control of the system. The auxiliaries such as air supply compressor, cooling fan, solenoid valves, cell voltage monitor, current sensor, temperature sensor, and pressure sensor require interface cards in order to operate and communicate with main controller “Cubloc”. Two interface cards are designed and manufactured within the scope of this study. First card is directly connected to the Cubloc via their connectors and its main duty is the power management, pump, compressor, and fan drive. This card also has necessary drive circuit for multiplexer card which is the second card of the system that is designed and manufactured.

### 7.2.1 Power management and peripheral driver card

The power management and peripheral driver card is designed in a way that it can be directly connected to Cubloc’s digital and analog input and output ports. The connectors that are used for interfacing driver board with Cubloc is shown in Figure 7.4. J13 is the connector that supplies Cubloc’s power. J15 is connected to a switch that is a user interface for starting and stopping the system. J16 is an interface for the digital inputs of the Cubloc which transports start/stop signal and pressure sensor digital information. The necessary 5V power comes from Cubloc via J9 which is connected to CUNET connector. J10 and J11 is the connector for the digital outputs of the Cubloc. Multiplexer digital signals, battery pack charging enable or disable, H<sub>2</sub> supply and purge solenoid signals, and output power enable or disable control signals are interfaced via these connectors. The pulse width modulation (PWM) signals for NaBH<sub>4</sub> circulation pump, air compressor, and cooling blower fan are interfaced with J12. The analog input connector of the Cubloc is connected with J2 which sends cell voltage monitor (CVM), battery voltage, temperature reading voltage, H<sub>2</sub> pressure reading voltage, and current reading voltage. J17 is an interface with the pressure sensor and switch.

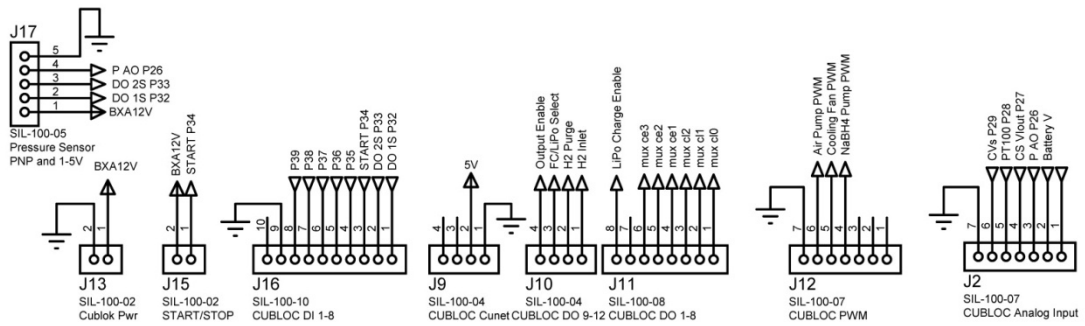


Figure 7.4 The connectors of the peripheral card that is interfaced with Cubloc

The peripheral driver board consists of many functional blocks. Power handling and current sensor block design is given in Figure 7.5. There are two power input for the card or entire system. First power input comes from J4 which is connected to a lithium polymer (LiPo) battery pack. The current from battery pack flows through Q14 which is in a normally on configuration. Q3 keeps Q14 in on position if the voltage on the gate (2<sup>nd</sup> pin) is low (0V). If FC/LiPo select pin is made high (+12V) from the program running in the Cubloc, Q3 drains the potential on the gate of the Q14 and it turns to off state. Meanwhile, the gate of Q15 becomes high and starts to allow current coming from fuel cell stack to the control system. The power entering to the system, regardless of the source, enters into a 30W DC-DC converter (Artesyn, BXA 12D12). The DC-DC converter regulates the 9-18V to a stable 12V output which powers controller, compressor, pump, fan, pressure sensor, and solenoid fans. A variable resistor, RV1, is used for adjusting the output voltage of the DC-DC converter. The fuel cell stack power is connected to system with J8. It is connected to a current sensor (Allegro, ACS755XCB-050) capable of measuring -50 to 50A current with analog output of 0 to 5V where 2.5V corresponds to 0A and 5V corresponds to 50A. When the system ready to supply the necessary power to user “Output Enable” pin is made high and the power of the fuel cell stack is supplied to the user.

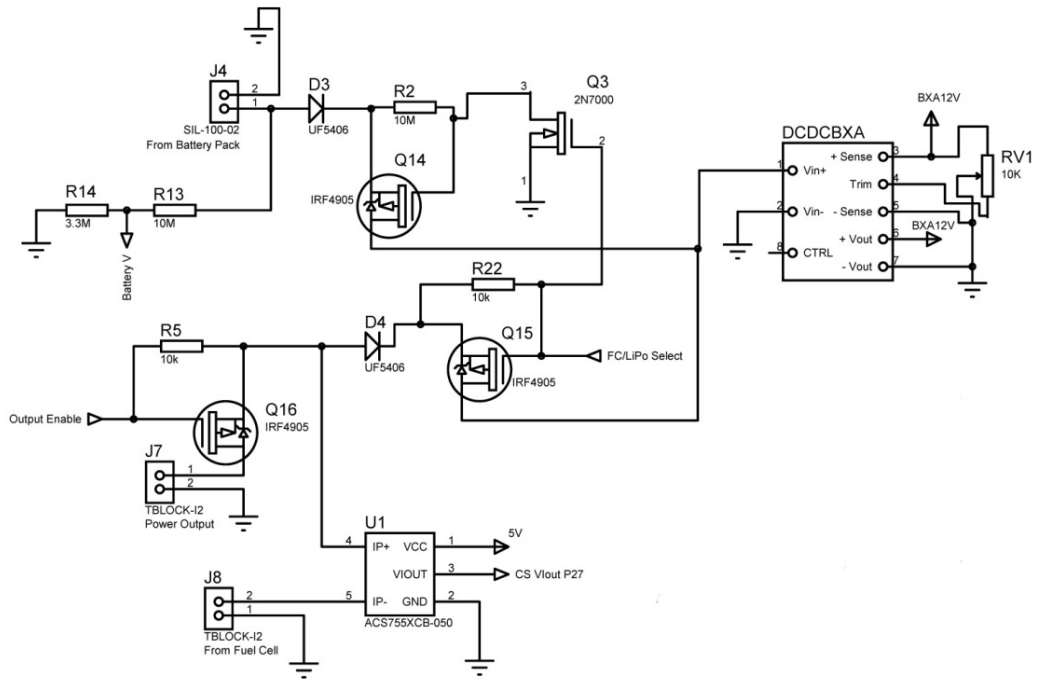


Figure 7.5 Power handling and current sensor block

Pulse width modulation (PWM) is a convenient method for power control or motor speed control. In this method, the output is modulated between 0 to 100% duty by changing the on-off period with high frequency. PWM signal coupled with a metal-oxide-semiconductor field-effect transistor (MOSFET) which is capable of switching at high frequencies can control the speed of DC motors. The MOSFET drivers designed for controlling NaBH<sub>4</sub> pump, air compressor and cooling blower fan is shown in Figure 7.6. PWM signals generated by Cubloc are connected to the gates of the Q4, Q5 and Q6. The 10K resistors connected between the gate and source of the MOSFET are used for draining the charge formed on the gate when the input signal is low. The compressor, pump and blower fans are directly connected to J1, J5 and J6, respectively.

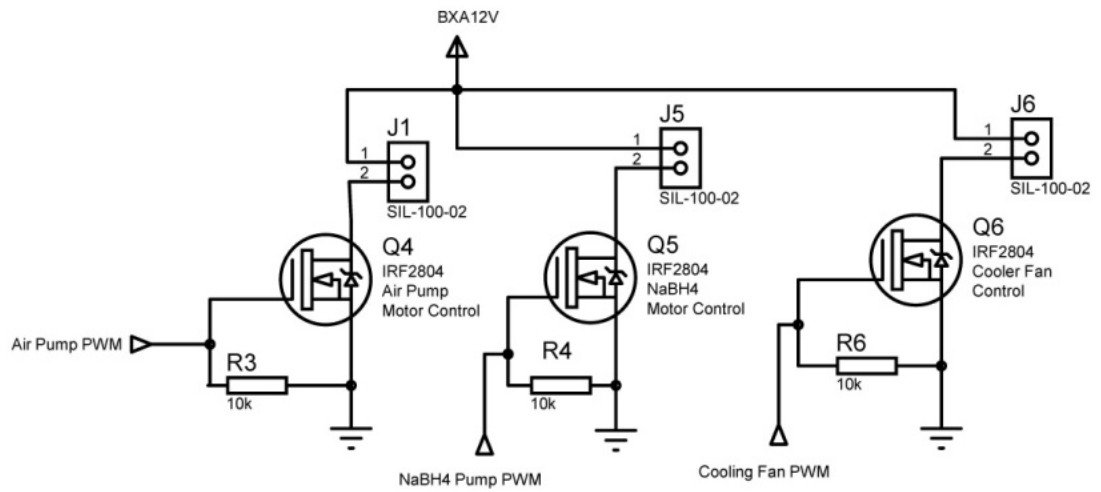


Figure 7.6 Pulse width modulation (PWM) driver block

The driver block for solenoid valves and enabling battery charging is given in Figure 7.7. The operation principle is similar to PWM drivers, but the switching is not duty controlled. The switch is on or off according to the status of the digital output of the Cubloc. H2 inlet valve, H2 purge valve and lithium polymer battery pack charger module are connected to J20, J21 and J22, respectively.

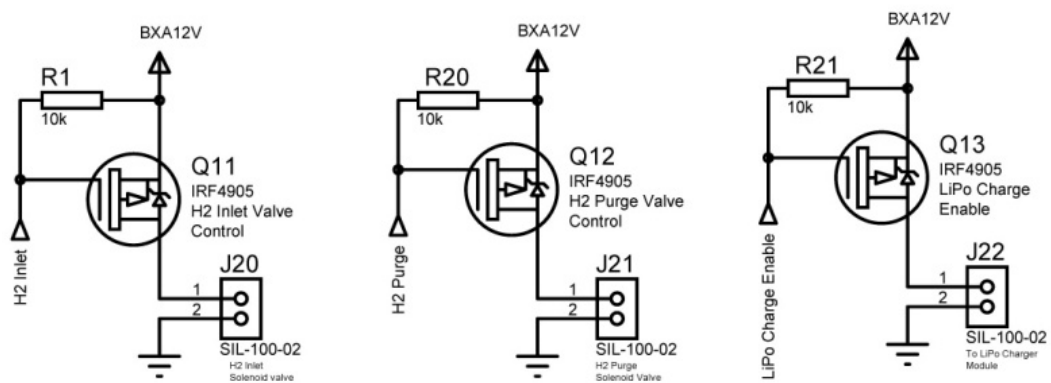


Figure 7.7 Valve and battery charging enable driver block

Multiplexers are used for fast switching of multiple analog input signals to a single analog input channel. Six digital signals are required for controlling three multiplexer integrated circuits (ICs) having 8 dual channel inputs. Three of them is required for switching the channels ( $2^3=8$  combinations) and three of them is enabling or disabling the individual multiplexer chips. The digital signals necessary for driving multiplexing board is produced with the Cubloc's digital signals with the circuit block illustrated in Figure 7.8.

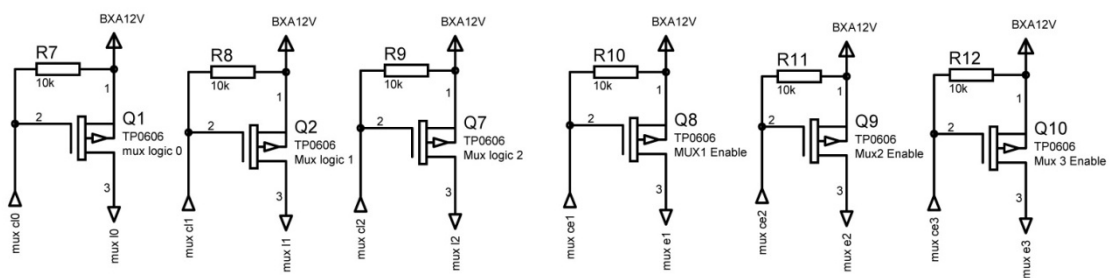


Figure 7.8 Multiplexer logic signal driver block

Connector “J3” is used for interfacing driver board with multiplexer board which is located on the stack. The pin-out diagram of the connector is shown in Figure 7.9.

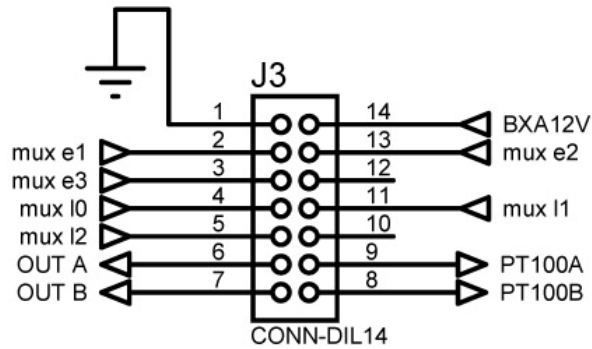


Figure 7.9 The pin-out of the multiplexer card interface.

The temperature of the stack is measured with a temperature sensor called “PT100” which is a platinum resistance sensor. The resistance of the sensor increases with increasing temperature. Although it is possible to read the sensor data with a simple constant current circuit, it is safer and much easier to use a PT100 converter module (Sunyuan, ISO Z1-W2-P2-O4). The schematic for the temperature sensor reading to voltage converter block is shown in Figure 7.10. The module gets the sensor input, and converts the 0-100°C temperature data to 0-5V output signal. RV3 and RV4 are used for zero and span adjustment, respectively.

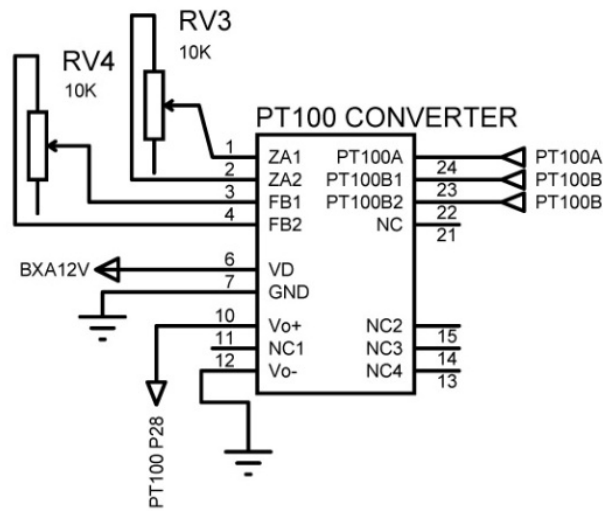


Figure 7.10 Temperature sensor reading to voltage converter block (PT100 converter block)

The fuel cell stack designed and manufactured has a potential of up to 22V. That means the most positive cells anode has 21.1 and cathode has 22V with respect to most negative anode of the stack. The Cubloc or any controller has up to 5V analog input. For that reason, the input potential must be conditioned while reading by the analog input of the controller. The circuit designed for the solution of the problem is given in Figure 7.11. For measuring any cell voltage, an analog isolator (Sunyuan, ISO-U1-P2-O4) is connected to the output of the multiplexers. The output of the module is directly connected to the analog input of Cubloc. RV2 is used for calibration of the input and output signal.

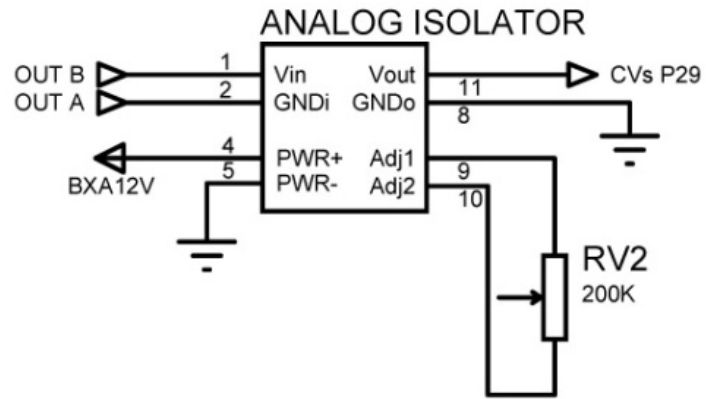


Figure 7.11 Analog isolator used for isolation of cell voltage monitor readings

The images of the designed and manufactured peripheral driver card connected to Cubloc controller is shown in Figure 7.12.

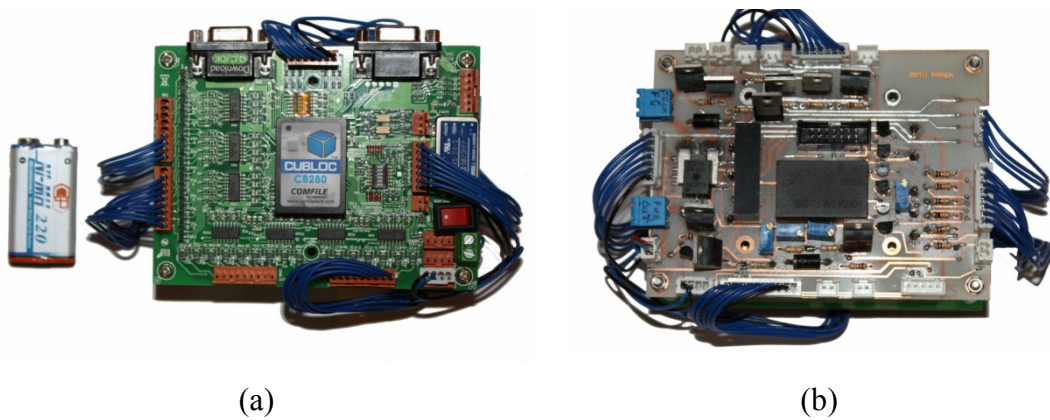


Figure 7.12 The photographs of completed fuel cell system controller a) Cubloc controller side b) power management and peripheral driver card side

## 7.2.2 Cell voltage monitor multiplexer card

Cell voltage monitor is designed by using DG407 multiplexer chips. 24 cell voltages can be monitored with 3 multiplexers with 6 digital outputs and an analog input of Cubloc. The cell voltages are measured from the cells with spring probes.

The schematic diagram of the multiplexer circuit is given in Figure 7.13. U1, U2 and U3 are DG 507 differential 8-Channel, CMOS analog multiplexer chips. The logic inputs define which input pair is routed to output. The logic and output relation is illustrated in Table 7.3.

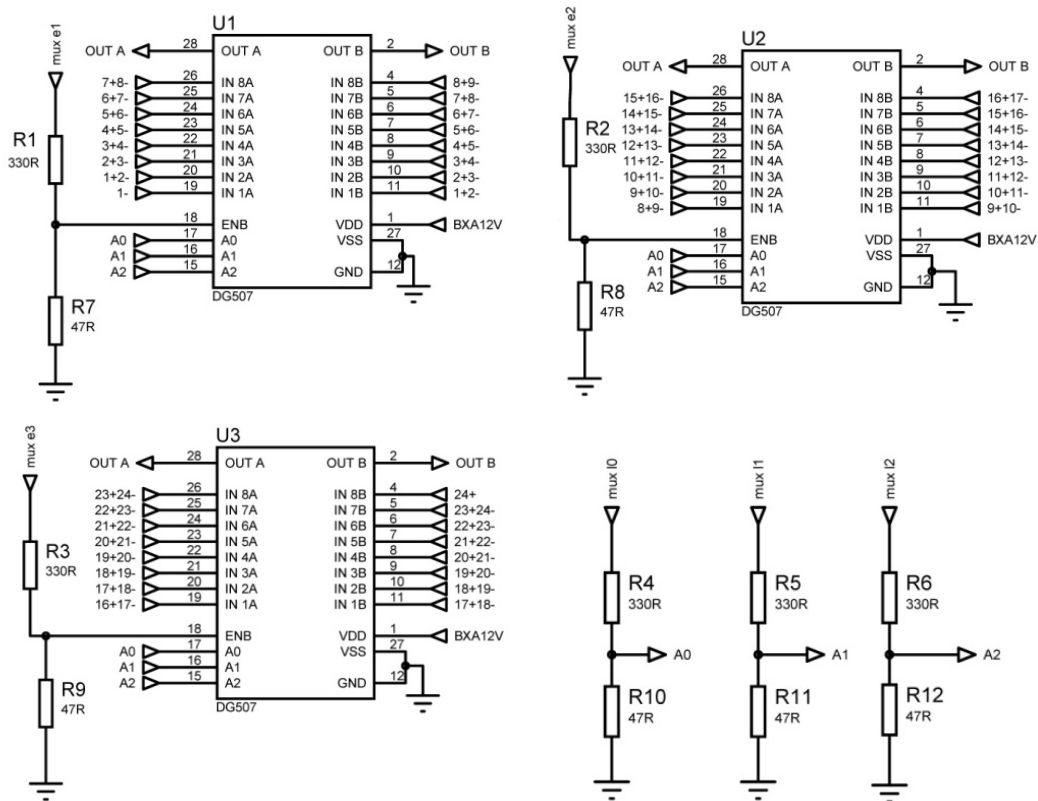


Figure 7.13 The schematics of multiplexer circuit

Table 7.3 Switch pair output relation according to the logic status

A2	A1	A0	EN	ON SWITCH PAIR
X	X	X	0	None
0	0	0	1	1
0	0	1	1	2
0	1	0	1	3
0	1	1	1	4
1	0	0	1	5
1	0	1	1	6
1	1	0	1	7
1	1	1	1	8

The spring pin connections are shown in Figure 7.14. J1 is connected to the most negative cell's anode and J25 is connected to the most positive cell's cathode. The connections of the pins with the multiplexer is numbered as 1-, 1+2-, 2+3-, ..., 23+24-, 24+.

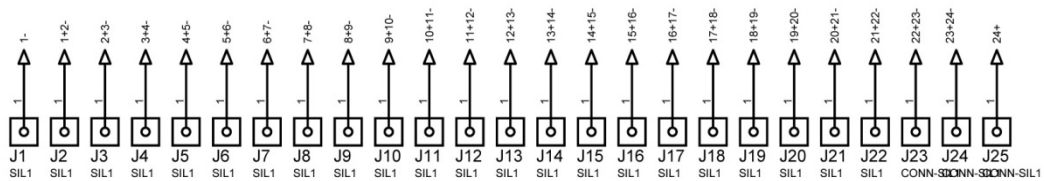


Figure 7.14 Schematic view of spring pin connections

Figure 7.15 illustrates the pin-out of the connector between the cell voltage monitor card and peripheral driver card. J26 is the connector for PT100 sensor which is used for stack temperature measurement. The designed circuit is mounted to the stack itself. Figure 7.16 shows designed CVM multiplexer card.

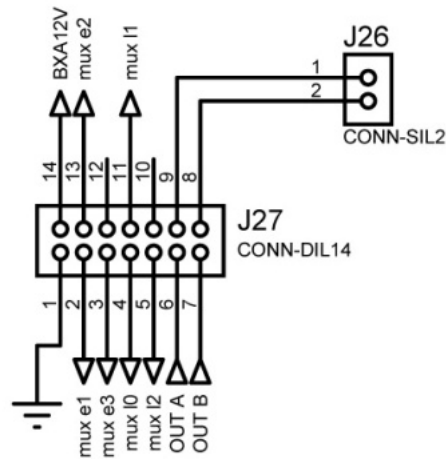


Figure 7.15 Interface connector with the peripheral driver board

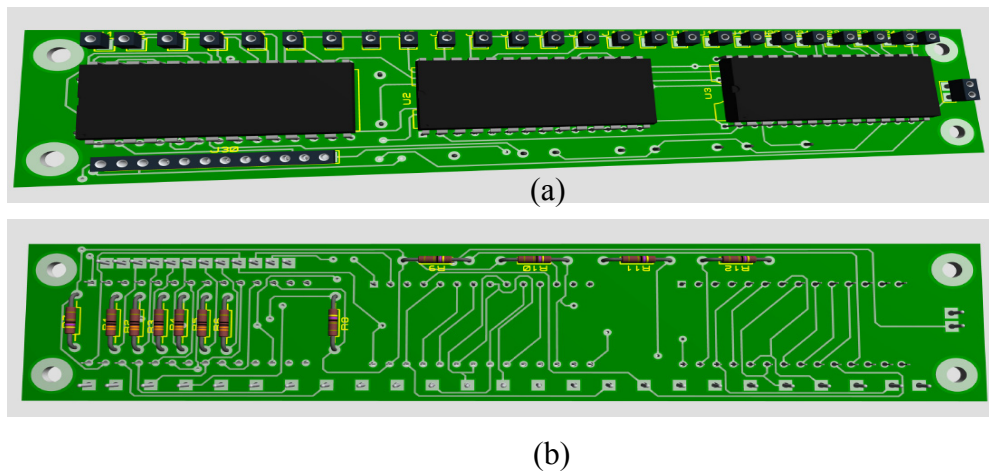


Figure 7.16 Cell voltage monitor multiplexer card a) Front view b) Back view

The image of the designed and manufactured cell voltage monitor card is shown in Figure 7.17.

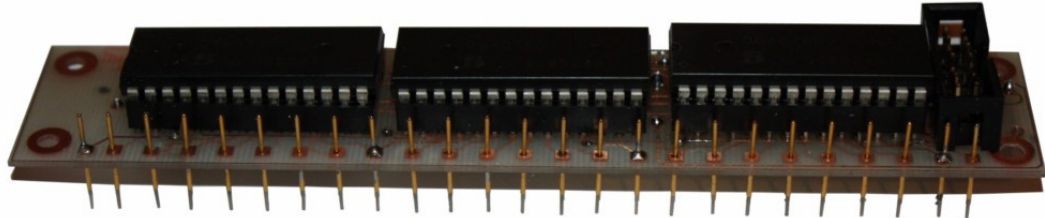


Figure 7.17 The photograph of the manufactured cell voltage monitor card

### 7.3 Air Supply System

Air supply system consists of a micro air compressor (Hargraves, USA), the stack current sensor, a MOSFET system to change the rpm of the compressor motor and a small filter. The sensor input voltage is calculated to the corresponding current data in the Cubloc. The necessary amount of air flow is calculated considering the set stoichiometric ratio for the air and the actual current data. Cubloc sends PWM signal to the MOSFET driver card. The rpm of the compressor motor is adjusted to supply the calculated amount of air to the system. The input variable is the current generated by the stack, the controlled variable is the flow rate of the air, and the manipulated variable is the rpm of the compressor motor. The relation between the compressor motor rpm and flow rate of the air is open-loop controlled since there is no sensor for the actual air flow rate. The schematic representation of the air supply system is shown in Figure 7.18.

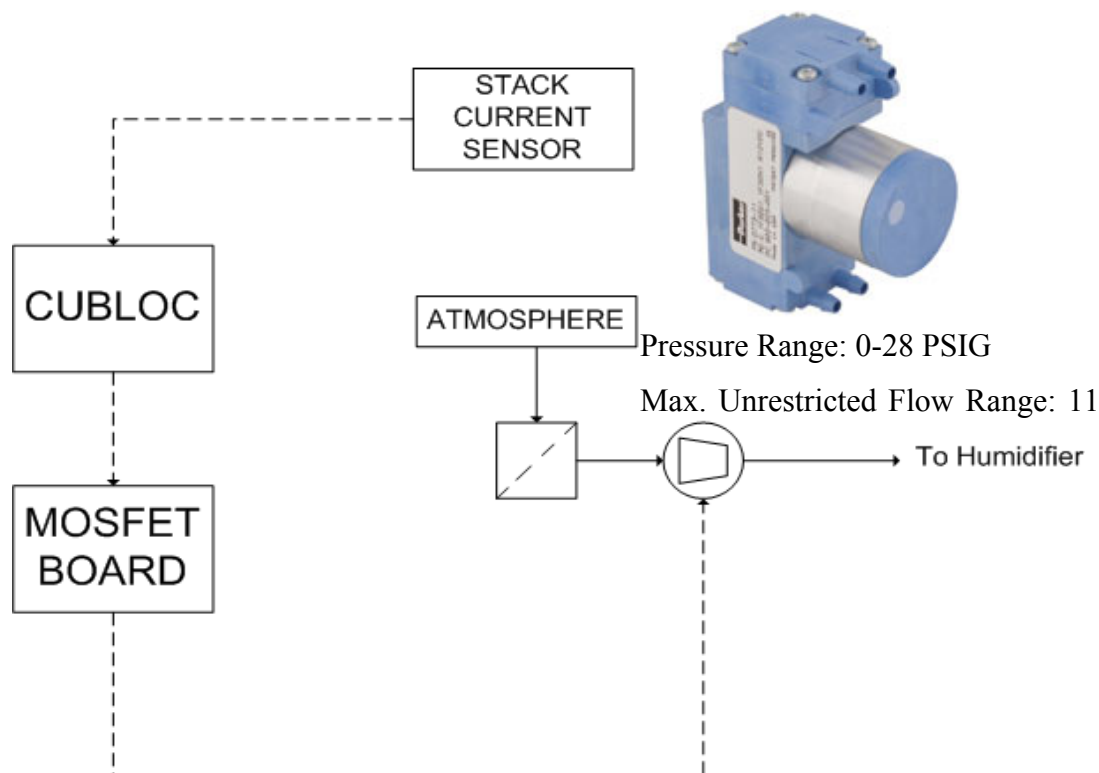


Figure 7.18 Air supply system

#### 7.4 NaBH<sub>4</sub> Hydrolysis Reactor and H<sub>2</sub> Supply System

The schematic representation of sodium borohydride storage, hydrolysis and hydrogen supply system is shown in Figure 7.19. The sodium borohydride solution is stored in a tank which is also used as liquid gas separator and hydrogen storage at 1 bar [54]. The pressure of the tank is monitored and when the pressure of the tank reduces a set point i.e. 1 bar the circulation pump starts circulating sodium borohydride solution from the tank to the catalytic hydrolysis reactor. The outlet stream of the reactor contains sodium borohydride, sodium metaborate and hydrogen gas returns to the storage tank. This circulation continues until a pressure set point.

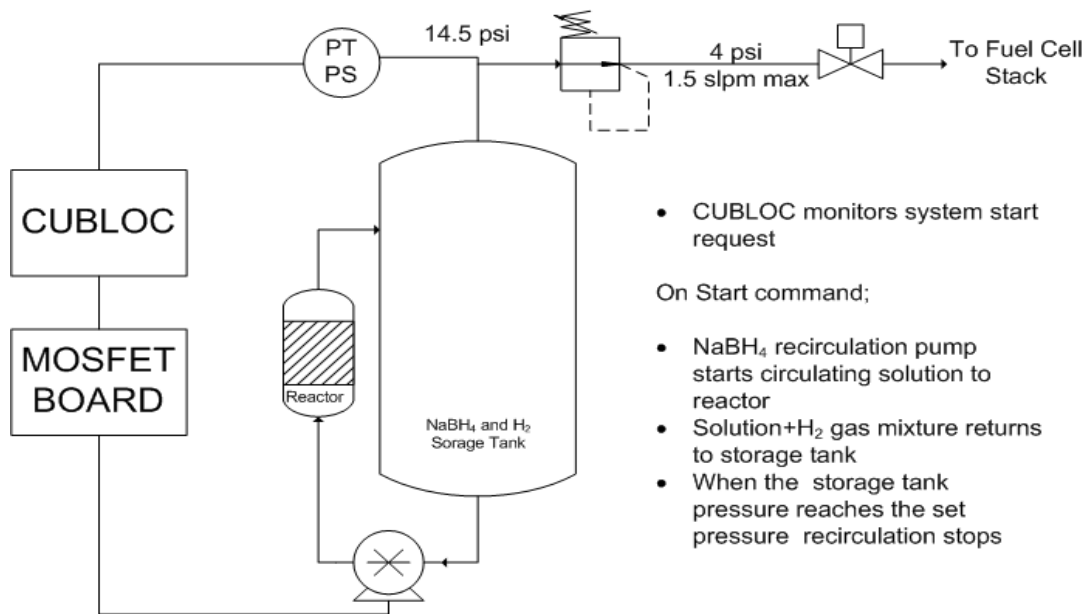


Figure 7.19 NaBH<sub>4</sub> reactor and H<sub>2</sub> supply system

## 7.5 Power Flow of System

Power flow diagram of the complete system is given in Figure 7.20. Power flows from battery or fuel cell stack according to the working status of the fuel cell stack. The startup power comes from battery pack which consists of 4 serial connected LiPo battery packages. Normally battery pack powers up the Cubloc and other peripherals. When the Cubloc decides the stack is ready to supply power it switches power from battery to fuel cell stack and Cubloc and peripherals power up from fuel cell stack. If the power comes from fuel cell stack and battery pack requires charging, Cubloc starts charging of the battery pack through battery charger module. If fuel cell is ready to supply power to user, Cubloc lets current drawn from fuel cell stack.

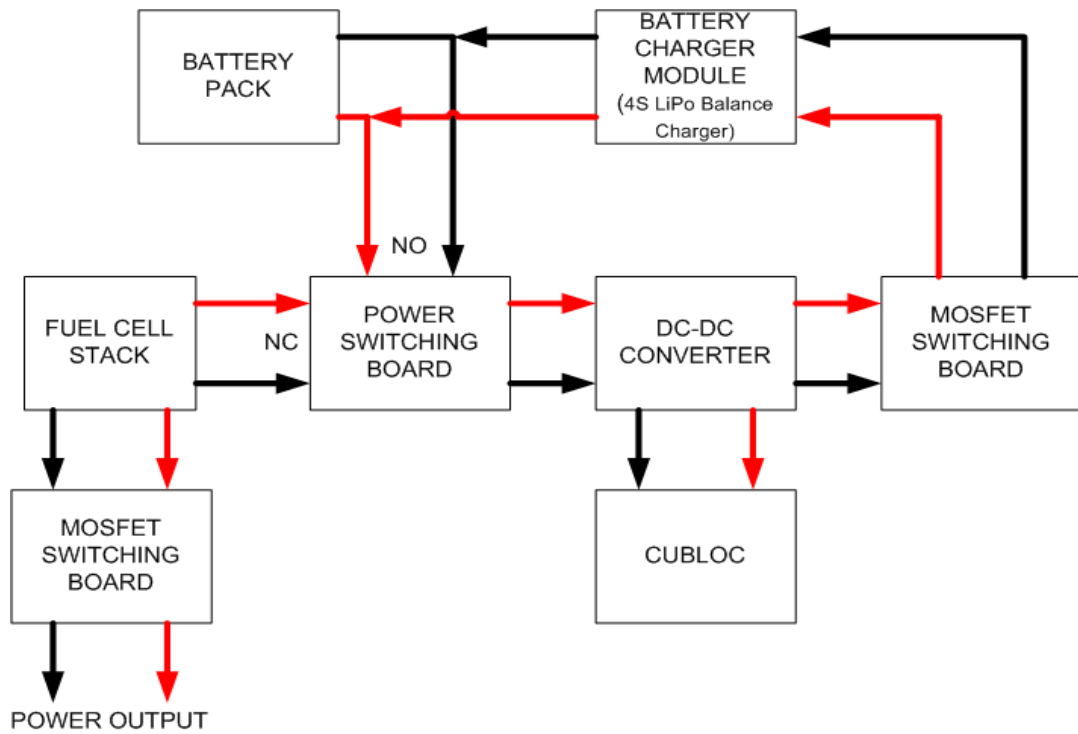


Figure 7.20 Power flow block diagram

The control system hardware is manufactured and the individual operations of the functions were tested. The hardware can manipulate the motor speeds, measure 24 voltages of the cells and can measure the battery pack voltage, the temperature can be read, battery to fuel cell power switching can be performed without interrupting the system. A graphical user interface has been designed in order to test the functionality of the control system. Further tests with assembled fuel cell system are suggested to be performed.

## CHAPTER 8

### CONCLUSION AND RECOMMENDATIONS

In this study, a 100W PEM fuel cell system working with sodium borohydride designed, manufactured, and tested. The study was performed in membrane electrode assembly development, stack development, control system development, and system integration parts.

The membrane electrode assembly is an important part of a PEM fuel cell. Its components (catalyst, membrane, gas diffusion layer) and preparation technique significantly affect the performance of the fuel cell. A previously developed technique has been applied for many years by Middle East Technical University Fuel Cell Research Center (FCRC) group [4, 5]. This technique is spraying of catalyst ink with air pressure atomizing spray brush (or simply air brush) onto the microporous layer coated side of the gas diffusion layer. The power density can be reached with this method was  $0.3 \text{ W/cm}^2$  at 0.45V cell potential. The nature of the manufacturing technique is strongly dependent on the hand operation of the operator. Therefore, the produced membrane electrode assemblies are not identical with this method. This method is also not applicable for larger active area and large number of membrane electrode assemblies.

Achievements in this thesis

### 1. Improving MEA manufacturing technique

A new technique called “ultrasonic spray coating technique” is developed to increase the MEA performance. The power densities reached with this new method are 0.53, 0.74, 0.77, and 0.88 W/cm<sup>2</sup> for 20%, 40%, 50%, 70% Pt/C catalyst by keeping 0.4mg Pt/cm<sup>2</sup> loading constant, respectively. The power density increase is %267 compared to “spraying of catalyst ink with air pressure atomizing spray gun”

The process for the production of the MEAs for volume production or high power stacks is also achieved.

### 2. Bipolar plate design

Evenly distributed flow of air or hydrogen in the flow field channels is achieved by theoretical work and consequently the bipolar plate design is improved.

It should be emphasized that the Solidworks is very convenient software for the mechanical 3D designs. Four bipolar plate and three flow field have been designed throughout the study. First two bipolar plates have “mixed serpentine” flow channels. Simulation of the mixed serpentine flow geometry revealed a non-uniform flow distribution through the channels. However, uniform gas flow distribution has been achieved “multi channel serpentine” geometry as is suggested in the present work. This improved flow geometry design has been used with Design 3 and Design 4.

### 3. Manufacturing of bipolar plates

Metallic and graphite bipolar plates are manufactured by CNC technique in Fuel Cell Technology Laboratory. Aluminum bipolar plate machining is more convenient than

graphite bipolar plate machining since graphite is an abrasive material and it is difficult to observe consistent machining tolerances.

#### 4. New coating materials and techniques are investigated.

Aluminum bipolar plates are coated with nickel, a special alloy, and graphite-PVDF. The comparison of the coatings in terms of durability has resulted that Sn-Ag-Ti soldering is more durable than nickel coating. The performances of coated bipolar plates are in the order of Sn-Ag-Ti soldering > graphite-PVDF coating > nickel coating > uncoated aluminum. The degradation rate of the fuel cell assembled with Sn-Ag-Ti solder coated and nickel coated bipolar plates are  $1.9 \frac{mV}{h}$  and  $15.5 \frac{mV}{h}$ , respectively. Graphite bipolar plates are superior compared to uncoated aluminum bipolar plates. The coating proposed in this thesis work are not sufficient to eliminate corrosion during the operation. Therefore, a suitable coating material needs to be searched for future.

#### 5. Design and manufacturing of stack completed

Two prototype stacks are manufactured. A novel design is proposed in this thesis for the stack is very promising. A suitable liquid seal material has to be investigated. The specifications of the developed and manufactured air cooled stacks are given Table 8.1.

Table 8.1 The specifications of the developed and manufactured stacks

	Design 1	Design 2
Cell potential	12V	14.4V
Number of cells	20	24
Active area per cell	12.25cm <sup>2</sup>	23cm <sup>2</sup>
Power of the stack	50W	155W

6. Fuel cell system controller hardware is designed and manufactured.

A compact control system which can be used with the system developed during this thesis was designed, manufactured and tested. The control system developed might be applied for any fuel cell system with smaller or larger in size. The compact cell voltage monitor system developed during the thesis study is not available on the market.

Recommendations:

- I) The performances of the MEAs may be further improved by optimizing “ultrasonic spray coating” method. It should be emphasized that by concentrating only on the optimization of the ink composition, process parameters like frequency, speed etc. the membrane electrode assembly performance might be further increased.
- II) The durability of the MEAs should be tested. The factors affecting the durability of the MEAs might be investigated.
- III) Metallic bipolar plates can be further investigated.
- IV) CNC machining is applicable for the prototype production but it is not feasible for the mass production. Feasible methods should be developed.

- V) The durability and the life time of the stack developed can be tested.
- VI) The load cycling, start-up and shut down, cold start behavior of the stack can be investigated.
- VII) A suitable liquid seal material has to be investigated.
- VIII) Sodium borohydride integration and response of the system to the dynamic load conditions may be investigated.
- IX) The control algorithm might be improved by system dynamics analysis.

## REFERENCES

1. Eg, Services G., *Fuel cell handbook [electronic resource] / EG&G Technical Services, Inc.* Morgantown, WV :, U.S. Dept. of Energy, Office of Fossil Energy, National Energy Technology Laboratory, 2004.
2. Hermann A., Chaudhuri T., Spagnol P., Bipolar plates for PEM fuel cells: A review. *International Journal of Hydrogen Energy* 2005, 30, 1297-1302.
3. Lin J.H., Chen W.H., Su Y.J., Ko T.H., Effect of gas diffusion layer compression on the performance in a proton exchange membrane fuel cell. *Fuel* 2008, 87, 2420-2424.
4. Bayraceken A., Erkan S., Turker L., Eroglu I., Effects of membrane electrode assembly components on proton exchange membrane fuel cell performance. *International Journal of Hydrogen Energy* 2008, 33, 165-170.
5. Sengul E., Erkan S., Bac N., Eroglu I., Effect of Gas Diffusion Layer Characteristics and Addition of Pore-Forming Agents on the Performance of Polymer Electrolyte Membrane Fuel Cells. *Chemical Engineering Communications* 2009, 196, 161-170.
6. Barbir F., *PEM Fuel Cells: Theory and Practice*. Elsevier Inc., 2005.
7. Ullmann F., *Ullmann's encyclopedia of industrial chemistry*. Wiley-VCH, 2003.
8. Kirk R.E., Othmer D.F., Kroschwitz J.I., Howe-Grant M., *Encyclopedia of chemical technology*. Wiley, 1998.
9. Larminie J., Dicks A., *Fuel cell systems explained*. Wiley, 2000.
10. Damiano P.J., Fuel Cell Structure. In 1978.

11. Smitha B., Sridhar S., Khan A.A., Solid polymer electrolyte membranes for fuel cell applications - a review. *Journal of Membrane Science* 2005, 259, 10-26.
12. Hoogers G., *Fuel cell technology handbook*. CRC Press, 2003.
13. Ficicilar B., Bayrakceken A., Eroglu I., Effect of Pd loading in Pd-Pt bimetallic catalysts doped into hollow core mesoporous shell carbon on performance of proton exchange membrane fuel cells. *Journal of Power Sources* 2009, 193, 17-23.
14. Bayrakçeken A., Platinum and Platinum-Ruthenium Based Catalysts on Various carbon Supports Prepared by Different Methods for PEM Fuel Cell Applications. In *PhD. Thesis in Chemical Engineering Department*. Ankara, Middle East Technical University, 2008, 165.
15. Nam J.H., Lee K.-J., Hwang G.-S., Kim C.-J., Kaviany M., Microporous layer for water morphology control in PEMFC. *International Journal of Heat and Mass Transfer* 2009, 52, 2779-2791.
16. Park S., Lee J.-W., Popov B.N., Effect of PTFE content in microporous layer on water management in PEM fuel cells. *Journal of Power Sources* 2008, 177, 457-463.
17. Ramasamy R.P., FUEL CELLS - PROTON-EXCHANGE MEMBRANE FUEL CELLS | Membrane-Electrode Assemblies. In x00Fc, rgen G. eds. *Encyclopedia of Electrochemical Power Sources*. Amsterdam, Elsevier, 2009, 787-805.
18. Zhang J., Yin G., Wang Z., Shao Y., Effects of MEA preparation on the performance of a direct methanol fuel cell. *Journal of Power Sources* 2006, 160, 1035-1040.
19. Zhou P., Wu C.W., Numerical study on the compression effect of gas diffusion layer on PEMFC performance. *Journal of Power Sources* 2007, 170, 93-100.
20. Tan J., Chao Y.J., Zee J.W.V., Lee W.K., Degradation of elastomeric gasket materials in PEM fuel cells. *Materials Science and Engineering A* 2007, 445-446, 669-675.

21. Cleghorn S.J.C., Mayfield D.K., Moore D.A., Moore J.C., Rusch G., Sherman T.W., Sisofo N.T., Beuscher U., A polymer electrolyte fuel cell life test: 3 years of continuous operation. *Journal of Power Sources* 2006, 158, 446–454.
22. Agnolucci P., Economics and market prospects of portable fuel cells. *International Journal of Hydrogen Energy* 2007, 32, 4319-4328.
23. Trimm D.L., Onsan Z.I., Onboard fuel conversion for hydrogen-fuel-cell-driven vehicles. *Catalysis Reviews-Science and Engineering* 2001, 43, 31-84.
24. Avci A.K., Onsan Z.I., Trimm D.L., On-board hydrogen generation for fuel cell-powered vehicles: the use of methanol and propane. *Topics in Catalysis* 2003, 22, 359-367.
25. Avci A.K., Trimm D.L., Aksoylu A.E., Onsan Z.I., Hydrogen production by steam reforming of n-butane over supported Ni and Pt-Ni catalysts. *Applied Catalysis a-General* 2004, 258, 235-240.
26. Aksoylu A.E., Gokaliler F., Caglayan B.S., Onsan Z.I., Hydrogen production by autothermal reforming of LPG for PEM fuel cell applications. *International Journal of Hydrogen Energy* 2008, 33, 1383-1391.
27. Onsan Z.I., Soybal-Baltacioglu F., Aksoylu A.E., Steam reforming of ethanol over Pt-Ni Catalysts. *Catalysis Today* 2008, 138, 183-186.
28. Amendola S.C., Sharp-Goldman S.L., Janjua M.S., Kelly M.T., Petillo P.J., Binder M., An ultrasafe hydrogen generator: aqueous, alkaline borohydride solutions and Ru catalyst. *Journal of Power Sources* 2000, 85, 186-189.
29. Ozkar S., Zahmakiran M., Hydrogen generation from hydrolysis of sodium borohydride using Ru(0) nanoclusters as catalyst. *Journal of Alloys and Compounds* 2005, 404, 728-731.
30. Jeong S.U., Kim R.K., Cho E.A., Kim H.J., Nam S.W., Oh I.H., Hong S.A., Kim S.H., A study on hydrogen generation from NaBH<sub>4</sub> solution using the high-performance Co-B catalyst. *Journal of Power Sources* 2005, 144, 129-134.

31. Kim S., Lee J., Kong K., Ryuljung C., Min I., Lee S., Kim H., Nam S., Lim T., Hydrogen generation system using sodium borohydride for operation of a 400W-scale polymer electrolyte fuel cell stack. *Journal of Power Sources* 2007, 170, 412-418.
32. Ingersoll J.C., Mani N., Thenmozhiyal J.C., Muthaiah A., Catalytic hydrolysis of sodium borohydride by a novel nickel–cobalt–boride catalyst. *Journal of Power Sources* 2007, 173, 450-457.
33. Bai Y., Wu C., Wu F., Yi B., Carbon-supported platinum catalysts for on-site hydrogen generation from NaBH<sub>4</sub> solution. *Materials Letters* 2006, 60, 2236-2239.
34. Kojima Y., Development of 10 kW-scale hydrogen generator using chemical hydride. *Journal of Power Sources* 2004, 125, 22-26.
35. Hino M., Murakami K., Mitooka Y., Muraoka K., Kanadani T., Effects of zincate treatment on adhesion of electroless Ni-P coating onto various aluminum alloys. *Transactions of Nonferrous Metals Society of China* 2009, 19, 814-818.
36. Saito M., Maegawa T., Homma T., Electrochemical analysis of zincate treatments for Al and Al alloy films. *Electrochimica Acta* 2005, 51, 1017-1020.
37. USFCC Single Cell Test Protocol, Washington, DC, US Fuel Cell Council, 05-014B.2, 2006.
38. Devrim Y., Erkan S., Bac N., Eroglu I., Preparation and characterization of sulfonated polysulfone/titanium dioxide composite membranes for proton exchange membrane fuel cells. *International Journal of Hydrogen Energy* 2009, 34, 3467-3475.
39. Ergün D., High temperature proton exchange membrane fuel cells. In *MSc. Thesis in Chemical Engineering*. Ankara, Middle East Technical University, 2009, 97.
40. Erkan S., Synthesis of some metalophthalocyanines and their effects on the performance of pem fuel cells. In *MSc. Thesis in Chemical Engineering*. Ankara, Middle East Technical University, 2005, 97.

41. Qi Z., Kaufman A., Low Pt loading high performance cathodes for PEM fuel cells. *Journal of Power Sources* 2003, 113, 37-43.
42. Endoo S., Pruksathorn K., Piumsomboon P., Identification of the key variables in membrane electrode preparation for PEM fuel cells by a factorial design. *Renewable Energy* 2010, 35, 807-813.
43. Thanasilp S., Hunsom M., Effect of MEA fabrication techniques on the cell performance of Pt-Pd/C electrocatalyst for oxygen reduction in PEM fuel cell. *Fuel* 2010, 89, 3847-3852.
44. Scholta J., Development and performance of a 10kW PEMFC stack. *Journal of Power Sources* 2004, 127, 206-212.
45. Giddey S., Design, assembly and operation of polymer electrolyte membrane fuel cell stacks to 1 kWe capacity. *Journal of Power Sources* 2004, 125, 155-165.
46. Sohn Y., Park G., Yang T., Yoon Y., Lee W., Yim S., Kim C., Operating characteristics of an air-cooling PEMFC for portable applications. *Journal of Power Sources* 2005, 145, 604-609.
47. Jiang R.Z., Chu D.R., Stack design and performance of polymer electrolyte membrane fuel cells. *Journal of Power Sources* 2001, 93, 25-31.
48. Knobbe M., Active gas management for PEM fuel cell stacks. *Journal of Power Sources* 2004, 138, 94-100.
49. Hsieh S.-S., Feng C.-L., Huang C.-F., Development and performance analysis of a H<sub>2</sub>/air micro PEM fuel cell stack. *Journal of Power Sources* 2006, 163, 440-449.
50. Oszcipok M., Zedda M., Hesselmann J., Huppmann M., Wodrich M., Junghardt M., Hebling C., Portable proton exchange membrane fuel-cell systems for outdoor applications. *Journal of Power Sources* 2006, 157, 666-673.
51. Urbani F., Squadrito G., Barbera O., Giacoppo G., Passalacqua E., Zerbinati O., Polymer electrolyte fuel cell mini power unit for portable application. *Journal of Power Sources* 2007, 169, 334-337.

52. Weng F., Jou B., Su A., Chan S., Chi P., Design, fabrication and performance analysis of a 200W PEM fuel cell short stack. *Journal of Power Sources* 2007, 171, 179-185.

53. Alcaide F., Álvarez G., Blázquez J.A., Cabot P.L., Miguel O., Development of a novel portable-size PEMFC short stack with electrodeposited Pt hydrogen diffusion anodes. *International Journal of Hydrogen Energy* 2010, 35, 5521-5527.

54. Boran A., Design of prototype reactor for hydrogen production from sodium borohydride. In *MSc. Thesis in Chemical Engineering*. Ankara, Middle East Technical University, 2011.

## APPENDIX A

### SAMPLE CALCULATION FOR STACK DESIGN

#### A.1 Design Basis

Design power

$$P := 117.6W$$

Design current density at 0.6V

$$i := 500 \frac{\text{mA}}{\text{cm}^2}$$

Design power density at 0.6V

$$p := 0.6V \cdot i$$

Number of electrons involved

$$n := 2$$

Faraday Constant

$$F_c := 96485 \frac{\text{coul}}{\text{mol}}$$

Total active area to reach design Power

$$TAA := \frac{P}{p} \quad TAA = 0.039\text{m}^2$$

Operating Pressure

$$P_{an} := 1.5\text{atm}$$

$$P_{cat} := P_{an}$$

$$R_g := 8.314 \frac{\text{J}}{\text{mol} \cdot \text{K}}$$

$$Temp := (60 + 273.15)\text{K}$$

$$T_{airin\text{atm}} := 298.15\text{K}$$

$$T_{anin} := 298.15\text{K}$$

$$T_{anout} := Temp$$

$$T_{catout} := Temp$$

$$T_{catin} := Temp$$

Reference state is 25°C (298.15K) 1 atm

$$T_{ref} := 298.15\text{K}$$

$$T_{environment} := (25 + 273.15)\text{K}$$

Vapor Pressure of water between 0 and 100°C

$$A_c := -5800.2206$$

$$B_c := 1.391499$$

$$C_c := 0.04864023$$

$$D_c := 0.4176476810^{-4}$$

$$E_c := 0.1445209310^{-7}$$

$$F_c := 6.545967$$

$$P_{vap}(T) := e^{A_c \cdot K \cdot T^{-1} + B_c - C_c \cdot \frac{1}{K} \cdot T + D_c \cdot \frac{1}{K^2} \cdot T^2 - E_c \cdot \frac{1}{K^3} \cdot T^3 + F_c \ln\left(T \cdot \frac{1}{K}\right)} \cdot \text{Pa}$$

Design potential  $V_{\text{design}} := 12\text{V}$

Number of Cells  $N_{\text{cell}} := \frac{V_{\text{design}}}{0.6\text{V}} \quad N_{\text{cell}} = 20$

Cell Active Area  $A_{\text{cell}} := \frac{TAA}{N_{\text{cell}}} \quad A_{\text{cell}} = 1.96 \times 10^{-3} \text{ m}^2$

Square shape active area dimension (side length)  $L_{\text{aa}} := \sqrt{A_{\text{cell}}} \quad L_{\text{aa}} = 0.044\text{m}$

Total Current of stack at Maximum Power  $I_{\text{atmaxP}} := i \cdot A_{\text{cell}} \quad I_{\text{atmaxP}} = 9.8\text{A}$

### Properties Table

$M_{\text{H}_2} := 2.0158 \frac{\text{gm}}{\text{mol}}$	$C_{\text{pH}_2} := 14.2 \frac{\text{J}}{\text{gm}\cdot\text{K}}$	$N_{\text{CpH}_2} := C_{\text{pH}_2} \cdot M_{\text{H}_2}$
$M_{\text{O}_2} := 31.9988 \frac{\text{gm}}{\text{mol}}$	$C_{\text{pO}_2} := 0.913 \frac{\text{J}}{\text{gm}\cdot\text{K}}$	$N_{\text{CpO}_2} := C_{\text{pO}_2} \cdot M_{\text{O}_2}$
$M_{\text{N}_2} := 28.0134 \frac{\text{gm}}{\text{mol}}$	$C_{\text{pN}_2} := 1.04 \frac{\text{J}}{\text{gm}\cdot\text{K}}$	$N_{\text{CpN}_2} := C_{\text{pN}_2} \cdot M_{\text{N}_2}$
$M_{\text{air}} := 28.848 \frac{\text{gm}}{\text{mol}}$	$C_{\text{pair}} := 1.01 \frac{\text{J}}{\text{gm}\cdot\text{K}}$	$N_{\text{Cpair}} := C_{\text{pair}} \cdot M_{\text{air}}$
$M_{\text{H}_2\text{O}} := 18.0152 \frac{\text{gm}}{\text{mol}}$	$C_{\text{pH}_2\text{Ov}} := 1.87 \frac{\text{J}}{\text{gm}\cdot\text{K}}$	$N_{\text{CpH}_2\text{Ov}} := C_{\text{pH}_2\text{Ov}} \cdot M_{\text{H}_2\text{O}}$
	$C_{\text{pH}_2\text{OL}} := 4.18 \frac{\text{J}}{\text{gm}\cdot\text{K}}$	$N_{\text{CpH}_2\text{OL}} := C_{\text{pH}_2\text{OL}} \cdot M_{\text{H}_2\text{O}}$
$H_{\text{H}_2\_h\text{hv}298} := 285840 \frac{\text{J}}{\text{mol}}$		

## A.2 Mass Balance

### A.2.1 Inlet flow rates

Hydrogen (semi batch operation)

Hydrogen consumed by fuel cell reaction at Max Power  $N_{\text{H}_2} := \frac{I_{\text{atmaxP}}}{n \cdot F_c}$

For dead-end operation 1% of hydrogen consumed is purged  $SH_2 := 1.01$

Total Hydrogen Consumption Rate of fuel cell at max power  $NH_{2in} := N_{cell} \cdot NH_2 \cdot SH_2$

Hydrogen consumption in SLPM  $NH_{2in} = 1.026 \times 10^{-3} \frac{\text{mol}}{\text{s}}$

$$H_2C := \frac{NH_{2in} \cdot R_g \cdot T_{in}}{1 \text{ atm}} \quad H_2C = 2.51 \times 10^{-5} \frac{\text{m}^3}{\text{s}} \quad H_{2CinSLPM} := \frac{H_2C}{\left(1.667 \times 10^{-5} \frac{\text{m}^3}{\text{s}}\right)}$$

Air (continuous steady state operation)

Oxygen ratio of air (inlet)  $r_{O_2in} := 0.2095$

Oxygen Stoichiometric Ratio  $SO_2 := 2.5$   $\frac{\text{L}}{\text{min}} = 1.667 \times 10^{-5} \frac{\text{m}^3}{\text{s}}$

Inlet oxygen

Oxygen inlet flow rate at max Power  $NO_{2in} := SO_2 \cdot \frac{I_{atmaxP}}{4F_c} \cdot N_{cell}$

$$NO_{2in} = 1.27 \times 10^{-3} \frac{\text{mol}}{\text{s}}$$

$$MO_{2in} := NO_{2in} \cdot M_{WO_2} = 4.063 \times 10^{-5} \frac{\text{kg}}{\text{s}}$$

$$MO_{2inPerHour} := MO_{2in} \cdot 3600 \text{ s} = 0.146 \text{ kg}$$

Air inlet flow rate at max Power

$$N_{airin} := \frac{SO_2}{r_{O_2in}} \cdot \frac{I_{atmaxP}}{4F_c} \cdot N_{cell}$$

Nitrogen inlet flow rate at max Power

$$N_{airin} = 6.06 \times 10^{-3} \frac{\text{mol}}{\text{s}}$$

$$MN2_{in} := NN2_{in} \cdot MWN2 = 1.342 \times 10^{-4} \frac{\text{kg}}{\text{s}} \quad NN2_{in} := \text{SO2} \cdot \frac{1}{4 \cdot Fc} \cdot \frac{1 - rO2_{in}}{rO2_{in}} \cdot I_{atmaxP} \cdot N_{cell}$$

$$MN2_{inPerHour} := MN2_{in} \cdot 3600\text{s} = 0.483\text{kg} \quad NN2_{in} = 4.791 \times 10^{-3} \frac{\text{mol}}{\text{s}}$$

Water

Water vapor in hydrogen inlet  $\psi_{an} := 0$

$$NH2O_{inH2in} := SH2 \cdot \frac{I_{atmaxP}}{2 \cdot Fc} \cdot N_{cell} \cdot \frac{\psi_{an} \cdot P_{vap}(\text{Temp})}{P_{an} - \psi_{an} \cdot P_{vap}(\text{Temp})}$$

$$NH2O_{inH2in} = 0$$

Water vapor in air inlet  $\psi_{cat} := 1$

$$NH2O_{inAirin} := \frac{\text{SO2}}{rO2_{in}} \cdot \frac{I_{atmaxP}}{4Fc} \cdot N_{cell} \cdot \frac{\psi_{cat} \cdot P_{vap}(\text{Temp})}{P_{cat} - \psi_{cat} \cdot P_{vap}(\text{Temp})}$$

$$NH2O_{inAirin} = 9.153 \times 10^{-4} \frac{\text{mol}}{\text{s}}$$

$$MH2O_{inAirin} := NH2O_{inAirin} \cdot MWH2O$$

$$MH2O_{inAirin} \text{kgperhour} := MH2O_{inAirin} \cdot 3600\text{s} = 0.059\text{kg}$$

$$MH2O_{inAirin} \text{kgperminute} := \frac{MH2O_{inAirin} \text{kgperhour}}{60} = 9.894 \times 10^{-4} \text{kg}$$

## A.2.2 Outlet flow rates

Anode

Purged hydrogen flow rate (average)  $NH2_{out} := (SH2 - 1) \cdot \frac{I_{atmaxP}}{2Fc} \cdot N_{cell}$

$$NH2_{out} = 1.016 \times 10^{-5} \frac{\text{mol}}{\text{s}}$$

Water out

Assume  $\zeta := 1$  (each proton is accompanied by one water molecule to form H3O+)

Due to electro osmotic drag (From anode to cathode)  $NH2O_{ED} := \zeta \cdot \frac{I_{atmaxP}}{Fc} \cdot N_{cell}$

$$\text{NH}_2\text{OED} = 2.031 \times 10^{-3} \frac{\text{mol}}{\text{s}}$$

Due to Back diffusion (From cathode to anode)  $\beta := 1.0$      $\text{NH}_2\text{OBD} := \beta \cdot \text{NH}_2\text{OED}$

$$\text{NH}_2\text{OBD} = 2.031 \times 10^{-3} \frac{\text{mol}}{\text{s}}$$

Total water out from Anode     $\text{NH}_2\text{OinH}_2\text{out} := \text{NH}_2\text{OinH}_2\text{in} - \text{NH}_2\text{OED} + \text{NH}_2\text{OBD}$

$$\Delta P_{\text{an}} := 1 \text{ atm}$$

Water out from anode in vapor phase

$$\text{NH}_2\text{OinH}_2\text{outV} := \min \left[ (\text{SH}_2 - 1) \cdot \frac{\text{IatmaxP}}{2F_c} \cdot \frac{\text{Pvap}(\text{Temp})}{\text{Pan} - \Delta P_{\text{an}} - \text{Pvap}(\text{Temp})} \cdot \text{Ncell}, \text{NH}_2\text{OinH}_2\text{out} \right]$$

$$\text{NH}_2\text{OinH}_2\text{outV} = 0 \frac{\text{mol}}{\text{s}}$$

Water out from anode in Liquid phase  
(if exists)

$$\text{NH}_2\text{OinH}_2\text{outL} = 0 \frac{\text{mol}}{\text{s}}$$

Cathode

$$\text{NH}_2\text{OinH}_2\text{outL} := \text{NH}_2\text{OinH}_2\text{out} - \text{NH}_2\text{OinH}_2\text{outV}$$

$$\Delta P_{\text{cat}} := 95.65 \text{ Pa}$$

Oxygen Flow rate at cathode exhaust     $\text{NO}_2\text{out} := (\text{SO}_2 - 1) \cdot \frac{\text{IatmaxP}}{4F_c} \cdot \text{Ncell}$

$$\text{NO}_2\text{out} = 7.618 \times 10^{-4} \frac{\text{mol}}{\text{s}}$$

Nitrogen flow rate at the cathode exhaust     $\text{NN}_2\text{out} := \text{NN}_2\text{in}$

$$\text{NN}_2\text{out} = 4.791 \times 10^{-3} \frac{\text{mol}}{\text{s}}$$

Air flow rate at the cathode exhaust     $\text{NAirout} := \text{NO}_2\text{out} + \text{NN}_2\text{out}$

$$r_{O2out} := \frac{SO2 - 1}{\frac{SO2}{r_{O2in}} - 1}$$

$$N_{Airout} = 5.552 \times 10^{-3} \frac{\text{mol}}{\text{s}}$$

Oxygen volume fraction at outlet (Dry)

$$r_{O2out} = 0.137$$

$$\text{Oxygen volume fraction at outlet (wet)} \quad r_{O2outwet} := r_{O2out} \cdot \left( 1 - \frac{\psi_{cat} \cdot P_{vap}(\text{Temp})}{P_{cat}} \right)$$

$$r_{O2outwet} = 0.119$$

Water generated is equal to Hydrogen consumed

$$NH_{2Ogen} := \frac{I_{atmaxP}}{n \cdot Fc} \cdot N_{cell}$$

Total water out from cathode

$$NH_{2OinAirout} := NH_{2OinAirin} + NH_{2Ogen} + NH_{2OED} - NH_{2OBE}$$

$$NH_{2OinAirout} = 1.931 \times 10^{-3} \frac{\text{mol}}{\text{s}}$$

Water out from cathode in vapor phase

$$NH_{2OinAiroutV} = \min \left[ \left( \frac{SO2 - r_{O2in}}{r_{O2in}} \cdot \frac{I_{atmaxP}}{4 \cdot Fc} \cdot N_{cell} \cdot \frac{P_{vap}(\text{Temp})}{P_{cat} - \Delta P_{cat} - P_{vap}(\text{Temp})} \right), NH_{2OinAirout} \right]$$

$$NH_{2OinAiroutV} = 8.392 \times 10^{-4} \frac{\text{mol}}{\text{s}}$$

$$MH_{2OinAiroutVperhour} := NH_{2OinAiroutV} \cdot M_{WH2O} \cdot 3600s = 0.054kg$$

Water out from cathode in Liquid phase  
(if exists)

$$NH_{2OinAiroutL} := NH_{2OinAirout} - NH_{2OinAiroutV}$$

$$NH_{2OinAiroutL} = 1.092 \times 10^{-3} \frac{\text{mol}}{\text{s}}$$

$$MH_{2OinAiroutLperhour} := NH_{2OinAiroutL} \cdot M_{WH2O} \cdot 3600s = 0.071kg$$

### A.3 Energy Balance

#### A.3.1 Input

$$\begin{aligned} \text{HH2in} &:= \text{NH2in} \cdot [\text{H\_H2\_hhv298} + \text{NCpH2} \cdot (\text{Tanin} - \text{Tref})] & \text{HH2in} &= 293.232\text{W} \\ \text{HO2in} &:= \text{NO2in} \cdot [\text{NCpO2} \cdot (\text{Tcatin} - \text{Tref})] & \text{HO2in} &= 1.298\text{W} \\ \text{HN2in} &:= \text{NN2in} \cdot [\text{NCpN2} \cdot (\text{Tcatin} - \text{Tref})] & \text{HN2in} &= 4.885\text{W} \\ \text{HH2Ovin} &:= \text{NH2OinAirin} \cdot [\text{NCpH2Ov} \cdot (\text{Tcatin} - \text{Tref})] + \text{NH2OinH2in} \cdot [\text{NCpH2Ov} \cdot (\text{Tcatin} - \text{Tref})] & \text{HH2Ovin} &= 1.079\text{W} \\ \text{Hin} &:= \text{HH2in} + \text{HO2in} + \text{HN2in} + \text{HH2Ovin} & \text{Hin} &= 300.494\text{W} \end{aligned}$$

#### A.3.2 Output

$$\begin{aligned} \text{HH2out} &:= \text{NH2out} \cdot [\text{H\_H2\_hhv298} + \text{NCpH2} \cdot (\text{Tanout} - \text{Tref})] & \text{HH2out} &= 2.913\text{W} \\ \text{HO2out} &:= \text{NO2out} \cdot [\text{NCpO2} \cdot (\text{Tcatout} - \text{Tref})] & \text{HO2out} &= 0.779\text{W} \\ \text{HN2out} &:= \text{NN2out} \cdot [\text{NCpN2} \cdot (\text{Tcatout} - \text{Tref})] & \text{HN2out} &= 4.885\text{W} \\ \text{HH2Ovout} &:= \text{NH2OinAiroutV} \cdot [\text{NCpH2Ov} \cdot (\text{Tcatout} - \text{Tref})] + \text{NH2OinH2outV} \cdot [\text{NCpH2Ov} \cdot (\text{Tcatout} - \text{Tref})] & \text{HH2Ovout} &= 0.99\text{W} \\ \text{Hout} &:= \text{HH2out} + \text{HO2out} + \text{HN2out} + \text{HH2Ovout} + \text{HH2OLout} & \text{Hout} &= 12.444\text{W} \\ \text{HH2OLout} &:= \text{NH2OinAiroutL} \cdot [\text{NCpH2OL} \cdot (\text{Tcatin} - \text{Tref})] + \text{NH2OinH2outL} \cdot [\text{NCpH2OL} \cdot (\text{Tcatin} - \text{Tref})] & & \\ & & \text{HH2OLout} &= 2.878\text{W} \end{aligned}$$

Steady-state energy Balance is  $0 = \text{Hin} - \text{Hout} - \text{Wel} - \text{Q}$

$$\text{Q} := \text{Hin} - \text{Hout} - \text{P}$$

$$\text{Q} = 170.45\text{W}$$

#### A.4 Summary of Results

Stack Design Power	$P = 117.6W$
Design current Density at 0.6V	$i = 5 \times 10^3 \frac{A}{m^2}$
Design Potential	$V_{design} = 12V$
Total active area	$TAA = 0.039m^2$
Number of Cells	$N_{cell} = 20$
Active area of a cell	$A_{cell} = 1.96 \times 10^{-3} m^2$
Current at Maximum Power	$i_{atmaxP} = 9.8A$
Hydrogen Flow rate at Maximum Power	$NH_{2in} = 1.026 \times 10^{-3} \frac{mol}{s}$
Total Hydrogen Consumption per hour operation	$HC_{perH} := NH_{2in} \cdot 1hr = 3.693mol$
Hydrogen consumption in SLPM	$MHC_{perH} := MWH_2 \cdot HC_{perH} = 7.445 \times 10^{-3} kg$  $H_2C_{inSLPM} = 1.505$ $MHC_{perH} = 7.445 \times 10^{-3} kg$
Air Consumption rate at Maximum Power	$AirC := \frac{N_{airin} \cdot R_g \cdot T_{airin} \cdot i_{atmaxP}}{i_{atm}}$  $AirC = 1.483 \times 10^{-4} \frac{m^3}{s}$
Air Consumption in L/min at Maximum Power	$AirC_{inSLPM} := \frac{AirC}{\left(1.667 \times 10^{-5} \frac{m^3}{s}\right)}$  $AirC_{inSLPM} = 8.894$
Water Generation Rate at Maximum Power	$MH_2O_{gen} := NH_2O_{gen} \cdot MWH_2O$
Total water generated per hour of operation at max power	$MH_2O_{gen} = 1.83 \times 10^{-5} \frac{kg}{s}$ $TMH_2O_{gen} := MH_2O_{gen} \cdot hr$ $TMH_2O_{gen} = 0.066kg$
Thermal energy generation at Maximum power	$Q = 170.45W$ $E_{thermal} := Q \cdot hr$

Total Thermal Energy generated  
for 1 hr of operation at Max Power

$$E_{\text{thermal}} = 6.136 \times 10^5 \text{ J}$$

Required Active area for the design power is  $A_{\text{cell}} = 1.96 \times 10^{-3} \text{ m}^2$ . However, one may not obtain a suitable flow field design if serpentine shaped flow field is chosen with the active area actually meet the design power.

### A.5 Pressure Drop Calculations

For a serpentine design for every channel length is  $ChL := 107 \text{ mm}$  and number of channels parallel is  $N_{ch} := 6$ . Channel width  $W_c := 1 \text{ mm}$ , space between channels  $WL := 1 \text{ mm}$ , channel depth  $d_c := 1 \text{ mm}$ . Then actual active area with the specified available design is

$$A_{\text{celld}} := 35 \text{ mm} \cdot 35 \text{ mm}$$

$$A_{\text{celld}} = 1.225 \times 10^{-3} \text{ m}^2$$

Stack current  $I_{\text{atmaxP}} := i \cdot A_{\text{celld}}$

$$I_{\text{atmaxP}} = 6.125 \text{ A}$$

Corrected stack Power  $P_{\text{corrected}} := V_{\text{design}} \cdot I_{\text{atmaxP}}$

$$P_{\text{corrected}} = 73.5 \text{ W}$$

Total number of channels in stack  $N_{ch} := N_{\text{cell}} \cdot 6$   $N_{ch} = 120$

H2 flow in per channel  $NH_{2\text{pchin}} := \frac{NH_{2\text{in}}}{N_{ch}}$

$$NH_{2\text{pchin}} = 8.549 \times 10^{-6} \frac{\text{mol}}{\text{s}}$$

Hydrogen velocity (in a single channel) at the specified temperature is

$$v_{H2} := \frac{(N_{H2pchin} \cdot R_g \cdot T_{anin})}{(P_{an} - \psi_{an} \cdot P_{vap}(T_{anin})) \cdot W_c^2}$$

$$v_{H2} = 0.139 \frac{m}{s}$$

$$\text{Air flow in per channel (Dry)} \quad \text{AirFinSLPMpch} := \frac{\text{AirCinSLPM}}{N_{ch}}$$

$$\text{AirFinSLPMpch} = 0.074$$

$$N_{\text{Airpchin}} := \frac{N_{\text{airin}}}{N_{ch}}$$

$$N_{\text{Airpchin}} = 5.05 \times 10^{-5} \frac{\text{mol}}{s}$$

Air velocity (in a single channel) at the specified temperature is

$$v_{\text{Air}} := \frac{(N_{\text{Airpchin}} \cdot R_g \cdot T_{catin})}{(P_{cat} - \psi_{cat} \cdot P_{vap}(T_{anin})) \cdot W_c^2}$$

$$v_{\text{Air}} = 0.94 \frac{m}{s}$$

$$\text{Hydraulic Diameter of a channel} \quad \text{DH} := \frac{2 \cdot W_c \cdot d_c}{W_c + d_c} \quad \text{DH} = 1 \times 10^{-3} \text{ m}$$

Viscosities of hydrogen, air and water vapor as a function of Temperature are

$$\mu_{H2}(T) := 0.92 \cdot 10^{-5} \frac{\text{kg}}{\text{m} \cdot \text{s}} \cdot \left( \frac{298.15\text{K} + 72\text{K}}{T + 72\text{K}} \right) \cdot \left( \frac{T}{298.15\text{K}} \right)^{\frac{3}{2}}$$

$$\mu_{\text{Air}}(T) := 1.81 \cdot 10^{-5} \frac{\text{kg}}{\text{m} \cdot \text{s}} \cdot \left( \frac{298.15\text{K} + 120\text{K}}{T + 120\text{K}} \right) \cdot \left( \frac{T}{298.15\text{K}} \right)^{\frac{3}{2}}$$

$$\mu_{H2Ovap}(T) := 1.02 \cdot 10^{-5} \frac{\text{kg}}{\text{m} \cdot \text{s}} \cdot \left( \frac{298.15\text{K} + 660\text{K}}{T + 660\text{K}} \right) \cdot \left( \frac{T}{298.15\text{K}} \right)^{\frac{3}{2}}$$

The calculation of the mixture viscosities is as follows;

$$\Phi 1(\mu 1, \mu 2, r 1, r 2) := \frac{\sqrt{2}}{4} \cdot \left[ 1 + \left( \frac{\mu 1}{\mu 2} \right)^{0.5} \cdot \left( \frac{r 2}{r 1} \right)^{0.25} \right]^2 \cdot \left( 1 + \frac{r 1}{r 2} \right)^{-0.5}$$

$$\Phi 2(\mu 1, \mu 2, r 1, r 2) := \frac{\sqrt{2}}{4} \cdot \left[ 1 + \left( \frac{\mu 2}{\mu 1} \right)^{0.5} \cdot \left( \frac{r 1}{r 2} \right)^{0.25} \right]^2 \cdot \left( 1 + \frac{r 2}{r 1} \right)^{-0.5}$$

$$\mu_{\text{mix}}(\mu 1, \mu 2, r 1, r 2, M 1, M 2) := \frac{\mu 1}{1 + \Phi 1(\mu 1, \mu 2, r 1, r 2) \cdot \frac{M 2}{M 1}} + \frac{\mu 2}{1 + \Phi 2(\mu 1, \mu 2, r 1, r 2) \cdot \frac{M 1}{M 2}}$$

where

$\mu 1, \mu 2$  are the viscosities of components 1 and 2

$r 1, r 2$  are the volume fractions of components 1 and 2 in the mixture

$M 1, M 2$  are the molecular weights of components 1 and 2

Anode feed hydrogen is dry  $\mu_{\text{anode}} := \mu_{\text{H2}}(\text{Tanin})$

$$\mu_{\text{anode}} = 9.2 \times 10^{-6} \frac{\text{kg}}{\text{m}\cdot\text{s}}$$

Cathode feed is air water mixture

$$\mu_{\text{cathode}} := \mu_{\text{mix}}\left(\mu_{\text{Air}}(\text{Tcatin}), \mu_{\text{H2Ovap}}(\text{Tcatin}), \frac{N_{\text{airin}}}{N_{\text{airin}} + N_{\text{H2OinAirin}}}, \frac{N_{\text{H2OinAirin}}}{N_{\text{airin}} + N_{\text{H2OinAirin}}}, M_{\text{Wair}}, M_{\text{WH2O}}\right)$$

$$\mu_{\text{cathode}} = 1.883 \times 10^{-5} \frac{\text{kg}}{\text{m}\cdot\text{s}}$$

Density of anode gas  $\rho_{\text{anode}} := \frac{P_{\text{an}}}{R_{\text{g}} \cdot \text{Tanin}} \cdot M_{\text{WH2}}$

$$\rho_{\text{anode}} = 0.124 \frac{\text{kg}}{\text{m}^3}$$

MW of cathode gas mixture is

$$MW_{cat} := MW_{air} \cdot \frac{N_{airin}}{(N_{airin} + NH_{2OinAirin})} + M_{H_2O} \cdot \frac{NH_{2OinAirin}}{N_{airin} + NH_{2OinAirin}}$$

Density of cathode gas

$$\rho_{cathode} := \frac{P_{an}}{R_g \cdot T_{anin}} \cdot MW_{cat}$$

$$\rho_{cathode} = 1.682 \frac{\text{kg}}{\text{m}^3}$$

Reynolds Number for a single channel in anode and cathode becomes;

Anode	$Re_{Anode} := \frac{\rho_{anode} \cdot v_{H_2} \cdot DH}{\mu_{anode}}$	$Re_{Anode} = 1.873$
-------	---	----------------------

Cathode	$Re_{Cathode} := \frac{\rho_{cathode} \cdot v_{Air} \cdot DH}{\mu_{cathode}}$	$Re_{Cathode} = 83.95$
---------	---	------------------------

Both flows are laminar

For a square channel  $Re_f = 56$

Then friction factor for Anode and Cathode becomes

$f_{Anode} := \frac{56}{Re_{Anode}}$	$f_{Anode} = 29.897$
--------------------------------------	----------------------

$f_{Cathode} := \frac{56}{Re_{Cathode}}$	$f_{Cathode} = 0.667$
--	-----------------------

For 90-degree bends  $K_L = 30f$ ; 4 bends exist in the flow field

$$\Delta P_{\text{anode}} := f_{\text{Anode}} \cdot \frac{ChL}{DH} \cdot \rho_{\text{anode}} \cdot \frac{v_{H2}^2}{2} + 4 \cdot 30 \cdot f_{\text{Anode}} \cdot \rho_{\text{anode}} \cdot \frac{v_{H2}^2}{2}$$

$$\Delta P_{\text{anode}} = 8.153 \text{ Pa}$$

$$\Delta P_{\text{cathode}} := f_{\text{Cathode}} \cdot \frac{ChL}{DH} \cdot \rho_{\text{cathode}} \cdot \frac{v_{\text{Air}}^2}{2} + 4 \cdot 30 \cdot f_{\text{Cathode}} \cdot \rho_{\text{cathode}} \cdot \frac{v_{\text{Air}}^2}{2}$$

$$\Delta P_{\text{cathode}} = 112.488 \text{ Pa}$$

This pressure drop has been calculated based on inlet conditions. The velocity at the outlet is somewhat lower, so the average velocity throughout the channel would be lower, and consequently, the pressure drop would be somewhat lower. The exact solution may be obtained through an iterative process.

## A.6 Cooling Calculations

$$L_{\text{stack}} := 124 \text{ mm}$$

$$H_{\text{stack}} := 43 \text{ mm}$$

$$W_{\text{stack}} := 65 \text{ mm}$$

Properties of air

Linear fit for thermal conductivity of air as a function of temperature between 100K and 400K is

Linear Fit:  $y=a+bx$

Coefficient Data:

$$a = 0.0015458571$$

$$b = 8.1394286e-005$$

$$k_{\text{air}}(T) := \left( 0.0015458571 + 8.139428610^{-5} \cdot \frac{1}{K} T \right) \cdot \frac{W}{m \cdot K}$$

Curve fit for kinematic viscosity of air as a function of temperature between 100K and 400K is

Quadratic Fit:  $y=a+bx+cx^2$

Coefficient Data:

$$a = -3.2714286e-008$$

$$b = 5.3369048e-009$$

$$c = 1.5069048e-010$$

$$\nu_{air}(T) := \left( -3.271428610^{-8} + 5.336904810^{-9} \cdot \frac{1}{K} \cdot T + 1.506904810^{-10} \cdot \frac{1}{K^2} \cdot T^2 \right) \frac{m^2}{s}$$

Pr number fit for air as a function of temperature between 100K and 400K is

Quadratic Fit:  $y=a+bx+cx^2$

Coefficient Data:

$$a = 0.81085714$$

$$b = -0.00043285714$$

$$c = 3.1428571e-007$$

$$Pr_{Air}(T) := 0.81085714 - 0.00043285714 \frac{1}{K} T + 3.142857110^{-7} \cdot \frac{1}{K^2} \cdot T^2$$

Wall temperature is the isothermal operating temperature of the stack  $T_w := \text{Temp}$

Film temperature  $T_f := \frac{T_w + T_{environment}}{2}$

$$\beta \beta := \frac{1}{T_f}$$

## A.6.1 Natural convection

from vertical sides;

Rayleigh Number  $Ra(Gr, Pr) := Gr \cdot Pr$

Grashof Number  $Gr := \frac{g \cdot \beta \cdot (T_w - T_{environment}) \cdot H_{stack}^3}{\nu_{air}(T_f)^2}$   $Gr = 3.113 \times 10^5$

Rayleigh number becomes  $Ra(Gr, Pr_{Air}(T_f)) = 2.196 \times 10^5$

From Holman "Heat Transfer"

$$Nu_{Vertical} := 0.59 Ra(Gr, Pr_{Air}(T_f))^{\frac{1}{4}} \quad Nu_{Vertical} = 12.772$$

$$h = \frac{k}{\delta} \times Nu (W / m^2 \cdot ^\circ C)$$

$$h_{NaturalVertical} := \frac{k_{air}(T_f)}{H_{stack}} \cdot Nu_{Vertical} \quad h_{NaturalVertical} = 8.09 \frac{kg}{K \cdot s^3}$$

$$\dot{Q}_{conv} = h \times A \times (T_s - T_\infty) (Watt)$$

$$Q_{NaturalVertical} := h_{NaturalVertical} \cdot 2 \cdot H_{stack} \cdot L_{stack} \cdot (T_w - T_{environment})$$

$$Q_{NaturalVertical} = 3.02W$$

from horizontal top;

Characteristic length for a rectangular horizontal surface is the mean of the side lengths.

$$L_{topCh} := \frac{L_{stack} + W_{stack}}{2} \quad L_{topCh} = 0.095m$$

Grashof Number  $Gr := \frac{g \cdot \beta \cdot (T_w - T_{environment}) \cdot L_{topCh}^3}{\nu_{air}(T_f)^2}$   $Gr = 3.304 \times 10^6$

Rayleigh number becomes  $Ra(Gr, PrAir(Tf)) = 2.331 \times 10^6$

$$Nu_{TopHorizontal} := 0.59 Ra(Gr, PrAir(Tf))^{1/4} \quad Nu_{TopHorizontal} = 23.054$$

$$h_{TopHorizontal} := \frac{k_{air}(Tf)}{L_{topCh}} \cdot Nu_{TopHorizontal} \quad h_{TopHorizontal} = 6.645 \frac{\text{kg}}{\text{K} \cdot \text{s}^3}$$

$$Q_{NaturalTop} := h_{TopHorizontal} \cdot W_{stack} \cdot L_{stack} \cdot (T_w - T_{environment})$$

$$Q_{NaturalTop} = 1.874W$$

$$Q_{NaturalConv} := Q_{NaturalVertical} + Q_{NaturalTop} \quad Q_{NaturalConv} = 4.894W$$

## A.6.2 Radiation

from vertical sides;

$$\dot{Q}_{rad} = \varepsilon \times A \times \sigma \times (T_s^4 - T_\infty^4) \text{ (Watt)}$$

$$\text{Boltzmann's constant} \quad \sigma := 5.669 \cdot 10^{-8} \frac{\text{W}}{\text{m}^2 \cdot \text{K}^4}$$

$$\text{Emissivity of graphite} \quad \varepsilon_m := 0.75$$

$$Q_{VerticalRadiation} := \varepsilon_m \cdot (2 \cdot H_{stack} \cdot L_{stack}) \cdot \sigma \cdot (T_w^4 - T_{environment}^4)$$

$$Q_{VerticalRadiation} = 2.002W$$

from top of the stack;

$$Q_{TopRadiation} := \varepsilon_m \cdot (W_{stack} \cdot L_{stack}) \cdot \sigma \cdot (T_w^4 - T_{environment}^4)$$

$$Q_{TopRadiation} = 1.513W$$

$$Q_{\text{radiation}} := Q_{\text{VerticalRadiation}} + Q_{\text{TopRadiation}} \quad Q_{\text{radiation}} = 3.516\text{W}$$

Total Heat loss naturally

$$Q_{\text{naturally}} := Q_{\text{NaturalVertical}} + Q_{\text{NaturalTop}} + Q_{\text{VerticalRadiation}} + Q_{\text{TopRadiation}}$$

$$Q_{\text{naturally}} = 8.41\text{W}$$

Bottom surface is closed for cooling fan manifold. Therefore, there is no natural (natural convective or radiative) heat transfer occurring naturally from the bottom.

The additional cooling must be supplied is  $Q_{\text{activecooling}} := Q - Q_{\text{naturally}}$

$$Q_{\text{activecooling}} = 162.039\text{W}$$

Air is used for forced convection heat removal fluid

Total number of vertical ducts in the stack is  $N_{\text{coolingDucts}} := 11 \cdot 20$

$$N_{\text{coolingDucts}} = 220$$

The amount of heat must be removed per channel is  $Q_{\text{perchannel}} := \frac{Q_{\text{activecooling}}}{N_{\text{coolingDucts}}}$

$$Q_{\text{perchannel}} = 0.737\text{W}$$

There must be a design value for the outlet air temperature.

Assume  $T_{\text{outletcoolingair}} := T_w - 10\text{K}$

$$\Delta T_{\text{LMcoolingair}} := \frac{(T_w - T_{\text{outletcoolingair}}) - (T_w - T_{\text{environment}})}{\ln \left[ \frac{(T_w - T_{\text{outletcoolingair}})}{(T_w - T_{\text{environment}})} \right]}$$

$$\Delta T_{\text{LMcoolingair}} = 19.956\text{K}$$

The heat transfer coefficient must be to supply necessary cooling,

$$h_{\text{InCoolingChannel}} := \frac{Q_{\text{perchannel}}}{(4.2\text{mm} \cdot 50\text{mm}) \cdot \Delta T_{\text{LMcoolingair}}} \quad h_{\text{InCoolingChannel}} = 92.271 \frac{\text{kg}}{\text{K} \cdot \text{s}^3}$$

Hydraulic diameter of the cooling channel duct having square shape

$$D_{\text{hCoolingChannel}} := 2\text{mm}$$

$$\text{Nu}_{\text{InCoolingchannel}} := \frac{h_{\text{InCoolingChannel}} \cdot D_{\text{hCoolingChannel}}}{k_{\text{air}}(T_f)} \quad \text{Nu}_{\text{InCoolingchannel}} = 6.775$$

Saider and Tate correlation for laminar flow in pipe

$$13 \leq \text{Re} \leq 2030$$

$$0.48 \leq \text{Pr} \leq 16700$$

$$0.0044 \leq \frac{\mu}{\mu_w} \leq 9.75$$

$$\text{Nu} := 1.86 \text{Re}^{\frac{1}{3}} \cdot \text{Pr}^{\frac{1}{3}} \cdot \left(\frac{D_{\text{h}}}{L}\right)^{\frac{1}{3}} \cdot \left(\frac{\mu}{\mu_w}\right)^{0.14} \quad \blacksquare$$

$$\text{Re}_{\text{InCoolingchannel}} := \left[ \frac{\text{Nu}_{\text{InCoolingchannel}}}{1.86 \text{Pr}_{\text{Air}}(T_f)^{\frac{1}{3}} \cdot \left(\frac{D_{\text{hCoolingChannel}}}{H_{\text{stack}}}\right)^{\frac{1}{3}} \cdot \left(\frac{\mu_{\text{Air}}(T_f)}{\mu_{\text{Air}}(T_w)}\right)^{0.14}} \right]^3$$

$$\text{Re}_{\text{InCoolingchannel}} = 1.499 \times 10^3$$

Since Reynolds Number is

$$N_{\text{Re}} = \frac{D_H \times \rho_{\text{Air}} \times v_{\text{Air}}}{\mu_{\text{Air}}}$$

Velocity of cooling air in a channel  $v_{\text{coolingair}} := \frac{\text{ReInCoolingchannel} \cdot \mu_{\text{Air}}(\text{Tf})}{\left( \frac{1 \text{ atm}}{\text{Rg} \cdot \text{Tf}} \cdot \text{MWair} \right) \cdot \text{DhCoolingChannel}}$

$$v_{\text{coolingair}} = 12.732 \frac{\text{m}}{\text{s}}$$

Volumetric flow rate of air in single channel  $Q_{\text{coolingair}} := v_{\text{coolingair}} \cdot (2 \cdot \text{mm})^2$

$$Q_{\text{coolingair}} = 5.093 \times 10^{-5} \frac{\text{m}^3}{\text{s}}$$

Total Volumetric flow rate of cooling air

$$Q_{\text{totalcoolingair}} := Q_{\text{coolingair}} \cdot \text{NcoolingDucts}$$

$$Q_{\text{totalcoolingair}} = 0.011 \frac{\text{m}^3}{\text{s}}$$

Total cooling in slpm  $Q_{\text{totalcoolingairSLPM}} := \frac{Q_{\text{totalcoolingair}}}{\left( 1.667 \times 10^{-5} \frac{\text{m}^3}{\text{s}} \right)}$

$$Q_{\text{totalcoolingairSLPM}} = 672.132$$

$$28 \frac{\text{m}^3}{\text{hr}} = 7.778 \times 10^{-3} \frac{\text{m}^3}{\text{s}}$$

$$35.04 \frac{\text{ft}^3}{\text{min}} = 0.017 \frac{\text{m}^3}{\text{s}}$$

$$Q_{\text{CFM}} := Q_{\text{totalcoolingair}} \cdot \frac{\text{s}}{\text{m}^3} \cdot \frac{35.04}{0.017} \quad Q_{\text{CFM}} = 23.094$$

## APPENDIX B

### FLOW SIMULATION OF SOLIDWORKS

Solidworks Flow Simulation is based on advanced Computational fluid dynamics (CFD) techniques and allows analyzing a wide range of complex problems including:

Two-and three-dimensional analyses

External and internal flows

Steady-state and transient flows

Incompressible liquid and compressible gas flows including subsonic, transonic, and supersonic regimes

Water vapor (steam) condensation

Calculation of relative humidity in gas flows

Non-Newtonian liquids (laminar only)

Compressible liquids (liquid density is dependent on pressure)

Real gases

Laminar, turbulent, and transitional flows

Swirling flows and Fans

Multi-species flows

Flows with heat transfer within and between fluids and solids

Heat transfer in solids only (no fluid exists in the analysis)

Thermal contact resistance

Thermoelectric coolers

Surface-to-surface radiation

Flows with gravitational effects (also known as buoyancy effects)

Porous media

Fluid flows with liquid droplets or solid particles

Walls with roughness

Tangential motion of walls (translation and rotation)

Flows in a rotating device (global rotating frame of reference) or in local regions of rotation

Cavitation in a water flow

## **B.1 Computational Domain**

Flow Simulation analyzes the model geometry and automatically generates a Computational Domain in the shape of a rectangular prism enclosing the model. The computational domain's boundary planes are orthogonal to the model's Global Coordinate System axes. For External flows, the computational domain's boundary planes are automatically distanced from the model. For Internal flows, the computational domain's boundary planes automatically envelop either the entire model (if heat conduction in solids is considered) or the model's flow passage only (if heat conduction in solids is not considered).

Flow Simulation provides accurate results regardless of the model complexity. For Internal flows the only modeling requirement is that all the model openings must be closed with lids. This is required because Flow Simulation boundary conditions at inlets and outlets must be defined on surfaces in contact with the fluid. The lids provide these surfaces for contact with the fluid at the inlets and outlets. One can create lids as Boss-Extrude features on a part or as separate components in an assembly. For External flows, far-field boundary conditions are specified on the Computational Domain boundaries.

## **B.2 Initial and Boundary Conditions**

Before starting the calculation, one must specify boundary conditions and initial conditions for the flow field. For External flows, the far-field boundary conditions are specified on the computational domain's boundary planes. For Internal flows, boundary conditions are specified on the model's walls and at the model's inlets and outlets which are the surfaces of the model lids in contact with the fluid.

The Transferred Boundary Conditions allows one to use results of a previous calculation (may be performed in another project) as a boundary condition. This type of boundary condition can be specified at Computational Domain boundaries for both external and internal flows that may relieve you of providing surfaces to apply the condition (i.e. creating lids) in case of internal flows.

As for the initial conditions, one can either specify them manually in the Wizard or General Settings, or specify them locally with the Initial Conditions dialog box, or take values for them from a previous calculation. See also Initial Conditions - Basic Information.

## **B.3 Meshing**

Following the automatic domain generation and any manual adjustments, Flow Simulation automatically generates a computational mesh.

Alternatively, one can specify parameters governing the initial computational mesh. The mesh is named initial since it can be later refined during the calculation.

The mesh is created by dividing the computational domain into slices, which are further subdivided into rectangular cells. Then the mesh cells are refined as necessary to properly resolve the model geometry.

## B.4 Solving

Flow Simulation discretizes the time-dependent Navier-Stokes equations and solves them on the computational mesh. Under certain conditions, to resolve the solution's features better, Flow Simulation will automatically refine the computational mesh during the flow calculation.

Navier-Stokes equations for Cartesian coordinates are

$$\begin{aligned}\rho \left( \frac{\partial u}{\partial t} + u \frac{\partial u}{\partial x} + v \frac{\partial u}{\partial y} + w \frac{\partial u}{\partial z} \right) &= -\frac{\partial p}{\partial x} + \mu \left( \frac{\partial^2 u}{\partial x^2} + \frac{\partial^2 u}{\partial y^2} + \frac{\partial^2 u}{\partial z^2} \right) + \rho g_x \\ \rho \left( \frac{\partial v}{\partial t} + u \frac{\partial v}{\partial x} + v \frac{\partial v}{\partial y} + w \frac{\partial v}{\partial z} \right) &= -\frac{\partial p}{\partial y} + \mu \left( \frac{\partial^2 v}{\partial x^2} + \frac{\partial^2 v}{\partial y^2} + \frac{\partial^2 v}{\partial z^2} \right) + \rho g_y \\ \rho \left( \frac{\partial w}{\partial t} + u \frac{\partial w}{\partial x} + v \frac{\partial w}{\partial y} + w \frac{\partial w}{\partial z} \right) &= -\frac{\partial p}{\partial z} + \mu \left( \frac{\partial^2 w}{\partial x^2} + \frac{\partial^2 w}{\partial y^2} + \frac{\partial^2 w}{\partial z^2} \right) + \rho g_z\end{aligned}$$

Since Flow Simulation solves steady-state problems by solving the time-dependent equations, Flow Simulation has to decide when a steady-state solution is obtained (i.e. the solution converges), so that the calculation can be stopped. Flow Simulation offers for your choice different conditions of finishing the calculation. To obtain results which are highly reliable from the engineering viewpoint, you can specify some engineering Goals, such as pressure, temperature, force, etc., in specific points, and/or on selected surfaces, and/or in the selected volumes, and/or in the computational domain

## B.5 Time - Dependent Analysis

Flow Simulation solves the time-dependent form of the Navier-Stokes equations. For steady flow problems Flow Simulation starts the calculation from initial conditions

defined by the user. The solver iterates on the variables until there is no appreciable change, i.e. the solution converges. You can facilitate shorter computation times by specifying initial conditions that are close to the final results. Although this practice is recommended, it is not usually required. For External problems the initial conditions will be the Ambient Conditions of the undisturbed fluid stream around the body.

For unsteady (Transient, or Time-dependent) problems Flow Simulation marches the solution from initial conditions for the problem's physical time that you specify. Unlike steady flow problems, the initial conditions must be precise, with the exception of unsteady problems, which have a steady periodic solution (e.g. in the case of periodic boundary conditions) that can be obtained from arbitrary initial conditions, but additional time will be required to eliminate the influence of specified initial conditions.

Steady-state problems are solved by marching the solution in time using time steps determined locally, i.e. at each computational mesh cell independently, which are based on the fluid flow properties of each cell. By default, the time step for solving time-dependent fluid flow problems is specified by Flow Simulation automatically, based on the fluid flow properties only. If you want either to better resolve a problem's time-dependent solution (by specifying a smaller time step than the automatically selected one, e.g. for resolving periodic solutions of too small period) or to calculate a heat transfer in solids faster (by specifying a larger time step than the automatically selected one, e.g. if the fluid flow does not change), it is expedient to specify the time step manually. If you solve a time-dependent problem with heat transfer in solids only, i.e., without calculating a fluid flow (the Heat conduction in solids only option is enabled) a manual specification of the time step is preferable.

## CURRICULUM VITAE

### PERSONAL INFORMATION

Surname, Name: Erkan, Serdar

Nationality: Turkish (TC)

Date and Place of Birth: 27 February 1980, Ankara

Marital Status: Single

Phone: +90 312 210 4372

email: [erkanserdar@gmail.com](mailto:erkanserdar@gmail.com)

### EDUCATION

<b>Degree</b>	<b>Institution</b>	<b>Year of Graduation</b>
MS	METU Chemical Engineering	2005
BS	METU Chemical Engineering	2003
High School	50.Yıl High School, Ankara	1998

### WORK EXPERIENCE

<b>Year</b>	<b>Place</b>	<b>Enrollment</b>
2007-present	Teksis İleri Teknolojiler Ltd. Şti.	Shareholder
2007-2009	Ayes Analitik Dış Tic. Ltd. Şti.	Service Manager
2005-2007	Ayes Analitik Dış Tic. Ltd. Şti.	Service Engineer
2005-2005	EAE Elektrik A.Ş	Engineer
2002	Deva Holding A.Ş. Medicine Factory, İstanbul	Intern Engineering Student
2001	Seydişehir Eti Alüminyum A.Ş, Konya	Intern Engineering Student

### FOREIGN LANGUAGES

Advanced English

## SCHOLARSHIPS AND AWARDS

1. Tubitak PhD Scholarship with project “Pem Yakıt Pilleri için Kompozit Membranlar ve Elektrokatalizörlerin Geliştirilmesi ve Uzun Dönem Performanslarının Belirlenmesi” 109M221, researcher, 2010 - .
2. Tubitak PhD Scholarship with project “Yüksek Sıcaklıkta Çalışabilen Proton Değişim Zarlı Yakıt Hücresi Geliştirilmesi, Researcher, 104M364, 2005-2008.
3. Mediterranean Regional winner of “Abbas Güçlü ile Bizim Mucitler” competition organized by Kanal D – METU – ATO. April 2007.

## PUBLICATIONS

### **Articles published in International Journals**

1. Devrim Y., Erkan S., Baç N., Eroğlu İ. "Preparation and characterization of sulfonated polysulfone/titanium dioxide composite membranes for proton exchange membrane fuel cells" International Journal of Hydrogen Energy 34 (2009) 3467-3475.
2. Şengül E., Erkan S., Eroğlu İ., Baç N. "Effect of Gas Diffusion Layer Characteristics and Addition of Pore Forming Agents on the Performance of Polymer Electrolyte Membrane Fuel Cells" Chemical Engineering Communications, 196, 1-2 (2009) 161-170.
3. Bayrakçeken, A., Erkan, S., Türker, L., Eroğlu, İ., "Effects of membrane electrode assembly components on proton exchange membrane fuel cell performance", International Journal of Hydrogen Energy 33 (2008) 165-170.

### **National and International Congress**

1. A. Yurdakul, S. Erkan, S. Ozkar, I. Eroglu, Design of a Hydrogen Gas Generator Using Aqueous Sodium Borohydride Solution for Portable Fuel

- Cell Applications. "Proceedings of the World Hydrogen Energy Conference (WHEC)", 78, (2010), p.281-286.
2. I. Eroglu, S. Erkan, Development of a 100W PEM Fuel Cell Stack for Portable Applications. "Proceedings of the World Hydrogen Energy Conference (WHEC)", 78, (2010), p.503-507.
  3. Devrim Y., Erkan S., Baç N., Eroğlu I., Nafion/Mixed Inorganic Oxide Nanocomposite Membranes for PEM Fuel Cells. "Proceedings of 10th International Conference on Clean Energy (ICCE 2010)", , (2010), p.1-4.
  4. Yılser Devrim, Serdar Erkan, Nurcan Baç, İnci Eroğlu, Nanocomposite Membranes based on Nafion and TiO<sub>2</sub> for PEM Fuel Cells. "th Chemical Engineering Conference for Collaborative Research in Eastern Mediterranean Countries", , (2010), p.107.
  5. Yurdakul A., Erkan S., Özkar S., Eroğlu I., On Demand Continuous Hydrogen Production System Using Hydrolysis of Sodium borohydride for Portable PEM Fuel Cell Applications. "Proceedings of 10th International Conference on Clean Energy (ICCE 2010)", , (2010), p.1-7
  6. Ergun D., Erkan S., Devrim Y., Bac N., Eroglu I., High Temperature Proton Exchange Membrane Fuel Cells. "Proceedings of HYPOTHESIS VIII", , (2009), p.83.
  7. Erkan S., Eroğlu İ., "100W Gücünde Polimer Zarlı Yakıt Pili Yığını Geliştirilmesi ve Test Edilmesi", 8. Ulusal Kimya Mühendisliği Kongresi, 26-29 Ağustos 2008, Malatya
  8. Şengül, E., Erkan, S., Baç, N., Eroğlu, İ., "Development of gas diffusion electrodes for polymer electrolyte membrane fuel cells", Somer Symposium Series 1, Ankara-Türkiye, May 2007.
  9. Şengül E., Erkan S., Eroğlu İ., Baç N., "Effect of membrane electrode assembly preparation technique on the performance of polymer electrolyte membrane fuel cells", Proc. International Hydrogen Energy Congress and Exhibition, İstanbul-Türkiye, July 2007.

10. Şengül E., Erkan S., Eroğlu İ., Baç N., "Effect of gas diffusion layer characteristics and addition of pore forming agents on the performance of polymer electrolyte membrane fuel cells", Somer Symposium Series I, Poster presentation 14-15 Mayıs 2007 Ankara.
11. Eroğlu İ., Erkan S., Bayrakçeken A., Türker L., Utilization of Metal Phthalocyanines as Cathode Catalysts of Proton Exchange Membrane Fuel Cells. "AIChE 2006 Meeting" , , (2006), p...
12. Erkan S., Bayrakçeken A., Türker L., Eroğlu İ., "Utilization of Metalphthalocyanines as Cathode Catalyst of Proton Exchange Membrane Fuel Cells", Proceedings of International Hydrogen Energy Congress & Exhibition (IHEC-2005), 13-15 July, Istanbul, TURKEY, 2005.
13. Bayrakçeken A., Erkan S., Türker L., Eroğlu İ., "Effect of different construction materials on proton exchange membrane fuel cells", Proceedings of International Hydrogen Energy Congress & Exhibition (IHEC-2005), 13-15 July, Istanbul, TURKEY, 2005.

### **Thesis**

Erkan S., Synthesis of some metalophthalocyanines and their effects on the performance of pem fuel cells. MSc. Thesis in *Chemical Engineering*. M.S. Thesis Ankara, Middle East Technical University, 2005, 97.

### **Books**

1. Baç N., Erdener H., Erkan S., Eroğlu E., Gür N., Şengül E. "Alternatif Enerji Kaynakları ve Hidrojen Enerjisi".(ANKARA: ODTÜ YAYINCILIK, 2007)

### **RESEARCH PROJECTS**

1. "Development of 3 KW Fuel Cell System" UNIDO-ICHET project, 2010 - .

2. “Pem Yakıt Pilleri için Kompozit Membranlar ve Elektrokatalizörlerin Geliştirilmesi ve Uzun Dönem Performanslarının Belirlenmesi” 109M221, researcher, 2010 - .
3. “Sodyum Borhidürle çalışan 100W gücünde taşınabilir yakıt pili sistemi geliştirilmesi” BOREN 2009.Ç0219, Researcher, 2009 - 2011.
4. “Hidrojen Gazı Üretimi, Depolanması ve Yakıt Hücrelerinde Elektrik Elde Edilmesi”, DPT - Yaygınlaştırılmış Ulusal ve Uluslararası (YUUP) Projesi,
5. BAP-08-11-DPT.2005K120600, Researcher, 2006 – 2008.
6. “Yüksek Sıcaklıkta Çalışabilen Proton Değişim Zarlı Yakıt Hücresi Geliştirilmesi, Araştırmacı, TÜBİTAK Projesi 104M364, 2005-2008.
7. “Metalofitalosiyanınların sentezi ve yakıt pillerinin performansına etkileri”, TÜBİTAK-MİSAG 230, Researcher, 2002-2004.

#### CONFERENCE ORGANISATION

1. Scientific Committee Member of International Hydrogen Energy Congress & Exhibition (IHEC-2005), held in Istanbul – TURKEY, 13-15 July, 2005.